Science
AAAS

Supplementary Materials for

High-precision measurement of the *W* boson mass with the CDF II detector

CDF Collaboration

Corresponding author: A. V. Kotwal, ashutosh.kotwal@duke.edu

Science **376**, 170 (2022)
DOI: 10.1126/science.abk1781

The PDF file includes:

Supplementary Materials for

High precision measurement of the W-boson mass with the CDF II detector

CDF Collaboration[§,*] T. Aaltonen,[1,2] S. Amerio,[3,4] D. Amidei,[5] A. Anastassov[a],[6] A. Annovi,[7] J. Antos,[8,9] G. Apollinari,[6] J.A. Appel,[6] T. Arisawa,[10] A. Artikov,[11] J. Asaadi,[12] W. Ashmanskas,[6] B. Auerbach,[13] A. Aurisano,[12] F. Azfar,[14] W. Badgett,[6] T. Bae,[15,16,17,18,19,20,21] A. Barbaro-Galtieri,[22] V.E. Barnes,[23] B.A. Barnett,[24] P. Barria,[25,26] P. Bartos,[8,9] M. Bauce,[3,4] F. Bedeschi,[25] S. Behari,[6] G. Bellettini,[25,27] J. Bellinger,[28] D. Benjamin,[29] A. Beretvas,[6] A. Bhatti,[30] K.R. Bland,[31] B. Blumenfeld,[24] A. Bocci,[29] A. Bodek,[32] D. Bortoletto,[23] J. Boudreau,[33] A. Boveia,[34] L. Brigliadori,[35,36] C. Bromberg,[37] E. Brucken,[1,2] J. Budagov,[11,†] H.S. Budd,[32] K. Burkett,[6] G. Busetto,[3,4] P. Bussey,[38] P. Butti,[25,27] A. Buzatu,[38] A. Calamba,[39] S. Camarda,[40] M. Campanelli,[41] B. Carls,[42] D. Carlsmith,[28] R. Carosi,[25] S. Carrillo[b],[43,†] B. Casal[c],[44] M. Casarsa,[45] A. Castro,[35,36] P. Catastini,[46] D. Cauz,[45,47,48] V. Cavaliere,[42] A. Cerri[d],[22] L. Cerrito[e],[41] Y.C. Chen,[49] M. Chertok,[50] G. Chiarelli,[25] G. Chlachidze,[6] K. Cho,[15,16,17,18,19,20,21] D. Chokheli,[11] A. Clark,[51] C. Clarke,[52] M.E. Convery,[6] J. Conway,[50] M. Corbo[f],[6] M. Cordelli,[7] C.A. Cox,[50] D.J. Cox,[50] M. Cremonesi,[25] D. Cruz,[12] J. Cuevas[g],[44] R. Culbertson,[6] N. d'Ascenzo[h],[6] M. Datta[i],[6] P. de Barbaro,[32] L. Demortier,[30] M. Deninno,[35,†] M. D'Errico,[3,4] F. Devoto,[1,2] A. Di Canto,[25,27] B. Di Ruzza[j],[6] J.R. Dittmann,[31] S. Donati,[25,27] M. D'Onofrio,[53] M. Dorigo,[45,54] A. Driutti,[45,47,48] K. Ebina,[10] R. Edgar,[5] A. Elagin,[34] R. Erbacher,[50] S. Errede,[42] B. Esham,[42] S. Farrington,[14] J.P. Fernández Ramos,[55] R. Field,[43] G. Flanagan[k],[6] R. Forrest,[50] M. Franklin,[46] J.C. Freeman,[6] H. Frisch,[34] Y. Funakoshi,[10] C. Galloni,[25,27] A.F. Garfinkel,[23] P. Garosi,[25,26] H. Gerberich,[42] E. Gerchtein,[6] S. Giagu,[56] V. Giakoumopoulou,[57] K. Gibson,[33] C.M. Ginsburg,[6] N. Giokaris,[57,†] P. Giromini,[7] V. Glagolev,[11] D. Glenzinski,[6] M. Gold,[58] D. Goldin,[12] A. Golossanov,[6] G. Gomez,[44] G. Gomez-Ceballos,[59] M. Goncharov,[59] O. González López,[55] I. Gorelov,[58] A.T. Goshaw,[29] K. Goulianos,[30] E. Gramellini,[35] C. Grosso-Pilcher,[34] J. Guimaraes da Costa,[46] S.R. Hahn,[6] J.Y. Han,[32] F. Happacher,[7] K. Hara,[60] M. Hare,[61] R.F. Harr,[52] T. Harrington-Taber[l],[6] K. Hatakeyama,[31] C. Hays,[14] J. Heinrich,[62] M. Herndon,[28] A. Hocker,[6] Z. Hong[m],[12] W. Hopkins[n],[6] S. Hou,[49] R.E. Hughes,[63] U. Husemann,[64] M. Hussein[o],[37] J. Huston,[37] G. Introzzi,[25,65,66] M. Iori,[56,67] A. Ivanov[p],[50] E. James,[6] D. Jang,[39] B. Jayatilaka,[6] E.J. Jeon,[15,16,17,18,19,20,21] S. Jindariani,[6] M. Jones,[23] K.K. Joo,[15,16,17,18,19,20,21] S.Y. Jun,[39] T.R. Junk,[6] M. Kambeitz,[68] T. Kamon,[15,16,17,18,19,20,21,12] P.E. Karchin,[52] A. Kasmi,[31] Y. Kato[q],[69] W. Ketchum[r],[34] J. Keung,[62] B. Kilminster[s],[6] D.H. Kim,[15,16,17,18,19,20,21] H.S. Kim[t],[6] J.E. Kim,[15,16,17,18,19,20,21] M.J. Kim,[7] S.H. Kim,[60] S.B. Kim,[15,16,17,18,19,20,21] Y.J. Kim,[15,16,17,18,19,20,21] Y.K. Kim,[34] N. Kimura,[10] M. Kirby,[6] K. Kondo,[10,†] D.J. Kong,[15,16,17,18,19,20,21] J. Konigsberg,[43] A.V. Kotwal,[29,‡] M. Kreps,[68] J. Kroll,[62] M. Kruse,[29] T. Kuhr,[68] M. Kurata,[60] A.T. Laasanen,[23] S. Lammel,[6] M. Lancaster,[41] K. Lannon[u],[63] G. Latino,[25,26] H.S. Lee,[15,16,17,18,19,20,21] J.S. Lee,[15,16,17,18,19,20,21] S. Leo,[42] S. Leone,[25] J.D. Lewis,[6] A. Limosani[v],[29] E. Lipeles,[62] A. Lister[w],[51] Q. Liu,[23] T. Liu,[6] S. Lockwitz,[64] A. Loginov,[64,†] D. Lucchesi,[3,4] A. Lucà,[7,6] J. Lueck,[68] P. Lujan,[22] P. Lukens,[6] G. Lungu,[30] J. Lys,[22,†] R. Lysak[x],[8,9] R. Madrak,[6] P. Maestro,[25,26] S. Malik,[30] G. Manca[y],[53] A. Manousakis-Katsikakis,[57] L. Marchese[z],[35] F. Margaroli,[56] P. Marino,[25,70] K. Matera,[42] M.E. Mattson,[52] A. Mazzacane,[6] P. Mazzanti,[35] R. McNulty[aa],[53] A. Mehta,[53] P. Mehtala,[1,2] A. Menzione,[25,†] C. Mesropian,[30] T. Miao,[6] E. Michielin,[3,4] D. Mietlicki,[5] A. Mitra,[49] H. Miyake,[60] S. Moed,[6] N. Moggi,[35] C.S. Moon,[15,16,17,18,19,20,21] R. Moore[bb cc],[6] M.J. Morello,[25,70] A. Mukherjee,[6] Th. Muller,[68] P. Murat,[6] M. Mussini,[35,36] J. Nachtman[l],[6] Y. Nagai,[60] J. Naganoma,[10] I. Nakano,[71] A. Napier,[61] J. Nett,[12] T. Nigmanov,[33] L. Nodulman,[13] S.Y. Noh,[15,16,17,18,19,20,21] O. Norniella,[42] L. Oakes,[14] S.H. Oh,[29] Y.D. Oh,[15,16,17,18,19,20,21] T. Okusawa,[69] R. Orava,[1,2] L. Ortolan,[40] C. Pagliarone,[45] E. Palencia[d],[44] P. Palni,[58] V. Papadimitriou,[6] W. Parker,[28] G. Pauletta,[45,47,48] M. Paulini,[39] C. Paus,[59] T.J. Phillips,[29] G. Piacentino[dd],[6] E. Pianori,[62] J. Pilot,[50] K. Pitts,[42] C. Plager,[72] L. Pondrom,[28] S. Poprocki[n],[6] K. Potamianos,[22] A. Pranko,[22] F. Prokoshin[ee],[11] F. Ptohos[ff],[7] G. Punzi,[25,27] I. Redondo Fernández,[55] P. Renton,[14] M. Rescigno,[56] F. Rimondi,[35,†] L. Ristori,[25,6] A. Robson,[38] T. Rodriguez,[62] S. Rolli[gg],[61] M. Ronzani,[25,27] R. Roser,[6] J.L. Rosner,[34] F. Ruffini,[25,26] A. Ruiz,[44] J. Russ,[39] V. Rusu,[6] W.K. Sakumoto,[32] Y. Sakurai,[10] L. Santi,[45,47,48] K. Sato,[60] V. Saveliev[h],[6] A. Savoy-Navarro[f],[6] P. Schlabach,[6] E.E. Schmidt,[6] T. Schwarz,[5] L. Scodellaro,[44] F. Scuri,[25] S. Seidel,[58] Y. Seiya,[69] A. Semenov,[11] F. Sforza,[25,27] S.Z. Shalhout,[50] T. Shears,[53] P.F. Shepard,[33] M. Shimojima[hh],[60] M. Shochet,[34] I. Shreyber-Tecker,[73] A. Simonenko,[11] K. Sliwa,[61] J.R. Smith,[50] F.D. Snider,[6] H. Song,[33] V. Sorin,[40] R. St. Denis,[38,†] M. Stancari,[6] D. Stentz[a],[6] J. Strologas,[58] Y. Sudo,[60] A. Sukhanov,[6] I. Suslov,[11] K. Takemasa,[60] Y. Takeuchi,[60] J. Tang,[34] M. Tecchio,[5] P.K. Teng,[49] J. Thom[n],[6] E. Thomson,[62] V. Thukral,[12] D. Toback,[12] S. Tokar,[8,9] K. Tollefson,[37] T. Tomura,[60] S. Torre,[7] D. Torretta,[6] P. Totaro,[3] M. Trovato,[25,70] F. Ukegawa,[60] S. Uozumi,[15,16,17,18,19,20,21]

F. Vázquez[b],[43] G. Velev,[6] K. Vellidis,[57] C. Vernieri,[25,70] M. Vidal,[23] R. Vilar,[44] J. Vizán[ii],[44] M. Vogel,[58] G. Volpi,[7] P. Wagner,[62] R. Wallny[c],[6] S.M. Wang,[49] D. Waters,[41] W.C. Wester III,[6] D. Whiteson[jj],[62] A.B. Wicklund,[13] S. Wilbur,[50] H.H. Williams,[62] J.S. Wilson,[5] P. Wilson,[6] B.L. Winer,[63] P. Wittich[n],[6] S. Wolbers,[6] H. Wolfmeister,[63] T. Wright,[5] X. Wu,[51] Z. Wu,[31] K. Yamamoto,[69] D. Yamato,[69] T. Yang,[6] U.K. Yang,[15,16,17,18,19,20,21] Y.C. Yang,[15,16,17,18,19,20,21] W.-M. Yao,[22] G.P. Yeh,[6] K. Yi[l kk],[6] J. Yoh,[6] K. Yorita,[10] T. Yoshida[ll],[69] G.B. Yu,[15,16,17,18,19,20,21] I. Yu,[15,16,17,18,19,20,21] A.M. Zanetti,[45] Y. Zeng,[29] C. Zhou,[29] and S. Zucchelli[35,36]

[1]*Division of High Energy Physics, Department of Physics, University of Helsinki, FIN-00014, Helsinki, Finland*
[2]*Helsinki Institute of Physics, FIN-00014, Helsinki, Finland*
[3]*Istituto Nazionale di Fisica Nucleare, Sezione di Padova, I-35131 Padova, Italy*
[4]*University of Padova, I-35131 Padova, Italy*
[5]*University of Michigan, Ann Arbor, Michigan 48109, USA*
[6]*Fermi National Accelerator Laboratory, Batavia, Illinois 60510, USA*
[7]*Laboratori Nazionali di Frascati, Istituto Nazionale di Fisica Nucleare, I-00044 Frascati, Italy*
[8]*Comenius University, 842 48 Bratislava, Slovakia*
[9]*Institute of Experimental Physics, 040 01 Kosice, Slovakia*
[10]*Waseda University, Tokyo 169, Japan*
[11]*Joint Institute for Nuclear Research, RU-141980 Dubna, Russia*
[12]*Mitchell Institute for Fundamental Physics and Astronomy, Texas A&M University, College Station, Texas 77843, USA*
[13]*Argonne National Laboratory, Argonne, Illinois 60439, USA*
[14]*University of Oxford, Oxford OX1 3RH, United Kingdom*
[15]*Center for High Energy Physics, Kyungpook National University, Daegu 702-701, Korea*
[16]*Seoul National University, Seoul 151-742, Korea*
[17]*Sungkyunkwan University, Suwon 440-746, Korea*
[18]*Korea Institute of Science and Technology Information, Daejeon 305-806, Korea*
[19]*Chonnam National University, Gwangju 500-757, Korea*
[20]*Chonbuk National University, Jeonju 561-756, Korea*
[21]*Ewha Womans University, Seoul, 120-750, Korea*
[22]*Ernest Orlando Lawrence Berkeley National Laboratory, Berkeley, California 94720, USA*
[23]*Purdue University, West Lafayette, Indiana 47907, USA*
[24]*The Johns Hopkins University, Baltimore, Maryland 21218, USA*
[25]*Istituto Nazionale di Fisica Nucleare Pisa, I-56127 Pisa, Italy*
[26]*University of Siena, I-53100 Siena, Italy*
[27]*University of Pisa, I-56126 Pisa, Italy*
[28]*University of Wisconsin-Madison, Madison, Wisconsin 53706, USA*
[29]*Duke University, Durham, North Carolina 27708, USA*
[30]*The Rockefeller University, New York, New York 10065, USA*
[31]*Baylor University, Waco, Texas 76798, USA*
[32]*University of Rochester, Rochester, New York 14627, USA*
[33]*University of Pittsburgh, Pittsburgh, Pennsylvania 15260, USA*
[34]*Enrico Fermi Institute, University of Chicago, Chicago, Illinois 60637, USA*
[35]*Istituto Nazionale di Fisica Nucleare Bologna, I-40127 Bologna, Italy*
[36]*University of Bologna, I-40127 Bologna, Italy*
[37]*Michigan State University, East Lansing, Michigan 48824, USA*
[38]*Glasgow University, Glasgow G12 8QQ, United Kingdom*
[39]*Carnegie Mellon University, Pittsburgh, Pennsylvania 15213, USA*
[40]*Institut de Fisica d'Altes Energies, ICREA, Universitat Autonoma de Barcelona, E-08193, Bellaterra (Barcelona), Spain*
[41]*University College London, London WC1E 6BT, United Kingdom*
[42]*University of Illinois, Urbana, Illinois 61801, USA*
[43]*University of Florida, Gainesville, Florida 32611, USA*
[44]*Instituto de Fisica de Cantabria, CSIC-University of Cantabria, 39005 Santander, Spain*
[45]*Istituto Nazionale di Fisica Nucleare Trieste, I-34127 Trieste, Italy*
[46]*Harvard University, Cambridge, Massachusetts 02138, USA*
[47]*Gruppo Collegato di Udine, I-33100 Udine, Italy*
[48]*University of Udine, I-33100 Udine, Italy*
[49]*Institute of Physics, Academia Sinica, Taipei, Taiwan 11529, Republic of China*
[50]*University of California, Davis, Davis, California 95616, USA*
[51]*University of Geneva, CH-1211 Geneva 4, Switzerland*
[52]*Wayne State University, Detroit, Michigan 48201, USA*
[53]*University of Liverpool, Liverpool L69 7ZE, United Kingdom*
[54]*University of Trieste, I-34127 Trieste, Italy*

[55] Centro de Investigaciones Energeticas Medioambientales y Tecnologicas, E-28040 Madrid, Spain
[56] Istituto Nazionale di Fisica Nucleare, Sezione di Roma 1, I-00185 Roma, Italy
[57] National and Kapodistrian University of Athens, 157 71 Athens, Greece
[58] University of New Mexico, Albuquerque, New Mexico 87131, USA
[59] Massachusetts Institute of Technology, Cambridge, Massachusetts 02139, USA
[60] University of Tsukuba, Tsukuba, Ibaraki 305, Japan
[61] Tufts University, Medford, Massachusetts 02155, USA
[62] University of Pennsylvania, Philadelphia, Pennsylvania 19104, USA
[63] The Ohio State University, Columbus, Ohio 43210, USA
[64] Yale University, New Haven, Connecticut 06520, USA
[65] Istituto Nazionale di Fisica Nucleare Pavia, I-27100 Pavia, Italy
[66] University of Pavia, I-27100 Pavia, Italy
[67] Sapienza Università di Roma, I-00185 Roma, Italy
[68] Institut für Experimentelle Kernphysik, Karlsruhe Institute of Technology, D-76131 Karlsruhe, Germany
[69] Osaka City University, Osaka 558-8585, Japan
[70] Scuola Normale Superiore, I-56126 Pisa, Italy
[71] Okayama University, Okayama 700-8530, Japan
[72] University of California, Los Angeles, Los Angeles, California 90024, USA
[73] Institution for Theoretical and Experimental Physics, ITEP, Moscow 117259, Russia
(Dated:)

*All listed authors are members of the collaboration; §visiting from [a]Northwestern University, Evanston, IL 60208, USA, [b]Universidad Iberoamericana, Lomas de Santa Fe, México, C.P. 01219, Distrito Federal, [c]ETH, 8092 Zürich, Switzerland, [d]CERN, CH-1211 Geneva, Switzerland, [e]Queen Mary, University of London, London, E1 4NS, United Kingdom, [f]CNRS-IN2P3, Paris, F-75205 France, [g]Universidad de Oviedo, E-33007 Oviedo, Spain, [h]National Research Nuclear University, Moscow 115409, Russia, [i]Hampton University, Hampton, VA 23668, USA, [j]Brookhaven National Laboratory, Upton, NY 11973, USA, [k]Muons, Inc., Batavia, IL 60510, USA, [l]University of Iowa, Iowa City, IA 52242, USA, [m]University of Toronto, Toronto, Ontario M5S 1A7, Canada, [n]Cornell University, Ithaca, NY 14853, USA, [o]The University of Jordan, Amman 11942, Jordan, [p]Kansas State University, Manhattan, KS 66506, USA, [q]Kinki University, Higashi-Osaka City, Japan 577-8502, [r]Los Alamos National Laboratory, Los Alamos, NM 87544, USA, [s]University of Zürich, 8006 Zürich, Switzerland, [t]Sejong University, Seoul 143-747, Korea, [u]University of Notre Dame, Notre Dame, IN 46556, USA, [v]University of Melbourne, Victoria 3010, Australia, [w]University of British Columbia, Vancouver, BC V6T 1Z1, Canada, [x]Institute of Physics, Academy of Sciences of the Czech Republic, 182 21, Czech Republic, [y]Istituto Nazionale di Fisica Nucleare, Sezione di Cagliari, 09042 Monserrato (Cagliari), Italy, [z]Università degli Studi di Napoli Federico II, I-80138 Napoli, Italy, [aa]University College Dublin, Dublin 4, Ireland, [bb]Massachusetts General Hospital, Boston, MA 02114 USA, [cc]Harvard Medical School, Boston, MA 02114 USA, [dd]Istituto Nazionale di Fisica Nucleare, Sezione di Lecce, Via Arnesano, I-73100 Lecce, Italy, [ee]Universidad Tecnica Federico Santa Maria, 110v Valparaiso, Chile, [ff]University of Cyprus, Nicosia CY-1678, Cyprus, [gg]Office of Science, U.S. Department of Energy, Washington, DC 20585, USA, [hh]Nagasaki Institute of Applied Science, Nagasaki 851-0193, Japan, [ii]Universite catholique de Louvain, 1348 Louvain-La-Neuve, Belgium, [jj]University of California Irvine, Irvine, CA 92697, USA, [kk]Nanjing Normal University, Department of Physics, Nanjing, China, [ll]University of Fukui, Fukui City, Fukui Prefecture, Japan 910-0017
†Deceased
‡Corresponding author. Email: ashutosh.kotwal@duke.edu

I. OVERVIEW

In the standard model (SM) of particle physics, the mediators of the electroweak interactions are the massive W and Z bosons and the massless photon. They are the quanta of the gauge fields in the locally gauge-invariant theory with the symmetry specified by the Lie group $SU(2)_L \times U(1)_Y$ [7–9]. The W and Z bosons would be massless if the gauge symmetry were unbroken. In the SM, the symmetry-breaking mechanism known as the Higgs mechanism [1–4] imparts masses as emergent properties to the W and Z bosons and the fermions. In the Higgs mechanism, a fundamental scalar "Higgs" field develops a condensate (a vacuum expectation value) in all space. The bosonic excitation of this field, the Higgs boson, was discovered at the Large Hadron Collider (LHC) in 2012 [5, 6].

As all the components of the SM have been experimentally established with high precision, global fits of the model to the data provide precise estimates of fundamental parameters of nature, such as the W boson mass. This quantity is estimated at present by SM global fits to a fractional precision of 0.01%, providing strong motivation to measure it at the same level of precision.

Following the discovery of the W boson in 1983 at the UA1 and UA2 experiments [68–71], measurements of M_W have been performed with increasing precision using $\sqrt{s} = 1.8$ TeV $p\bar{p}$ collisions at the CDF [28] and D0 [29, 31, 32] experiments in Tevatron Run I [33]; e^+e^- collisions at $\sqrt{s} = 161-209$ GeV at the ALEPH [34], DELPHI [35], L3 [36], and OPAL [37] experiments (LEP); and $\sqrt{s} = 1.96$ TeV $p\bar{p}$ collisions at the CDF [38, 39] and D0 [40] experiments (Tevatron Run II). Combining results from the Tevatron Run I, LEP, and the first Tevatron Run II measurements yields $M_W = 80\,399 \pm 23$ MeV [44]. Subsequent measurements performed with the CDF [41] and D0 [42] experiments have improved the global combination to $M_W = 80\,385 \pm 15$ MeV [45]. The ATLAS collaboration published a W-boson mass measurement of $M_W = 80\,370 \pm 19$ MeV [46, 47]. The CDF measurement described in this article, $M_W = 80\,433.5 \pm 9.4$ MeV/c^2, is more precise than all previous W-boson mass measurements combined.

The measurement strategy is described in Ref. [43] and summarized here. W and Z boson candidate events are selected by requiring high-p_T electron(s) or muon(s). The vector transverse momentum sum of all detectable collision products accompanying the W or Z boson is defined as the hadronic recoil $\vec{u} = \Sigma_i E_{T,i}\hat{n}_i = \Sigma_i E_i \sin(\theta_i)\hat{n}_i$. The sum runs over calorimeter towers [52], with energy E_i, polar angle θ_i, and transverse directions specified by unit vectors $\hat{n}_i$. Calorimeter towers containing energy deposition from the charged lepton(s) are excluded. The neutrino transverse momentum vector $\vec{p}_T^{\,\nu}$ is inferred as $\vec{p}_T^{\,\nu} \equiv -\vec{p}_T^{\,\ell} - \vec{u}$ from $\vec{p}_T$ conservation, where $\vec{p}_T^{\,\ell}$ is the vector p_T (E_T) of the muon (electron). In analogy with a two-body invariant mass, the W-boson transverse mass is defined using only the transverse momenta as $m_T = \sqrt{2\,(\,p_T^{\ell}\,p_T^{\nu} - \vec{p}_T^{\,\ell}\cdot\vec{p}_T^{\,\nu})}$ [53]. The measurement is performed by fitting for M_W using the three quantities, p_T^{ℓ}, p_T^{ν}, and m_T, which have varying degrees of sensitivity to the modeling of the hadronic recoil and the p_T of the W boson.

We calibrate track momenta using large samples of J/ψ and Υ meson decays to muon pairs, and test the calibration by comparing the Z-boson mass measured in $Z \to \mu\mu$ decays with the precise world-average value [10, 44]. The electron energy scale is calibrated using the ratio of the calorimeter energy to track momentum (E/p) in W and Z boson decays to electrons. The M_Z measurement in $Z \to ee$ decays is used to validate the electron energy calibration. During the calibration, all M_Z fit results from both ee and $\mu\mu$ decay channels are hidden by a single unknown additive offset in the range $[-50, 50]$ MeV. After completing the calibrations, the offset is removed (unblinding) and the results are included in the final calibration used for the M_W fits.

Since the W- and Z-boson hadronic recoils are similar, we tune the recoil response model using fully-reconstructed $Z \to \ell\ell$ data. These data are also used to tune the model of the p_T distribution of Z bosons, which is combined with a precise calculation [54–56] of the ratio of the p_T distributions of W and Z bosons to predict the p_T distribution of W bosons.

All simulated distributions, including the p_T^{ℓ}, p_T^{ν}, and m_T distributions of W bosons and the kinematic distributions of J/ψ, Υ and Z bosons are obtained from a custom Monte Carlo simulation [39, 43]. The M_W result is obtained by combining the m_T, p_T^{ℓ}, and p_T^{ν} fit results from both $W \to e\nu$ and $W \to \mu\nu$ channels, taking into account their correlations. As with the fits for M_Z, another blinding offset in the range $[-50, 50]$ MeV is applied to all M_W fits. No changes are made to the results once the offsets are removed.

The structure of this supplement is as follows. A brief detector description is provided in Sec. II and summary of the custom simulation is provided in Sec. III. Within the custom simulation, the model of the W and Z boson event generator is described in Sec. IV. The measurements of event selection efficiencies in the experimental data are described in Sec. V. The calibration of the track momentum and calorimeter energy measurements is described in Secs. VI and VII respectively. The estimation of the recoil model parameters is described in Sec. VIII, and background processes and their contributions to the W-boson data samples are discussed in Sec. IX. Finally, the W-boson mass fits, associated uncertainties and the combination of fit results are described in Sec. X.

While the analysis techniques draw heavily from the previous analysis [43], a number of new methods or refinements have been introduced to extract additional information from the data or to use improved calculations. A summary

Method or technique	impact	section of paper
Detailed treatment of parton distribution functions	+3.5 MeV	IV A
Resolved beam-constraining bias in CDF reconstruction	+10 MeV	VI C
Improved COT alignment and drift model [65]	uniformity	VI
Improved modeling of calorimeter tower resolution	uniformity	III
Temporal uniformity calibration of CEM towers	uniformity	VII A
Lepton removal procedure corrected for luminosity	uniformity	VIII A
Higher-order calculation of QED radiation in J/ψ and Υ decays	accuracy	VI A & B
Modeling kurtosis of hadronic recoil energy resolution	accuracy	VIII B 2
Improved modeling of hadronic recoil angular resolution	accuracy	VIII B 3
Modeling dijet contribution to recoil resolution	accuracy	VIII B 4
Explicit luminosity matching of pileup	accuracy	VIII B 5
Modeling kurtosis of pileup resolution	accuracy	VIII B 5
Theory model of p_T^W/p_T^Z spectrum ratio	accuracy	IV B
Constraint from p_T^W data spectrum	robustness	VIII B 6
Cross-check of p_T^Z tuning	robustness	IV B

TABLE S1: Summary of analysis updates with respect to [43]. The second column provides a quantitative estimate of the change induced in the previous result [43] due to the update. In case this estimate is not available, the second column indicates whether the update is expected to improve the temporal or spatial uniformity of the detector, increase the robustness of the analysis or the accuracy of the result.

of these updates is presented in Table S1, along with the expected impact and references to the sections of this supplement where the respective descriptions are provided. In some cases, the additive change induced by the update can be added to our previously published M_W value of $M_W = 80\,387 \pm 19$ MeV [41, 43] since the updated procedures can be incorporated into the previous analysis without repeating the latter. In other cases, the impact is classified in terms of the expected improvement in detector uniformity, analysis accuracy, or robustness. The shifts shown in the first two rows of Table S1 result in an updated value of $M_W = 80\,400.5$ MeV. With the correlations due to parton distribution functions, the momentum scale calibration and QED radiative corrections taken into account, the consistency between the updated previous measurement and the new measurement is at the percent level, assuming purely Gaussian fluctuations. Considering the large number of systematic improvements in analysis techniques, the best estimate of M_W quoted in this paper is a freestanding result obtained from a blind procedure, and supersedes our 2012 result [41, 43] in the same spirit as the latter superseding our 2007 result [38]. Subsequent analyses with new or modified procedures, such as independently blinded measurements in subsamples of data, are being pursued.

II. THE CDF II DETECTOR

The CDF II detector [39, 72, 73] is forward-backward and cylindrically symmetric [50]. Its relevant components, in order of increasing radius, are a charged-particle tracking system, composed of a silicon vertex detector [74] between radii of 2.5 cm and 29 cm, and an open-cell drift chamber [48] in the radial range of $40 < r < 138$ cm and covering the region $|z| < 155$ cm; a superconducting solenoid [75] with a length of 5 m and a radius of 1.5 m, generating a 1.4 T magnetic field; electromagnetic calorimeters [76, 77] to contain electron and photon showers and measure their energies, and hadronic calorimeters [78] to measure the energies of hadronic showers; and a muon detection system [49] for identification of muon candidates with $p_T \gtrsim 2$ GeV. Collision events passing three levels of online selection (trigger) are recorded for offline analysis. The major detector subsystems are described in Ref. [43].

Charged particles with $p_T \gtrsim 300$ MeV and $|\eta| \lesssim 1$ traverse the entire radius of the central outer tracking drift chamber (COT) [48]. The hit positions in the COT are used to reconstruct the helical trajectory of a charged particle using a χ^2 minimization, including an optional constraint to the transverse position of the beam. The fitted helix is parameterized by the signed transverse impact parameter (minimal distance) with respect to the nominal beam axis, d_0 (in the absence of the beam constraint); the azimuthal angle of the track direction at closest approach to the beam, ϕ_0; the longitudinal position at closest approach to the beam, z_0; the cotangent of the polar angle, $\cot\theta$; and the curvature, $c \equiv q/(2R)$, where $q = \pm 1$ is the particle charge and R is the radius of curvature. The measured track p_T is proportional to the inverse of the track curvature. Information from the silicon vertex detector is not used

because it does not significantly improve the resolution of the beam-constrained parameters for the particles used in this analysis.

The calorimeter has a projective-tower geometry with an inner electromagnetic compartment and an outer hadronic compartment. The central electromagnetic calorimeter (CEM) detects particles with $|\eta| < 1.1$ [76, 77], and the forward *plug* calorimeter covers $1.1 < |\eta| < 3.6$ [79, 80]. The CEM is approximately 18 radiation lengths thick.

Two control data samples are selected to study the recoil resolution. A *zero bias* trigger randomly samples beam bunch crossings, while a *minimum bias* trigger collects events consistent with the presence of an inelastic collision.

The data set used for analysis is selected by requiring that the relevant detector subsystems are stable and fully operational so that the data produced by them are of high quality. These subsystems include the online hardware triggers and the software event filter, the COT, solenoid, calorimeter and muon system, and the luminosity monitors. The data satisfying these requirements correspond to an integrated luminosity of 8.8 fb^{-1}. Detector subsystems such as the silicon vertex detector, its associated hardware trigger, and the time-of-flight detector, that are not used in this analysis are not subject to quality requirements.

III. DETECTOR SIMULATION

We summarize here the key aspects of the custom simulation, which is described in detail in Refs. [39, 43]. This simulation emphasizes the accuracy of the event generation for leptonic decays of bosons, and the accurate modeling of the detector response to leptons and the inclusive hadronic activity. The simulation of lepton interactions includes the processes of ionization energy loss and multiple Coulomb scattering. The ionization energy loss is calculated on the basis of material ionization properties in fine radial, azimuthal and longitudinal granularity in the silicon detector, and per electrode in the COT. In the same radial steps, Coulomb scattering is modeled by a double-Gaussian distribution of the scattering angle, based on the layer's radiation length [39, 43, 81]. If the amount of ionizing material were mismodeled in the simulation, the fitted $J/\psi \to \mu\mu$ mass would display a linear dependence on the mean inverse p_T (denoted by $\langle p_T^{-1} \rangle$) of the final-state muons. To obtain a $J/\psi \to \mu\mu$ mass determination that is independent of $\langle p_T^{-1} \rangle$, the amount of ionizing material in the default simulation of the silicon detector is adjusted by a few percent, as described in Sec. VI A.

The electron simulation also includes a detailed model of bremsstrahlung using the Bethe-Heitler spectrum [39, 43, 81] corrected for the suppression of very soft photons (due to Compton scattering and the Landau-Pomeranchuk-Migdal (LPM) effect [82–85]) or very hard photons (due to incomplete screening of the nuclear electromagnetic field by the atomic electrons [81]). The material composition [43] of each radial detector layer is used to model the material dependence of the LPM effect, which occurs due to quantum-mechanical interference caused by multiple scattering. Photons and electrons in close proximity are merged in the CEM simulation. Photon conversion and Compton scattering, as well as internal conversion of radiative photons, are modeled in the custom simulation [43].

Individual measurement points (*hits*) along the lepton trajectories are simulated [39, 43] with spatial resolution determined as a function of radius from the reconstructed muon tracks in $Z \to \mu\mu$ data. These resolutions are modeled as double-Gaussian distributions that describe the hit residuals accurately. The hit resolution varies from 140 μm to 120 μm (320 μm to 260 μm) for the core (tail) Gaussian distribution, and the tail fraction varies from 29% to 11%, from the inner to the outer radius of the COT. When fitting the $J/\psi \to \mu\mu$ and $\Upsilon \to \mu\mu$ mass distributions, these resolutions are further tuned by a few percent to best match the widths of the mass distributions of the J/ψ and Υ resonances in data. The tuning of the resolutions is uncorrelated with the mass fits. The hit multiplicity distributions are used to tune the model of hit efficiencies [39, 43]. A small inefficiency, correlated across all COT wires at small radius, is included to account for the effects of high occupancy. Prompt lepton tracks are constrained to pass through the transverse beam position to improve their resolution. The transverse beam spot size is tuned to $(36.0 \pm 0.5_{\rm stat})$ μm using the width of the peak of the reconstructed $Z \to \mu\mu$ mass distribution. The hit resolution model and the resulting track-parameter resolutions are validated by comparing the simulated and data distributions of the track impact parameter and the difference of the z_0 values of the two muon tracks in $Z \to \mu\mu$ events. As shown in Fig. S1, these distributions are adequately described by the simulation.

The calorimeter response to electrons and photons is calculated as a function of energy and traversed radiation lengths using a detailed GEANT-based simulation [64]. The fraction of energy leaked from the outer surface of the EM calorimeter, and the energy loss in the material upstream of the calorimeter, are parametrized from this calculation and included in the custom simulation. To describe residual effects due to aging or attenuation in the light guides, the measured transverse energy $E_T^{\rm meas}$ is parametrized as

$$E_T^{\rm meas} = S_E \left(1 + \zeta \log \frac{E_T^{\rm inc}}{39\ {\rm GeV}}\right) E_T^{\rm inc}, \tag{S1}$$

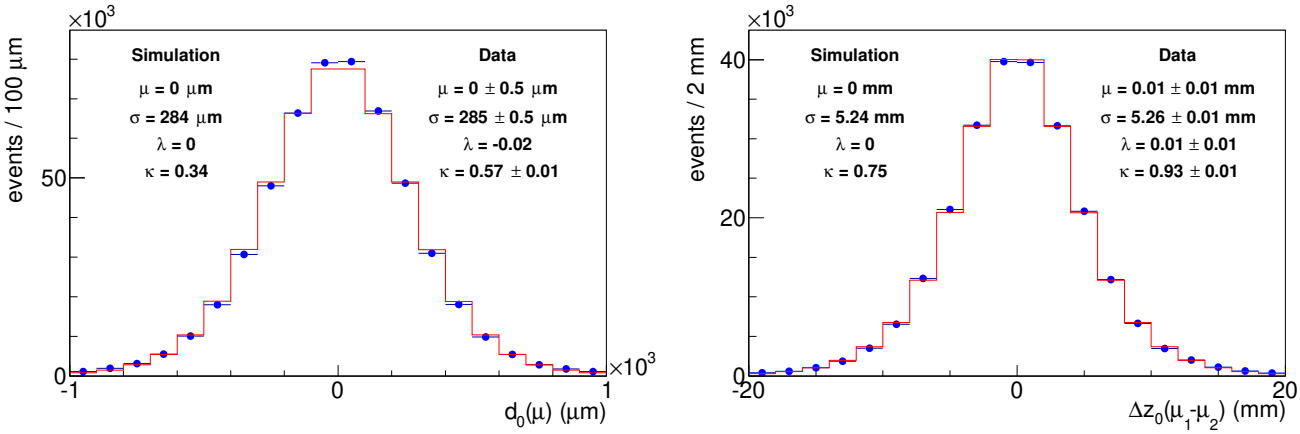

FIG. S1: Comparisons of the distributions of the impact parameter d_0 (left) and the difference of z_0 values (right) for the muon tracks in $Z \to \mu\mu$ data (circles) and simulation (histogram). The cumulants of the distributions, rms (σ), skewness (λ) and excess kurtosis (κ) are in adequate agreement.

where $E_T^{\rm inc}$ is the incident transverse energy, the empirical parameter ζ accounts for remaining non-linearity and S_E is the energy scale determined using the same data (see Sec. VII). The correction ζ is determined using the E/p distribution in W and Z boson data.

Electrons and photons in the same tower, and those in the closest tower in η, are combined into a calorimeter electron cluster. The sampling resolution of the EM calorimeter is calculated from the detailed GEANT-based simulation [64]. The cluster energy is smeared with fractional resolution $\sigma_E/E = \sqrt{0.126^2/E_T + \kappa^2}$, where E_T is in GeV and $\kappa = (0.730 \pm 0.021)\%$ is determined by minimizing the χ^2 of the inclusive E/p distribution of electrons from the W-boson data sample (see Sec. VII). This model from Ref. [43] is improved in this analysis by increasing κ linearly by 0.05% per tower as a function of $|\eta|$. This modification takes into account the observed degradation of the EM calorimeter resolution with pseudorapidity, and produces acceptable χ^2 values for the E/p fits in the individual towers shown in Fig. S13 (see Sec. VII). The measured width of the $Z \to ee$ peak is found to be consistent with this resolution model.

The nominal number of radiation lengths in the calorimeter is tuned by a pseudorapidity-dependent correction of a few percent (see Sec. VII), based on the fraction of electrons with low E/p, which have a high leakage out of the CEM. The nominal number of radiation lengths in the silicon detector is also adjusted by a few percent (see Sec. VII) based on the fraction of radiative electrons, identified by high values of E/p.

The energy deposited by muons in the calorimeter is simulated using their measured distribution from an unbiased sample of cosmic rays [39, 43]. A simulation of the CDF II detector [86] based on GEANT [87, 88] is used to check the geometrical aspects of the custom simulation. The first-principles calculations of lepton and photon interactions performed in the custom simulation and the context of the CDF GEANT-based detector simulation are discussed at length in Refs. [39, 43].

Other particles in the event also deposit energy in the towers associated with the leptons. This energy flow, along with its dependence on the event topology, is measured from the W-boson data and modeled in the simulation. Its correlation with the lepton tower removal (Sec. VIII A) is also measured from the W-boson data and modeled. These measurements use towers rotated in azimuth from the lepton direction.

IV. PRODUCTION AND DECAY MODELS

The measurement of M_W at hadron colliders requires the modeling of W-boson production in high-energy hadron-hadron collisions, including a model of proton structure and of the W-boson decay to parametrise the spectra of the observables. Simulated samples of W and Z bosons are generated using the CTEQ6M [89] parton distribution functions (PDFs) extracted at next-to-leading order (NLO) in QCD, and the RESBOS generator [54–56], which uses perturbative QCD and a parametrization of nonperturbative QCD effects to calculate boson production and decay kinematics. The PHOTOS program [57] is used to simulate internal bremsstrahlung.

The model-dependent nature of the analysis implies that the robustness of the measurement is dependent on the reliability of the models in use, which, although being the state-of-the-art, are continuously being updated and

improved. The quoted uncertainties from those models are estimated using plausible assumptions in the context of the models themselves and, therefore, do not cover the possibility of significant updates. Future improvements or corrections in any relevant theoretical modeling can alter this result in a way that could reduce or enhance the observed discrepancy with the SM expectation, just as the SM expectation is also subject to improvements.

A. Parton distribution functions

At hadron colliders, the distribution of longitudinal momentum of W bosons is determined by the PDFs describing the probability density of the fraction x of a hadron's momentum carried by an interacting parton. Variations in the PDFs induce variations in the transverse kinematic distributions because of the incomplete lepton acceptance in the longitudinal direction [92]. Since the beginning of the analysis [39], the CTEQ6M PDFs, which have been used for event generation, have been superseded by other global fits to a broader set of more precise data. We consider the recent independent PDF fits performed by the ABMP16 [90], CJ15 [91], CT18 [61], MMHT2014 [62] and NNPDF3.1 [60] collaborations at NLO and NNLO in QCD. We study the effect of PDF variations by analysing pseudoexperiments in which simulated events have been reweighted using different PDF sets.

The accuracy of NNLO PDFs in describing the global data sets is expected to be higher than NLO sets due to their higher perturbative order. We use the NNPDF3.1 set to quantify the PDF uncertainty from the global fit. The NNPDF3.1 methodology captures the uncertainties in the data by fitting fluctuated replicas of the data including their correlations, which is a statistically rigorous procedure. A CT18 study [61] has found that at most about 30 parameters can be varied simultaneously in a global PDF fit, since additional parameters tend to fit statistical noise and destabilize the fit. On the other hand, a study [93] by the NNPDF group found that only 14 parameters are needed to capture the uncertainties in the MMHT2014 PDF set, and that 11 parameters are sufficient to capture the relevant uncertainties for electroweak observables [94]. We conservatively use a set of 25 symmetric NNPDF3.1 eigenvectors [93] constructed according to the prescription of Ref. [93], and obtain a PDF uncertainty of 3.9 MeV.

For a consistency check, we perform a comparative study using the following sets which are available at NNLO; CT18, MMHT2014 and NNPDF3.1. Using the RESBOS generator, we find the M_W central values from these PDF sets to be consistent within ± 2.1 MeV of their midpoint.

An additional consistency check is provided by comparing the M_W values from the following NLO PDF sets; ABMP16, CJ15, MMHT2014 and NNPDF3.1. We find that they are consistent within ± 3 MeV of their midpoint (within ± 6 MeV if CT18 is included, but this spread reduces substantially when going from NLO to NNLO PDFs, suggesting perturbative convergence). These checks show that the differences between PDF sets due to differences in parametrizations and more importantly, due to different choices of fitted data sets, induce M_W variations that are within the quoted uncertainty. For example, the CJ15 set includes all Tevatron data on the W-charge asymmetry, as well as the lepton-charge asymmetry from W boson decays and quasi-free neutron scattering data from the Jefferson Lab BONuS experiment [95, 96]. Inclusion of the W-charge asymmetry data set from the Tevatron improves the precision of the d/u quark distribution ratio at high x by a factor of three beyond the precision achieved after all the lepton-charge asymmetry data have already been included in the fit [91]. The d/u quark distribution ratio at high x most strongly determines the rate of W boson production at high rapidity, and therefore the PDF-dependent uncertainty induced by the limited detector acceptance for such bosons. The CJ15 set also uses about 50% more data than the other PDF sets, by including high-precision deeply-inelastic scattering measurements at slightly lower Q^2 and incorporating higher-twist effects [91] in their fitting procedure. Higher-twist effects are also included in the ABMP16 set, but not included in the CT18, MMHT2014 or NNPDF3.1 sets. The ABMP16 set does not include W-charge asymmetry data and deuteron target data, while the MMHT2014 set only includes the W-charge asymmetry data from 1 fb^{-1} of CDF data but not the full Run 2 statistics of D0 data, and does not include the BONuS data. They also use different PDF parameterizations and different treatments (or exclude) higher-twist effects. Given these differences in fitting methods and data sets, the consistency of M_W is an indication of the robustness with respect to PDF variations.

The PDF uncertainty from the CJ15 set is 2.9 MeV, which is smaller than our quoted uncertainty of 3.9 MeV based on the NNPDF3.1 set. As noted, the CJ15 set fits more global data of relevance to this measurement. Furthermore, NNPDF3.1 only uses a fraction of the data in the global fit, while the remainder are used for testing the neural network convergence. However, we choose to use the NNPDF3.1 set because of its higher perturbative accuracy (NNLO) relative to CJ15 (NLO).

We investigate the systematic uncertainty due to missing higher-order QCD effects by the standard method of varying the factorization and renormalization scales in RESBOS, and by comparing two event generators with different resummation and non-perturbative schemes. Both methods estimate that the effect of missing higher-order QCD effects is ≈ 0.4 MeV, which we take as negligible.

We correct the final W-boson mass measurement by using pseudoexperiments to compute the shift between CTEQ6M and NNPDF3.1NNLO, which is $+(3.3, 3.6, 3.0)$ MeV for the (m_T, p_T^ℓ, p_T^ν) fits. As our simulated templates are generated

with the CTEQ6M PDFs, we add these shifts to the fit results on data and quote the corrected M_W values with respect to the NNPDF3.1NNLO PDF set.

B. W and Z boson p_T

RESBOS uses the Brock-Landry-Nadolsky-Yuan form of the dimensionless nonperturbative function S to describe the boson p_T spectrum at low p_T,

$$S = \left[g_1 - g_2 \log \left(\frac{\sqrt{\hat{s}}}{2Q_0} \right) - g_1 g_3 \log \left(\frac{100\hat{s}}{s} \right) \right] b^2, \tag{S2}$$

where Q_0 is the cutoff parameter of 1.6 GeV, b is the impact parameter between the interacting partons, $\hat{s}$ (s) is the parton-parton (proton-antiproton) energy-squared in its center-of-momentum system, and g_1, g_2, and g_3 are parameters to be determined experimentally. Since the g_i parameters are completely correlated at fixed beam energy and boson mass, we fix g_1 and g_3 to their values from a global fit [55, 56]. We fit for g_2 using the dilepton p_T spectra from $Z \to ee$ and $Z \to \mu\mu$ candidate decays (Fig. S2), obtaining a statistical uncertainty on g_2 of 0.0072 GeV^2. An uncertainty on the difference between the p_T spectra of W and Z bosons results from the uncertainty on the g_3 parameter, which we take as ± 0.3 from the global fit [55, 56]. This variation of g_3 is found to be equivalent to a g_2 variation of ± 0.007 GeV^2 in terms of its effect on the M_W fit. These uncertainties on g_2 (from our data) and g_3 (from the global fit excluding our data) are propagated to M_W uncertainties and the latter are combined in quadrature, leading to uncertainties on M_W of 0.5, 2.2, and 0.5 MeV for the m_T, p_T^ℓ, and p_T^ν fits, respectively.

The boson p_T spectrum is sensitive to the value of the QCD coupling α_s for boson p_T above 5 GeV. Tuning the value of α_s to fit the $Z \to \ell\ell$ data results in uncertainties on M_W of 1.0, 3.2, and 1.2 MeV for the m_T, p_T^ℓ, and p_T^ν fits, respectively. Given the correlation coefficient of -0.71 between the uncertainties on the fitted values of g_2 and α_s [104], the net uncertainty due to modeling of the p_T^Z distribution is 0.7, 2.3, and 0.9 MeV for the m_T, p_T^ℓ, and p_T^ν fits, respectively.

The distribution of the dilepton angular variable

$$\phi_\eta^* = \tan\left(\frac{\pi - \Delta\phi^{\ell\ell}}{2} \right) \operatorname{sech}\left(\frac{\eta^- - \eta^+}{2} \right) \quad , \tag{S3}$$

introduced as a measure of the p_T^Z distribution that is insensitive to the magnitudes of the lepton momenta [103], is used as a consistency check of the simulation (see Fig. S2). Here $\Delta\phi^{\ell\ell}$ is the difference in the azimuthal angle between the two leptons, and $\eta^\pm$ are the pseudorapidities of the positive- and negative-charge lepton respectively. The use of the ϕ_η^* variable is a new feature of this analysis compared to the previous analysis [43].

We use the DYQT program [97–99] to investigate an additional source of uncertainty arising from the perturbative calculation of the ratio of the p_T^W and p_T^Z spectra. The DYQT program combines the $\mathcal{O}(\alpha_s^2)$ calculation at high values of boson p_T with the resummation of the logarithmically-enhanced $\mathcal{O}[\alpha_s^n \ln^m(p_T^2/M^2)]$ QCD contributions at small values of boson p_T up to NNLL. There are three scales associated with this differential cross section calculation: the renormalization scale μ_R at which α_s is evaluated, the factorization scale μ_F to which the QCD evolution of the PDFs is performed, and the resummation scale Q entering the resummation calculation. We vary these scales within the range $\frac{1}{4} < (Q, \mu_F, \mu_R)/m_{\text{boson}} < 1$ and use the central values $Q = \mu_F = \mu_R = \frac{1}{2} m_{\text{boson}}$. Propagating the envelope of the variations of the p_T^W/p_T^Z spectrum ratio due to these scale variations leads to uncertainties of 3.5 MeV, 10.1 MeV and 3.9 MeV on M_W from the m_T, p_T^ℓ, and p_T^ν fits respectively. We reduce these uncertainties by a factor of 4.4 by constraining the theoretical p_T^W spectrum with our measured p_T^W spectra, taking into account all the detector effects. Thus, the scale-variation uncertainty in the p_T^W/p_T^Z spectrum ratio leads to an additional uncertainty of 0.8 MeV for the m_T fit, 2.3 MeV for the charged lepton p_T fit, and 0.9 MeV for the neutrino p_T fit. The use of a theoretical calculation of the p_T^W/p_T^Z spectrum ratio to study its scale variation is a new feature of this analysis compared to the previous analysis [43].

The observed p_T^W spectrum is also sensitive to the calorimeter response and resolution parameters, as discussed in Sec. VIII B 6. Thus, the uncertainty in the theoretical p_T^W spectrum is correlated with the uncertainties in the calorimeter parameters. The quoted uncertainties from the calorimeter response and resolution in Sec. VIII B 6 take these correlations into account.

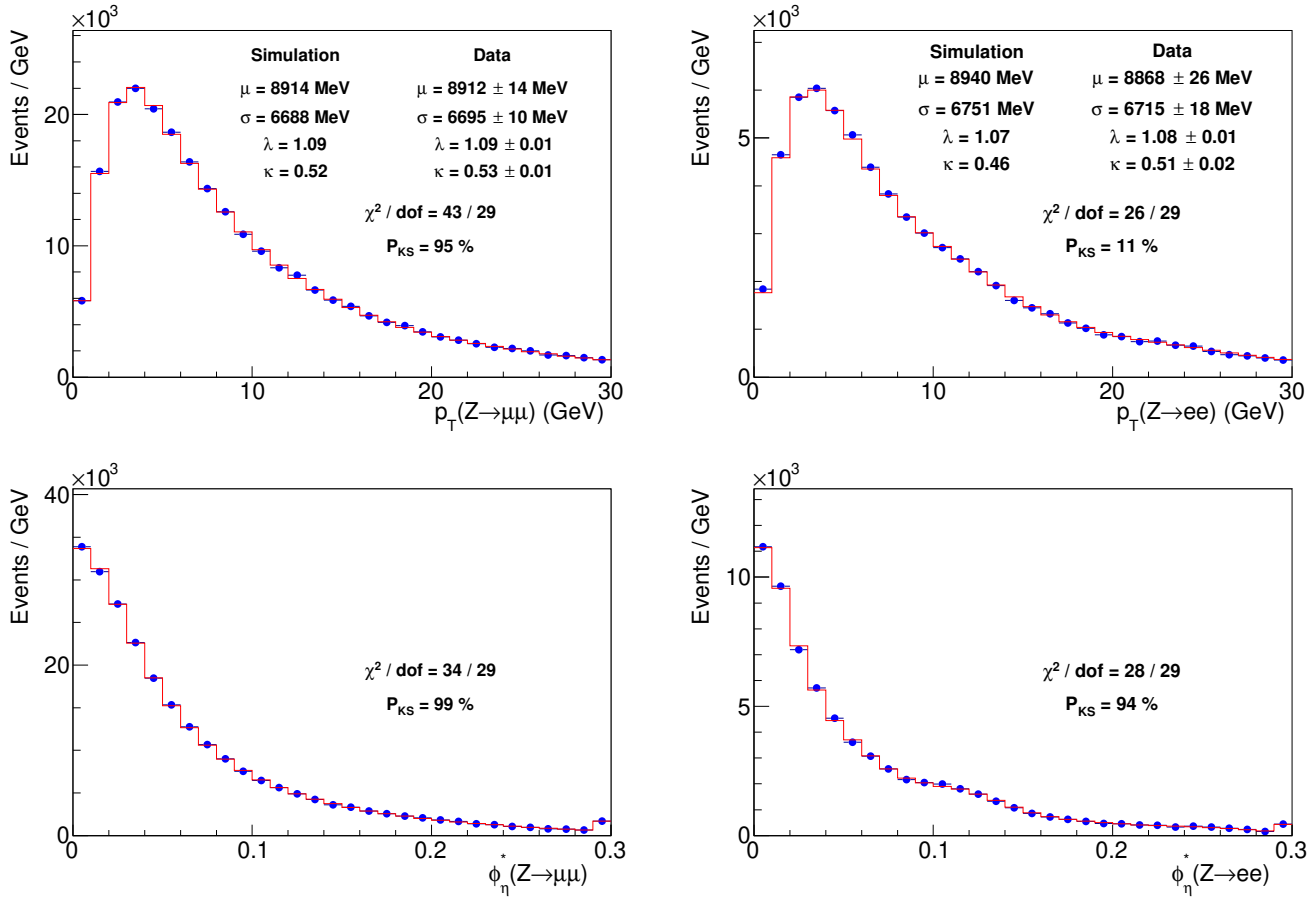

FIG. S2: Distributions of p_T^Z (top) and ϕ_η^* (bottom) from simulation (histogram) and data (circles) for Z-boson decays to $\mu\mu$ (left), and to ee (right). The p_T^Z distributions are used to fit for the nonperturbative parameter g_2 and for α_s, and the ϕ_η^* distributions provide a consistency check. The ϕ_η^* distribution in the electron channel is modulated by the periodic azimuthal acceptance of the 24 calorimeter wedges. In these and other figures, "P_{KS}" refers to the Kolmogorov-Smirnov probability of agreement between the shapes of the data and simulated distributions.

C. QED radiation

As described in Ref. [43], final-state radiation (FSR) of photons is simulated using the PHOTOS program [57], because PHOTOS can be interfaced with the RESBOS event generator. FSR photons are produced with an energy cutoff of $E_\gamma > 0.4$ MeV. Tripling the E_γ threshold shifts the value of M_W by 1 MeV, which is taken as a systematic uncertainty on the choice of E_γ threshold. A comparison of FSR from the PHOTOS and HORACE programs [58] finds consistency at the level of 0.7 MeV [59], which is taken as the uncertainty in the FSR algorithm. The HORACE program additionally includes the exact NLO QED calculation, the effects of initial-state radiation (ISR) and interference between ISR and FSR. Calibration of the PHOTOS program to the more accurate HORACE program yields a correction of $4 \pm 2_{\rm MC\ stat}$ MeV which is propagated to the M_W result. Uncertainties on the HORACE simulation are estimated to be 1 MeV [43]. As in Ref. [43], internal photon conversion [100] is simulated with an uncertainty on M_W of 1 MeV. The combined uncertainty on M_W due to QED radiation is 2.7 MeV in both the electron and muon channels and is correlated between the channels and the fit distributions.

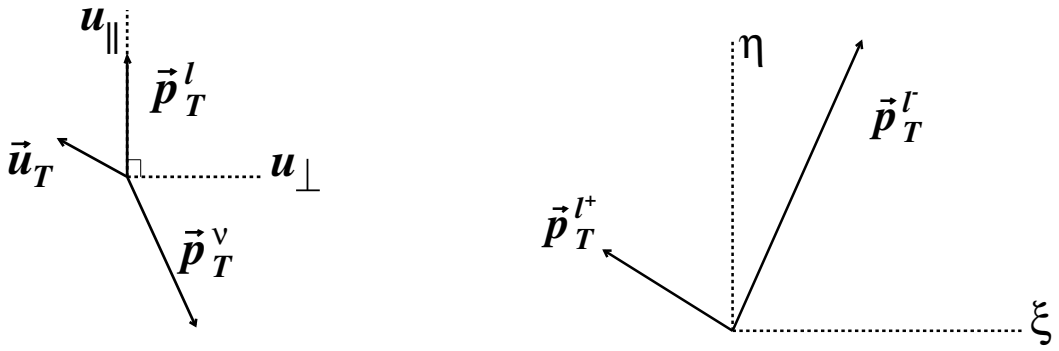

FIG. S3: (left) Sketches of typical transverse vectors associated to quantities reconstructed in a W-boson event, with the recoil hadron momentum ($\vec{u}_T$) separated into axes parallel ($u_{||}$) and perpendicular ($u_{\perp}$) to the charged lepton. (right) Illustration of the η and ξ axes in Z boson events.

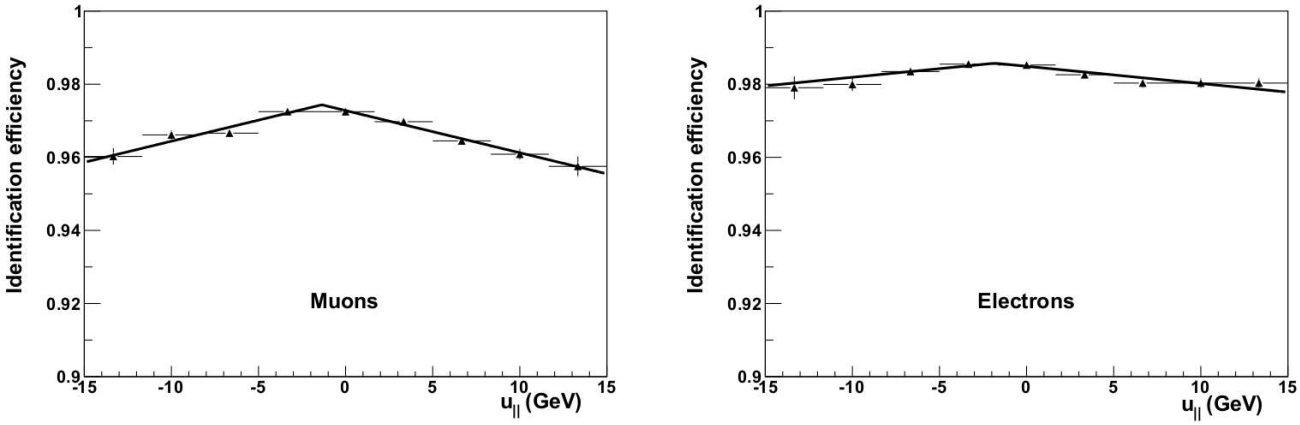

FIG. S4: Muon (left) and electron (right) identification efficiency as a function of the recoil component in the direction of the lepton ($u_{||}$), as measured in $Z \to \ell\ell$ data using the tag-probe technique. The piece-wise linear fits are used to model the lepton efficiencies in the simulation.

V. W AND Z BOSON EVENT SELECTION

The lepton selection criteria follow Ref. [43]. The criteria can be degraded by the presence of nearby energy associated with the hadronic recoil. Hence, the lepton identification efficiency depends on the projection of the recoil along the direction of the lepton, $u_{||}$, as shown in Fig. S3. The procedure for measuring this efficiency is described in Ref. [43], wherein $Z \to \ell\ell$ events with one identified *tag* lepton provide the second *probe* lepton whose efficiency is measured. The fraction of probe leptons passing the full W-boson candidate criteria (shown in Fig. S4) is fitted with the parametrization $\varepsilon_u = A[1 + m|u_{||} - d|]$, where A is an irrelevant normalization, m is the slope parameter versus $u_{||}$ and d is the offset parameter. The fits are used to model the lepton efficiencies in the simulation. The reduction in efficiency for large negative values of $u_{||}$ is due to an increase in overall hadronic activity in the event, verified by studying the efficiency with the PYTHIA [101, 102] Monte Carlo that includes hadrons from the breakup of the proton and the initial-state radiation.

The following parameter values and statistical uncertainties are determined from the data and used in the simulation: $A = 98.6\%$, $m = (0.048 \pm 0.006)\%/\text{GeV}$, and $d = (-1.8 \pm 0.9)$ GeV for the electron channel, and $A = 97.4\%$, $m = (0.1200 \pm 0.0054)\%/\text{GeV}$, and $d = (-1.40 \pm 0.24)$ GeV for the muon channel. The parameters m and d have a correlation coefficient of $-0.41(-0.18)$ for the electron (muon) channel. For a 1σ increase in m, the variations in the m_T, p_T^{ℓ}, and p_T^{ν} fits are -0.4 (-0.4), 0.0 (0.0) and -1.5 (-1.5) MeV respectively in the electron (muon) channel. For a 1σ increase in d, the variations in the m_T, p_T^{ℓ}, and p_T^{ν} fits are -0.5 (-0.3), 1.3 (1.0), and -2.8 (-1.7) MeV respectively in the electron (muon) channel. These systematic uncertainties are uncorrelated between the electron

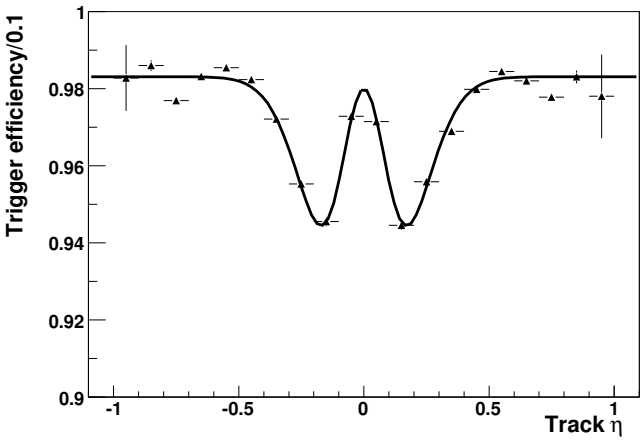

FIG. S5: Track trigger efficiency as a function of track η for electrons identified in the calorimeter. The measurement used W-boson events collected with a trigger with no track requirement.

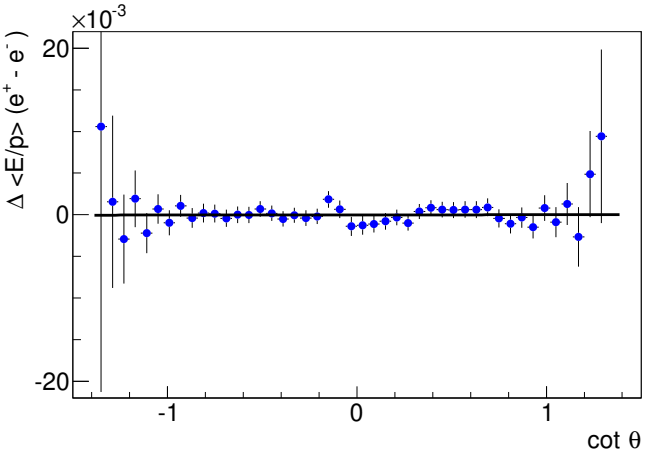

FIG. S6: Difference in $\langle E/p \rangle$ between positrons and electrons as a function of $\cot\theta$, and its linear fit. The curvature corrections given in Eq. (S4) have been applied.

and muon channels.

The η-dependent efficiency for reconstructing leptons due to track trigger requirements is measured using W-boson events collected with a trigger with no track requirement as described in Ref. [43]. The efficiency is described by a double-Gaussian function (Fig. S5) which captures the effects of COT structural supports. The uncertainty in the trigger efficiency measurement has a negligible impact on the M_W measurement.

VI. MUON MOMENTUM MEASUREMENT

The momentum of a muon produced in a $p\bar{p}$ collision is measured using a helical track fit to the hits in the COT, with a constraint to the transverse position of the beam for promptly produced muons [39, 43], i.e., muons produced directly in the hard scatter. To maximize accuracy and precision, we perform a momentum calibration using data samples with muonic decays of J/ψ mesons, $\Upsilon(1S)$ mesons, and Z-bosons. All calibrations are based on maximum-likelihood fits to the data spectra using simulated templates of the line-shapes. The templates are indexed by the COT momentum scale when fitting $J/\psi \to \mu\mu$ and $\Upsilon(1S) \to \mu\mu$ data, by the Z-boson pole mass when fitting the $Z \to \ell\ell$ data, and by the CEM energy scale when fitting the E/p spectrum. Uniformity of the calibration is significantly enhanced by an alignment of the COT wire-positions using cosmic-ray data [51]. The cosmic-ray alignment was performed [65] for the complete data-taking period corresponding to the data used in this analysis. A number of improvements were incorporated in the latest alignment procedure [65] compared to the procedure presented in Ref. [43]. As a result, residual biases that were not resolved in the previous iteration of the alignment were eliminated in this iteration [65].

The cosmic-ray-based alignment is used in track reconstruction and validated with tracks from electrons and positrons from W-boson decays. Global misalignments to which the cosmic ray reconstruction is insensitive are corrected at the track level using the difference in $\langle E/p \rangle$ between electrons and positrons, where E/p is in the range 0.9–1.1. Additive corrections are applied to q/p_T, a quantity proportional to the track's curvature, where q is the particle charge,

$$q\Delta p_T^{-1} = (43.2\cot^2\theta - 12.6 + B\cot\theta)\ \mathrm{PeV}^{-1} \quad . \tag{S4}$$

The difference in $\langle E/p \rangle$ between positrons and electrons as a function of $\cot\theta$ [50] is shown in Fig. S6 after the correction of Eq. (S4). The uncertainty on parameter $B = (0 \pm 4)\ \mathrm{PeV}^{-1}$, which induces an uncertainty of 0.8 MeV on M_W, is given by the statistical uncertainty on the slope in Fig. S6. The uncertainty in the other two parameters in Eq. (S4) cancels when averaged over the symmetric production of W^+ and W^- bosons in the $p\bar{p}$ collisions at the Tevatron.

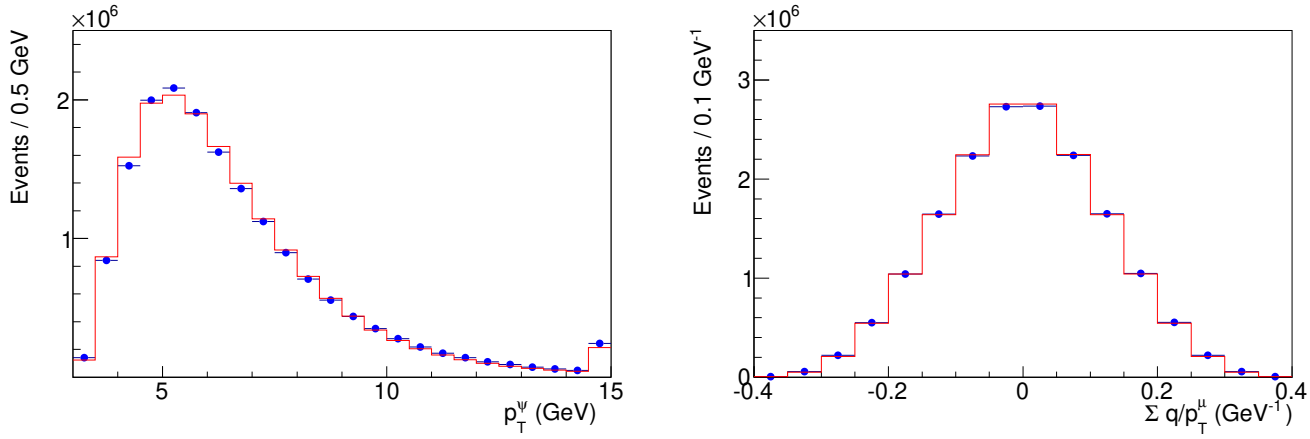

FIG. S7: Distribution of dimuon p_T (left) and $\Sigma(q/p_T^{\mu})$ (right) in the data (circles) and the simulation of $J/\psi \to \mu\mu$ decays (histogram). The data distributions are background-subtracted using events in the mass range 3.17–3.31 GeV.

A. $J/\psi \to \mu\mu$ calibration

The $J/\psi \to \mu\mu$ candidate selection [43] yields a sample of 18 million $J/\psi \to \mu\mu$ decays. The precisely known mass of the J/ψ meson, $M_{J/\psi} = 3096.916 \pm 0.011$ MeV, its narrow width, $\Gamma_{J/\psi} = 92.9 \pm 2.8$ keV [10], and its large production rate makes this sample useful for the precise calibration of the track momenta. In addition to the extraction of a global momentum scale factor, the $J/\psi \to \mu\mu$ sample is used to measure the spatial variation of the magnetic field, biases in the track parameters due to COT deformations, and a correction to the amount of ionizing material upstream of the COT. These corrections are measured by fitting the dimuon mass distribution for the J/ψ mass as a function of the appropriate geometrical or kinematic quantity.

We use the sample of $J/\psi \to \mu\mu$ decays generated with PYTHIA [101, 102] described in Ref. [43]. The kinematic distributions of the generated sample are tuned to match the data, as shown in Fig. S7. The generator does not model QED final-state radiation, so we simulate it using the following next-to-leading order (NLO) expression for the Kuraev-Fadin form factor [105, 106]:

$$\begin{aligned} f_{\mu}^{\mu,\mathrm{NLO}}(x) &= f_{\mu}^{\mu,\mathrm{LO}}(x)\left[1+\frac{3}{8}\beta-\frac{\beta^2}{48}\left(\frac{L}{3}+\pi^2-\frac{47}{8}\right)\right] \\ &- \frac{1}{4}\beta\,(1+x)+\frac{\beta^2}{32}\left[-4\,(1+x)\ln(1-x)-\frac{1+3x^2}{1-x}\ln x-5-x\right], \end{aligned} \tag{S5}$$

where $\pi\beta = 2\alpha_{\mathrm{EM}}(L-1)$ and $L = 2\ln\frac{Q}{m_{\mu}}$. The function $f_{\mu}^{\mu}(x)$ denotes the $\mu \to \mu$ fragmentation probability where x is the energy fraction retained by the muon, $Q = m_{J/\psi,\Upsilon}$ is the factorization scale set to the mass of the resonance, and at leading order (LO) in QED, the following relation holds

$$f_{\mu}^{\mu,\mathrm{LO}}(x) = \frac{1}{2}\beta(1-x)^{\beta/2-1} \quad . \tag{S6}$$

The curvature of the simulated muon track is increased according to the energy fraction taken by the radiation.

The reconstruction of charged-particle trajectories includes a spatial map of the magnetic field. The variation of the measured momentum scale as a function of the mean $\cot\theta$, for muons with small longitudinal opening angle $|\Delta\cot\theta| < 0.1$, reflects the effect of residual, uncorrected nonuniformities in the magnetic field [39, 43]. The observed dependence is used to derive the following correction to the measured track p_T in data,

$$p_T^{\mathrm{cor}} = (1 - 0.00031\cot\theta + 0.00069\cot^2\theta)\; p_T. \tag{S7}$$

After applying this correction, the relative momentum correction to each muon, $\Delta p/p$, shows no significant dependence on $\cot\theta$ (Fig. S8).

A small inaccuracy of the stereo angle of the COT sense wires would induce a longitudinal scale factor on $\cot\theta$, and lead to a quadratic variation of $\Delta p/p$ with $\Delta\cot\theta$. A linear dependence of $\Delta p/p$ on $\Delta\cot\theta$ would be induced by

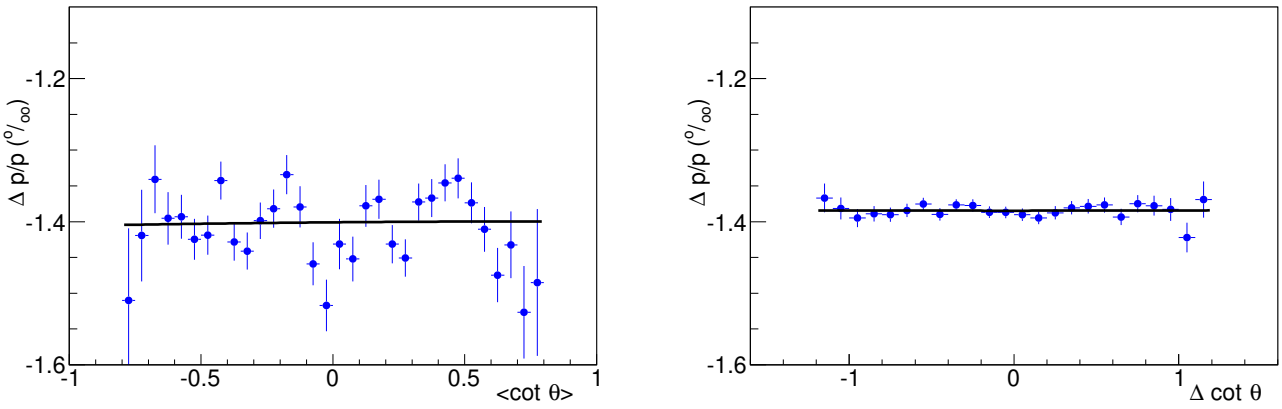

FIG. S8: (left) Measured $\Delta p/p$ (per mille) as a function of the mean $\cot\theta$ of the muon pair from J/ψ decay, after requiring $|\Delta\cot\theta| < 0.1$ and including corrections. (right) Measured $\Delta p/p$ as a function of $\Delta\cot\theta$ of the muon pair from J/ψ decay, after including corrections.

a relative rotation of the east and west endplates (twist) of the COT. The following corrections to the track $\cot\theta$ and curvature (c) are made:

$$\cot\theta \;\rightarrow (1+s_z)\cot\theta\;, \qquad c \;\rightarrow c - t\cot\theta, \tag{S8}$$

with the COT longitudinal-scale parameter $s_z = (45 \pm 9_{\rm stat})$ parts per million (ppm) and the COT twist correction $t = (3.6 \pm 0.6_{\rm stat}) \times 10^{-6}$ m^{-1}. Figure S8 shows that these corrections eliminate the dependence of $\Delta p/p$ on $\Delta\cot\theta$ originally present due to these global COT deformations [39, 43].

An inaccuracy in the modeling of the ionizing material in the tracking detectors induces a linear dependence of $\Delta p/p$ on $\langle 1/p_T^\mu\rangle$, the mean unsigned curvature of the two muons [39, 43]. A scale factor of 0.974 applied to the simulated amount of ionizing material eliminates such dependence, as shown in Fig. 2 (left) of the main text. The 2.6% relative correction to the passive material removes a linear slope with an end-to-end variation of 80 ppm. Using the post-correction linear fit to extrapolate to zero mean curvature, we find $\Delta p/p = (-1401 \pm 2_{\rm stat} \pm 11_{\rm slope/material})$ ppm. Examples of $J/\psi \rightarrow \mu\mu$ mass fits are shown in Fig. S9.

Systematic uncertainties on the momentum-scale correction extracted from $J/\psi \rightarrow \mu\mu$ decays are listed in Table S2. A major reduction in the systematic uncertainty with respect to Ref. [43] is due to the use of the NLO QED Kuraev-Fadin form factor of Eq. (S5) rather than the leading-order (LO) expression of Eq. (S6). The QED systematic uncertainty from missing higher orders is estimated by evaluating the effect of the β^2 terms in Eq. (S5), and is found to be 1 ppm.

The correction for magnetic-field nonuniformity to $J/\psi, \Upsilon \rightarrow \mu\mu$ and $W(Z) \rightarrow \ell\nu(\ell\ell)$ data shifts the respective mass determinations in the same direction, resulting in a partial cancellation of the corresponding uncertainty. Propagating the uncertainty on the magnetic field correction results in a residual uncertainty of 13 ppm on $\Delta p/p$, reflecting the difference in the polar-angle distributions of the charged leptons in the two samples.

The purely statistical uncertainty of 2 ppm on the $\Delta p/p$ correction at zero curvature is found by fixing the slope in the fit to $\Delta p/p$ as a function of $\langle 1/p_T^\mu\rangle$. The uncertainty in the ionizing material correction dominates the uncertainty of 11 ppm in the extrapolation.

The scale factor on the COT hit-resolution (see Sec. III) is determined using the $\Sigma\chi^2$ of the five highest momentum bins in the $\langle 1/p_T^\mu\rangle$-binned J/ψ mass fits, which are most sensitive to the hit resolution. The rms of the bin-to-bin variation in this scale factor is 0.9%, which translates into an uncertainty on $\Delta p/p$ of 10 ppm.

A linear background model is included in the $J/\psi \rightarrow \mu\mu$ mass-fitting templates. The shape of the background is separately constrained by widening the fitting region to include sidebands. The background parameters are tuned by χ^2 minimization while repeating the template fit including the wider sidebands. This procedure allows the sidebands to constrain the background normalization and slope under the peak, independently from the momentum scale. The background parameters are found to be statistically uncorrelated. With the background thus determined, it is fixed in the final template fit for the momentum scale using the default fitting region. The uncertainty in $\Delta p/p$ due to background modeling is 7 ppm, dominated by the uncertainty in the slope of the background.

The uncertainty in the COT longitudinal scale correction s_z in Eq. (S8) propagates to an uncertainty on $\Delta p/p$ of 4 ppm. The systematic uncertainty due to the twist (t) correction is negligible.

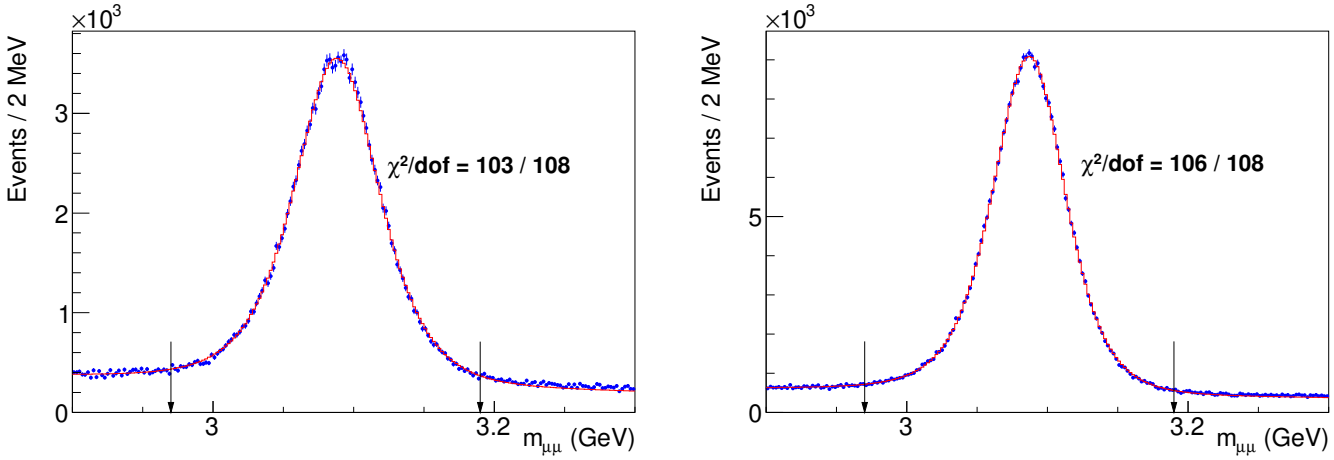

FIG. S9: Representative dimuon mass fits (histogram) to data (circles), in the ranges $\langle 1/p_T^\mu \rangle = (0.15, 0.1625)$ GeV^{-1} (left) and $\langle 1/p_T^\mu \rangle = (0.1875, 0.2)$ GeV^{-1} (right) of the $J/\psi \to \mu\mu$ data. The arrows enclose the fit range. Each fitting template includes a linear background shape which is separately constrained by including wider sidebands in the fit region.

The muon p_T threshold is increased by 200 MeV to check the sensitivity to unmodeled effects such as trigger efficiencies; the resulting mismodeling visibly distorts the simulation-to-data agreement in the $p_T(J/\psi)$ distribution compared to Fig. S7. The change in $\Delta p/p$ of 18 ppm is taken as the associated uncertainty. Increasing the muon p_T threshold by more than 200 MeV does not change the systematic variation, because the latter is induced by the displacement of the third bin from the right in Fig. 2 (left) of the main paper, relative to the fitted straight line. This point is eliminated when the muon p_T threshold is increased by 200 MeV.

The fit range is changed by ±20% to check the sensitivity to the modeling of resolution tails. The 2 ppm change in $\Delta p/p$ is taken as the uncertainty. Since templates are simulated in 4 ppm steps of $\Delta p/p$, we take half the step size as a systematic uncertainty due to the finite step size. Finally, the uncertainty on the known value of the J/ψ mass contributes 4 ppm to the uncertainty on $\Delta p/p$.

B. $\Upsilon \to \mu\mu$ calibration

The $\Upsilon(1S) \to \mu\mu$ sample provides a valuable additional source of calibration. The $\Upsilon(1S)$ meson mass of $M_\Upsilon = 9460.30 \pm 0.26$ MeV [10] lies between the J/ψ meson mass and the W and Z boson masses, providing an important intermediate point to the calibration. Additionally, since all Υ mesons are produced promptly, the transverse beam position can be added as a constraint (beam constraint) in the reconstruction of their decay products, reproducing the reconstruction procedure for tracks from W and Z bosons and allowing a consistency check of the beam-constraint procedure [107]. The selection of the $\Upsilon(1S) \to \mu\mu$ candidates is described in Ref. [43].

We use PYTHIA [101, 102] to generate a sample of $\Upsilon(1S) \to \mu\mu$ decays. As with the $J/\psi \to \mu\mu$ decays, we simulate QED radiation in $\Upsilon(1S) \to \mu\mu$ decays using the NLO Kuraev-Fadin form factor of Eq. (S5), which again represents an update compared to [43] where the LO Kuraev-Fadin form factor of Eq. (S6) was used. The generator is tuned to improve the modeling of the meson momentum and polarization, as described in Ref. [43]. After this tuning, the kinematic properties of the Υ and the final-state muons are well described, as shown in Fig. S10.

The Υ data are corrected for the magnetic field nonuniformity measured in J/ψ data (see Sec. VI A). By fitting for $\Delta p/p$ as a function of $\langle 1/p_T \rangle$, we find that the ionizing material scale factor determined with J/ψ data also makes the fitted Υ mass values independent of $\langle 1/p_T \rangle$, demonstrating consistency between the two calibration samples, as shown in Fig. S11.

Allowing for differences in the phase space populated by the muons in the various samples, we measure the COT longitudinal scale and twist parameters of Eq. (S8) in $\Upsilon \to \mu\mu$ data, finding $s_z = (-230 \pm 100_{\rm stat})$ ppm and $t = (7.0 \pm 1.2_{\rm stat}) \times 10^{-6}$ m^{-1} for muon tracks with the beam constraint. The measurements of $\Delta p/p$ versus $\Delta \cot\theta$

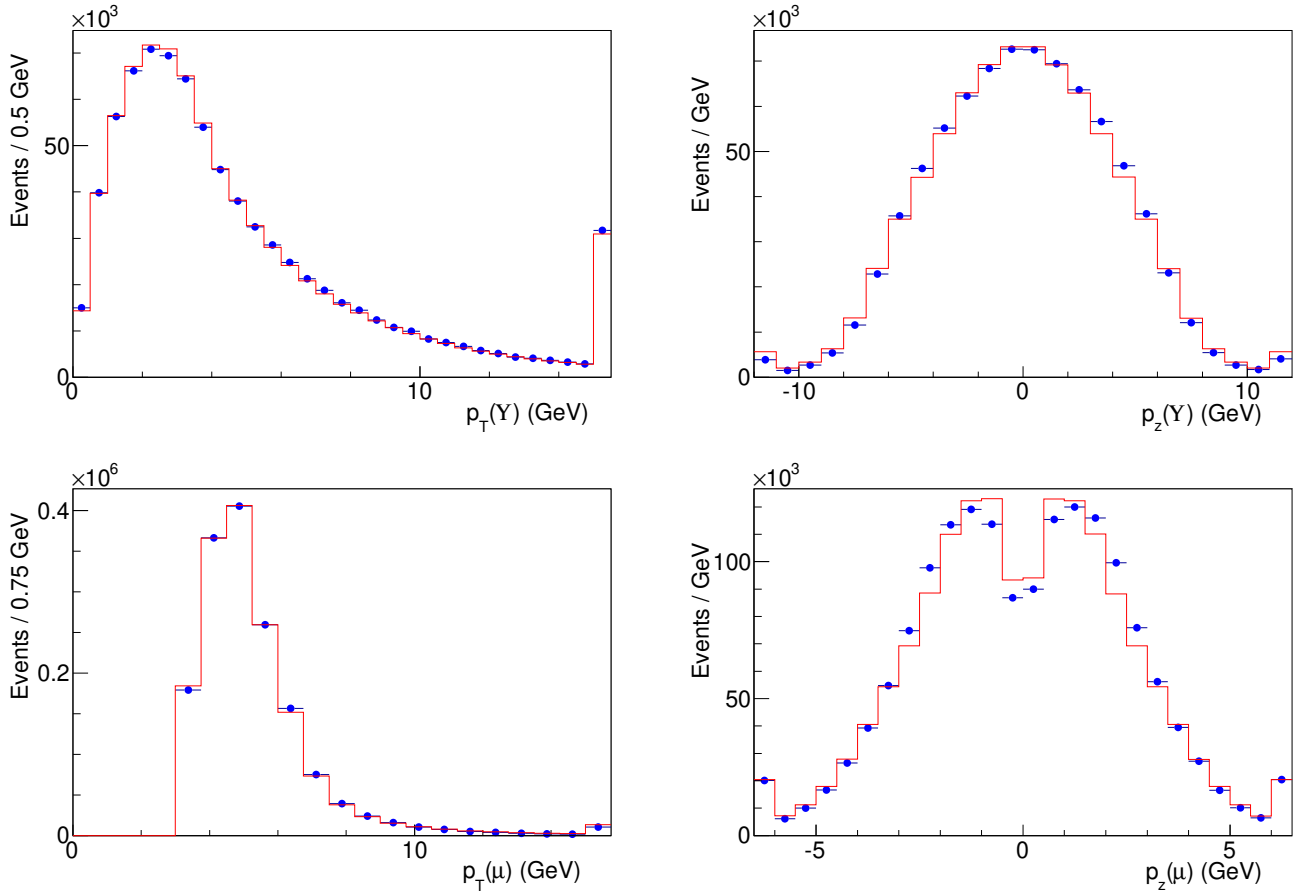

FIG. S10: Distributions of p_T (left) and p_z (right) for the Υ (top) and the decay muons (bottom) in the data (circles) and the tuned simulation of Υ decays (histogram). The data distributions correspond to the mass range $9.30 - 9.56$ GeV and are background-subtracted using events in the mass ranges $9.17 - 9.3$ GeV and $9.56 - 9.69$ GeV. The lowest and highest bins contain the underflows and overflows respectively.

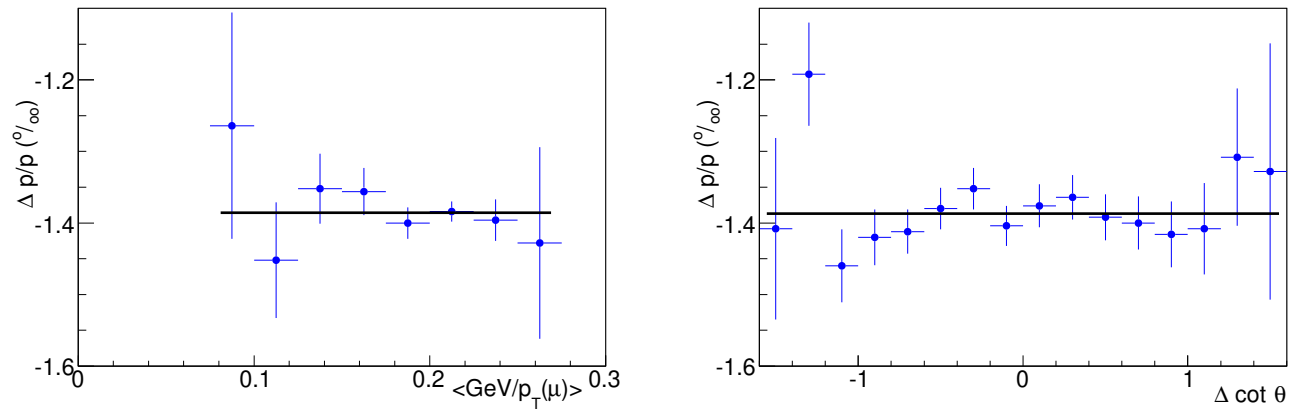

FIG. S11: Fractional momentum shift $\Delta p/p$ (per mille) from $\Upsilon \to \mu\mu$ data as a function of $\langle 1/p_T^\mu \rangle$ (left) and $\Delta \cot\theta$ (right). The measurements include corrections to the ionization energy loss determined from $J/\psi \to \mu\mu$ decays that remove $\langle 1/p_T^\mu \rangle$ dependence, and to the COT scale and twist determined from $\Upsilon \to \mu\mu$ decays that remove $\Delta \cot\theta$ dependence. Fits to a constant are overlaid on the plots as a visual aid.

TABLE S2: Fractional uncertainties, in parts per million (ppm), on the tracker momentum scale determined from the J/ψ and $\Upsilon(1S)$ meson masses reconstructed in dimuon decays. The last column shows the correlation coefficient between the J/ψ and Υ results. The tracks in the $J/\psi \to \mu\mu$ sample are not beam-constrained (NBC) while the tracks in the $\Upsilon(1S) \to \mu\mu$ sample may be beam-constrained (BC). Also shown in the "correlation" column is the component of the total uncertainty that is correlated between the J/ψ and Υ determinations, which is 16 ppm.

Source	J/ψ (ppm)	Υ (ppm)	Correlation (%)
QED	1	1	100
Magnetic field non-uniformity	13	13	100
Ionizing material correction	11	8	100
Resolution model	10	1	100
Background model	7	6	0
COT alignment correction	4	8	0
Trigger efficiency	18	9	100
Fit range	2	1	100
$\Delta p/p$ step size	2	2	0
World-average mass value	4	27	0
Total systematic	29	34	16 ppm
Statistical NBC (BC)	2	13(10)	0
Total	29	36	16 ppm

from beam-constrained $\Upsilon \to \mu\mu$ data used to obtain these corrections are shown in Fig. S11, after the corrections are applied.

The COT longitudinal scale s_z and twist parameter t need not be identical for the J/ψ and Υ samples because the track selection criteria are slightly different. The COT contains eight superlayers with 12 sense wires each. Since the J/ψ mesons are not all promptly produced, their muon tracks are not beam-constrained. To ensure optimal momentum resolution, all eight superlayers are required to contribute hits to these tracks. In comparison, the tracks in the Υ, Z- and W-boson samples are required to have at least 6 superlayers contributing hits, which ensures stable reconstruction efficiency while the beam constraint improves the momentum resolution. The innermost superlayer, which contributes to the measurement of the longitudinal coordinate due to its 2° stereo angle, has an inefficiency of $\approx 1\%$ due to its high occupancy. Since the stereo angle of each superlayer has been calibrated to about 1% of itself, a 1% inefficiency can induce a difference of $\mathcal{O}(100$ ppm) in s_z between the two track selections. The twist parameter t corresponds to a relative rotation of ± 6 μrad (± 12 μrad) of the longitudinal endplates of the COT in the J/ψ (Υ) sample, equivalent to a ± 8 μm (± 16 μm) east-west endplate twist at the COT outer radius. The small difference between samples is again consistent with selection differences and the precision of the relative east-west endplate alignment.

The longitudinal position calibration of the COT, while relevant for extracting information on track curvature from the $J/\psi \to \mu\mu$ and $\Upsilon \to \mu\mu$ mass measurements, is ultimately irrelevant for the M_W measurement since the latter depends only on the track p_T and the hadronic recoil measurements. The longitudinal position calibration obtained from the BC Υ sample is used for the Z-boson mass measurements. Similarly, the twist parameter t is ultimately irrelevant since its effect is antisymmetric in $\cos\theta$ and cancels when averaged over the polar angle distribution. It is incorporated in the alignment solely to monitor and improve the uniformity of the $J/\psi \to \mu\mu$ and $\Upsilon \to \mu\mu$ samples.

The measurements of $\Delta p/p$ with unconstrained (NBC) and beam-constrained (BC) tracks are consistent as shown in Fig. S12 and Table S3 (their difference is $[9 \pm 9_{\rm stat}]$ ppm, where the statistical error on the difference is due to the beam constraint and is equal to the quadrature difference of the respective statistical errors). The systematic uncertainties on these measurements are evaluated mirroring the procedure adopted from the J/ψ-based calibration and are detailed in Table S2. The BC $\Upsilon \to \mu\mu$ sample is divided into two equal size sub-samples to check the stability of the momentum scale versus time and versus instantaneous luminosity. The momentum scales are consistent within the statistical uncertainty; the difference between the later and earlier datasets is $(\frac{\Delta p}{p})_{\rm later} - (\frac{\Delta p}{p})_{\rm earlier} = (23 \pm 22_{\rm stat})$ ppm and the difference between the higher and lower instantaneous-luminosity datasets is $(\frac{\Delta p}{p})_{\rm higher} - (\frac{\Delta p}{p})_{\rm lower} = (22 \pm 22_{\rm stat})$ ppm (the later dataset has a higher average instantaneous luminosity).

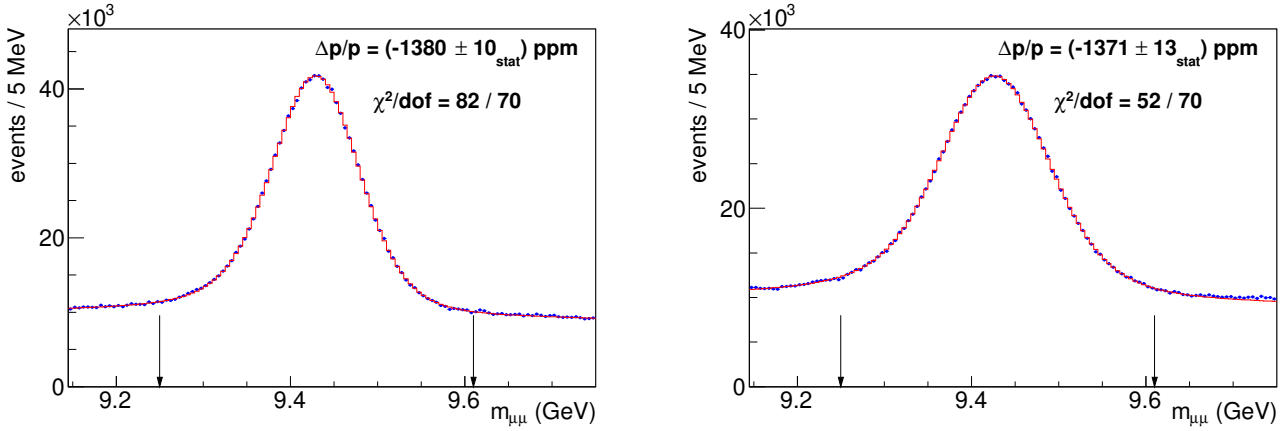

FIG. S12: Distribution of dimuon mass for the best-fit templates (histograms) and the data (circles) in the $\Upsilon \to \mu\mu$ sample used to calibrate the muon momentum scale. The muon tracks are reconstructed with (left) or without (right) a constraint to the beam position in the transverse plane. The arrows enclose the fit range. Each fitting template includes a background shape which is separately constrained by including wider sidebands in the fit region.

C. Combination of J/ψ and Υ calibrations

Since the muons in the $J/\psi \to \mu\mu$ sample are not beam-constrained, we first combine the results from J/ψ and NBC Υ meson fits from Table S3 to check their consistency. Taking the correlations listed in Table S2 into account, we obtain

$$[\Delta p/p]_{J/\psi+\mathrm{NBC}\ \Upsilon} = (-1392 \pm 2_{\mathrm{stat}} \pm 26_{\mathrm{syst}})\ \mathrm{ppm}\ . \tag{S9}$$

The two NBC measurements are consistent within 0.7σ.

Since the W and Z boson samples use beam-constrained tracks, the combined momentum scale applied to these measurements is based on measurements of J/ψ and BC Υ mesons, yielding

$$[\Delta p/p]_{J/\psi+\mathrm{BC}\ \Upsilon} = (-1393 \pm 2_{\mathrm{stat}} \pm 26_{\mathrm{syst}})\ \mathrm{ppm} = (-1393 \pm 26)\ \mathrm{ppm}\ , \tag{S10}$$

with a combination χ^2-probability of 51% taking the correlations listed in Table S2 into account. The $J/\psi \to \mu\mu$ and BC $\Upsilon \to \mu\mu$ measurements contribute weights of 62% and 38%, respectively.

In our previous analysis [43], an additional systematic uncertainty was quoted to cover an inconsistency between the NBC and BC $\Upsilon \to \mu\mu$ mass fits. In this analysis we resolve the inconsistency caused by the beam-constraining procedure, eliminating the additional systematic uncertainty and increasing the measured M_W value by ≈ 10 MeV. The beam-constraining procedure in the CDF track reconstruction software extrapolates the tracks found in the COT inward to the transverse position of the beamline. This extrapolation can and should take into account the energy loss in the material inside the inner radius of the COT (i.e., the beampipe, the silicon vertex detector and its services) to infer and update the track parameters at the beam position before applying the beam constraint. However, this update had been deactivated in the reconstruction software used for the previous analysis. By activating this updating feature of the extrapolator, the flaw in the BC $\Upsilon \to \mu\mu$ mass is corrected, which changes the momentum scale derived from it.

D. $Z \to \mu\mu$ mass measurement and calibration

The $Z \to \mu\mu$ data sample is selected following Ref. [43] and a blinded mass fit is performed (see Sec. I) using the momentum calibration given in Eq. (S10). The $Z \to \mu\mu$ invariant mass templates are produced from the custom simulation using the RESBOS event generator. The PHOTOS program is used to generate FSR photons and the mass shift is calibrated to the HORACE generator (Sec. IV). A binned maximum likelihood fit in the range 83 190 $< m_{\mu\mu} <$ 99 190 MeV (Fig. 3 of the main text) yields the mass measurement in the muon decay channel

$$M_Z = 91\ 192.0 \pm 6.4_{\mathrm{stat}} \pm 4.0_{\mathrm{syst}}\ \mathrm{MeV}\ . \tag{S11}$$

This result is the most precise determination of M_Z at a hadron collider and is in good agreement with the world-average value of $M_Z = 91\,187.6 \pm 2.1$ MeV [10], providing a sensitive consistency check of the momentum calibration. Systematic uncertainties on M_Z are due to uncertainties on the momentum calibration from Eq. (S10) (2.3 MeV), the COT global longitudinal scale parameter s_z from Eq. (S8) as determined using BC $\Upsilon \to \mu\mu$ data (1.0 MeV), and QED radiative corrections (3.1 MeV).

Combining this measurement with the calibration of Eq. (S10) from J/ψ and Υ data, and taking the COT global longitudinal scale and QED uncertainties to be fully correlated, we obtain

$$[\Delta p/p]_{J/\psi+\Upsilon+Z} = (-1389 \pm 25) \text{ ppm} . \tag{S12}$$

This momentum calibration is applied to the W-boson data for the M_W measurement.

VII. ELECTRON MOMENTUM MEASUREMENT

An electron radiates bremsstrahlung photons as it traverses the approximately 19% of a radiation length in the tracking volume [39], which degrades its track momentum resolution. Most of these photons are coalesced with the electron shower in the calorimeter, therefore we use the higher-resolution calorimeter energy measurement for the M_W and M_Z fits. The calibration of the track momentum p is transferred to the calorimeter energy E by fitting the distribution of their ratio, E/p. The mean of the ratio is used to improve the spatial and temporal uniformity of the calorimeter response, by applying corrections as functions of electron position and experiment running time. The distribution of the ratio is also used to determine the amount of radiative material upstream and in the calorimeter. The calorimeter calibration is verified by measuring the mass of the Z boson in $Z \to ee$ events. After this validation, the M_Z measurement is used as an additional calibration source for the M_W measurement.

A. E/p calibration

Following event reconstruction [77], the mean E/p in the range 0.9–1.1 is used to correct 1–2% response variations in electron-energy measurement in the data. These variations are mapped as functions of distance from tower edges in ϕ and z and corrected following Refs. [39, 43]. The spatial uniformity calibration has improved because of the increased sample size of the data. Furthermore, a temporal uniformity calibration of the EM calorimeter is introduced in this analysis; assuming azimuthal symmetry, the calorimeter response in each longitudinal tower is studied as functions of experiment operational time, and the time-dependence is corrected for. Next, the likelihood fits for the calorimeter energy scale are performed separately in the eight longitudinal towers. Applying these corrections to the data eliminates the dependence on electron $|\eta|$ (Fig. S13).

The amount of radiative material is simulated using a fine-grained three-dimensional lookup table, as described in Sec. III. The tail of the E/p distribution ($E/p > 1.12$), which is sensitive to the total number of radiation lengths traversed, is used to tune the latter in the simulation by performing a maximum likelihood fit. We obtain a multiplicative factor $S^W_{\rm mat} = 1.0493 \pm 0.0016_{\rm stat} \pm 0.0012_{\rm QCD}$ ($S^Z_{\rm mat} = 1.0428 \pm 0.0060_{\rm stat}$) to the number of radiation lengths in the simulation, where the QCD systematic uncertainty refers to background contamination due to QCD jets. The results from W and Z data are statistically consistent within 1σ and are combined to give the correction $S^{W,Z}_{\rm mat} = 1.0488 \pm 0.0020$ applied to the simulation. Figure S14 shows the E/p distributions for both $W \to e\nu$ and $Z \to ee$ data after the correction factor is applied. Displayed on each of these distributions in this figure is the quantity $\Delta S_{\rm mat} \equiv S_{\rm mat} - 1$, which averages to zero over the $W \to e\nu$ and $Z \to ee$ samples.

The accurate simulation of electron and photon showers requires knowledge of the amount of CEM material [64]. The relative fraction of electron candidates with low E/p ($0.90 < E/p < 0.93$) to those in the range $0.90 < E/p < 1.09$ is sensitive to longitudinal shower leakage, and hence the CEM thickness in radiation lengths. A maximum likelihood fit to this fraction is used to tune the radiation-length (X_0) thickness of each tower by $\approx 0.1X_0$. The statistical uncertainty derived from this tuning contributes a systematic uncertainty of 0.4 (0.8) MeV on the $W(Z)$-boson mass measurement in the electron channel.

The parameter ζ in Eq. (S1) describing the residual energy dependence of the CEM response (Sec. III) is tuned using the fitted energy scales as a function of electron E_T in $W \to e\nu$ and $Z \to ee$ data. Figure S15 shows the results of these fits after including the value $\zeta = (7.2 \pm 0.4_{\rm stat}) \times 10^{-3}$ in the simulation; the dependence of the energy scale on E_T is removed on average for the $W \to e\nu$ and $Z \to ee$ data. The uncertainty on ζ propagates to a systematic uncertainty of 2.4 (1.5) MeV on the $W(Z)$-boson mass measurement in the electron channel.

Finally, the inclusive fits to the peak region ($0.93 < E/p < 1.17$) of the E/p distribution yield consistent values for the calorimeter-energy scale-factor S_E in $W \to e\nu$ and $Z \to ee$ data, which differ by (215 ± 198) ppm. Their

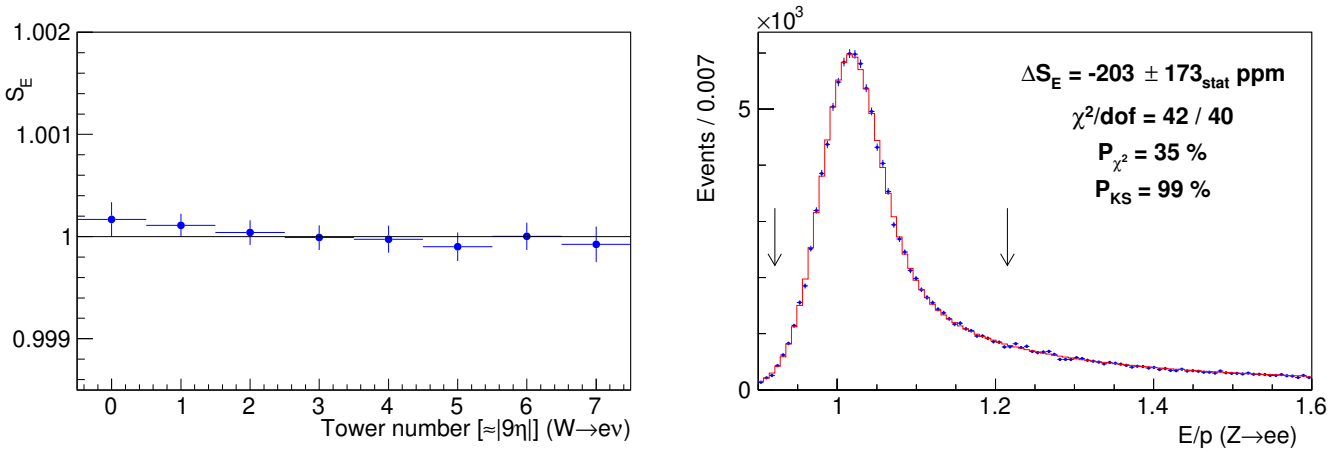

FIG. S13: (Left) Measured calorimeter energy scale in bins of electron tower in $W \to e\nu$ data after corrections are applied, with the line $S_E = 1$ overlaid. The towers are numbered in order of increasing $|\eta|$ and each tower subtends $\Delta\eta \approx 0.11$. (Right) Distribution of E/p for $Z \to ee$ data (circles) after the full energy-scale calibration; the best-fit template (histogram) is overlaid. The fit region is enclosed by arrows.

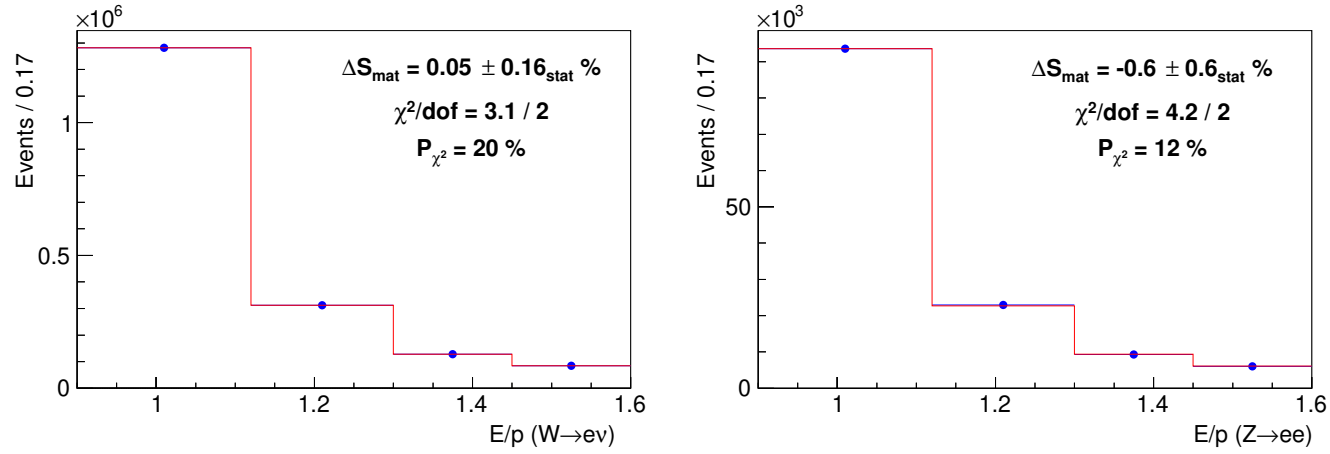

FIG. S14: Distributions of E/p in data (circles) and simulation with the best-fit value of $S_{\rm mat}^{W,Z}$ (histograms) in $W \to e\nu$ (left) and $Z \to ee$ (right) events.

combination has a statistical uncertainty of 42 ppm. After applying the combined S_E in the simulation, the simulated E/p distributions show good agreement with the $W \to e\nu$ (Fig. 2 of the main text) and $Z \to ee$ (Fig. S13) data respectively. Displayed on these figures is the value of $\Delta S_E \equiv S_E - 1$, which averages to zero over the $W \to e\nu$ and $Z \to ee$ samples.

The E/p-based calibration uncertainties are due to $S_{\rm mat}$ (2.7 MeV), the tracker material model (3.0 MeV), calorimeter thickness (0.4 MeV), nonlinearity (2.4 MeV), and resolution (0.9 MeV). Including the statistical uncertainty of 3.4 MeV gives a total E/p-based calibration uncertainty on M_W of 6.1 MeV.

B. $Z \to ee$ mass measurement and calibration

As with the calibration of track momenta using J/ψ and Υ events, the E/p-based calorimeter-energy calibration is validated with a measurement of the Z-boson mass, which is initially blinded as described in Sec. I. Using simulated templates, the maximum likelihood fit in the range 81 000 $< m_{ee} <$ 101 000 MeV (Fig. 3 of the main text) yields

$$M_Z = 91\ 194.3 \pm 13.8_{\rm stat} \pm 7.6_{\rm syst}\ {\rm MeV} \tag{S13}$$

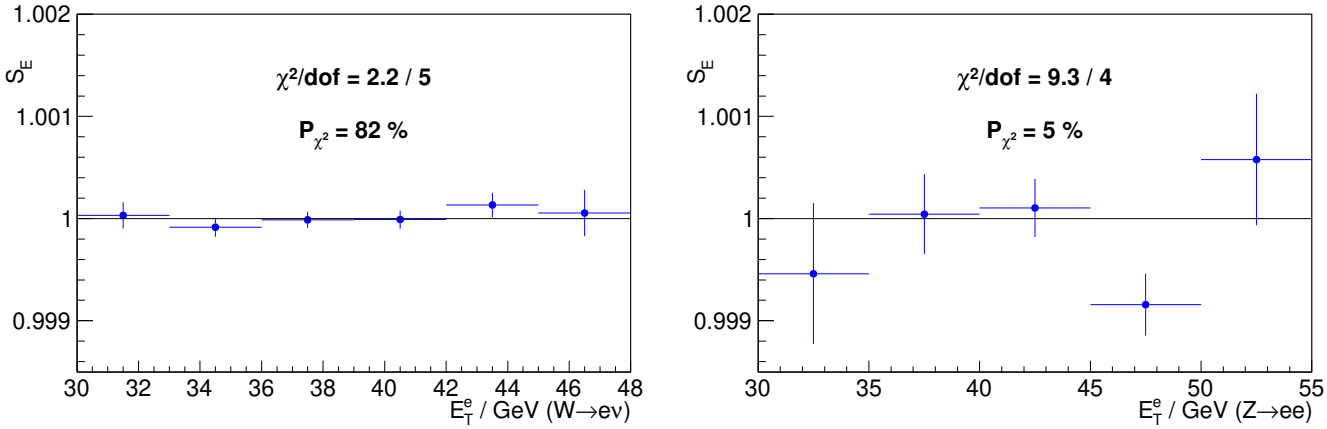

FIG. S15: Measured energy scale as a function of electron E_T for $W \to e\nu$ (left) and $Z \to ee$ (right) data, with the line $S_E = 1$ overlaid. The simulation is corrected with the best-fit value of $\zeta = (7.2 \pm 0.4) \times 10^{-3}$ in Eq. (S1).

TABLE S3: Summary of momentum scale determinations using J/ψ-meson data and Υ-meson data with (BC) and without (NBC) beam-constrained tracks. The systematic uncertainties for the Υ samples are obtained using BC Υ data and assumed to be the same for NBC Υ data, since the sources are completely correlated.

Sample	$\Delta p/p$ (ppm)
$J/\psi \to \mu\mu$	$-1401 \pm 2_{\rm stat} \pm 29_{\rm syst}$
$\Upsilon \to \mu\mu$ (NBC)	$-1371 \pm 13_{\rm stat} \pm 34_{\rm syst}$
$\Upsilon \to \mu\mu$ (BC)	$-1380 \pm 10_{\rm stat} \pm 34_{\rm syst}$

TABLE S4: Summary of M_Z measurements (in MeV) obtained using subsamples of data containing events with nonradiative electrons ($E/p < 1.1$), one radiative electron ($E/p > 1.1$), or two radiative electrons. Calorimeter-based and track-based measurements are shown for each category; uncertainties are statistical only.

Electrons	Calorimeter	Track
$E/p < 1.1$ only	$91\,190.9 \pm 19.7$	$91\,215.2 \pm 22.4$
$E/p > 1.1$ and $E/p < 1.1$	$91\,201.1 \pm 21.5$	$91\,259.9 \pm 39.0$
$E/p > 1.1$ only	$91\,184.5 \pm 46.4$	$91\,167.7 \pm 109.9$

with the E/p-based calibration, consistent with the known value of M_Z at the level of 0.4σ. The systematic uncertainties on M_Z are due to the E/p calibration (6.5 MeV), the COT momentum-scale calibration (2.3 MeV), alignment corrections (0.8 MeV), and the QED radiative corrections (3.1 MeV). Following this validation of the E/p-based calibration, the M_Z measurement is combined with it to obtain the final electron energy calibration for the M_W measurement, with a corresponding uncertainty of 5.8 MeV.

We test the detector simulation by measuring M_Z using electron track momenta in three configurations: neither electron radiative (i.e., both with $E/p < 1.1$), one electron radiative ($E/p > 1.1$), and both electrons radiative. The results of the fits are shown in Table S4 and Fig. S16. Combining the measurements of events with at least one radiative electron gives $M_Z = 91\ 226.3 \pm 19.4_{\rm stat}$ MeV, consistent with the known M_Z. The calorimeter-based measurements in the same categories of radiative and nonradiative electrons also provide consistent results (Table S4 and Fig. S16).

We combine the $Z \to ee$ mass measurement from Eq. (S13) with the E/p-based calibration, which set S_E to unity with an uncertainty of 76 ppm. Taking the correlations due to COT alignment and calibration, the calorimeter nonlinearity parameter ζ and QED radiative corrections into account, we obtain the final calorimeter-energy scale-factor

$$[\Delta S_E]_{E/p+Z} = -14 \pm 72 \text{ ppm} \tag{S14}$$

to be applied to the W-boson data for the M_W measurement. The $Z \to ee$ mass-based calibration carries a weight of 20% in this combination.

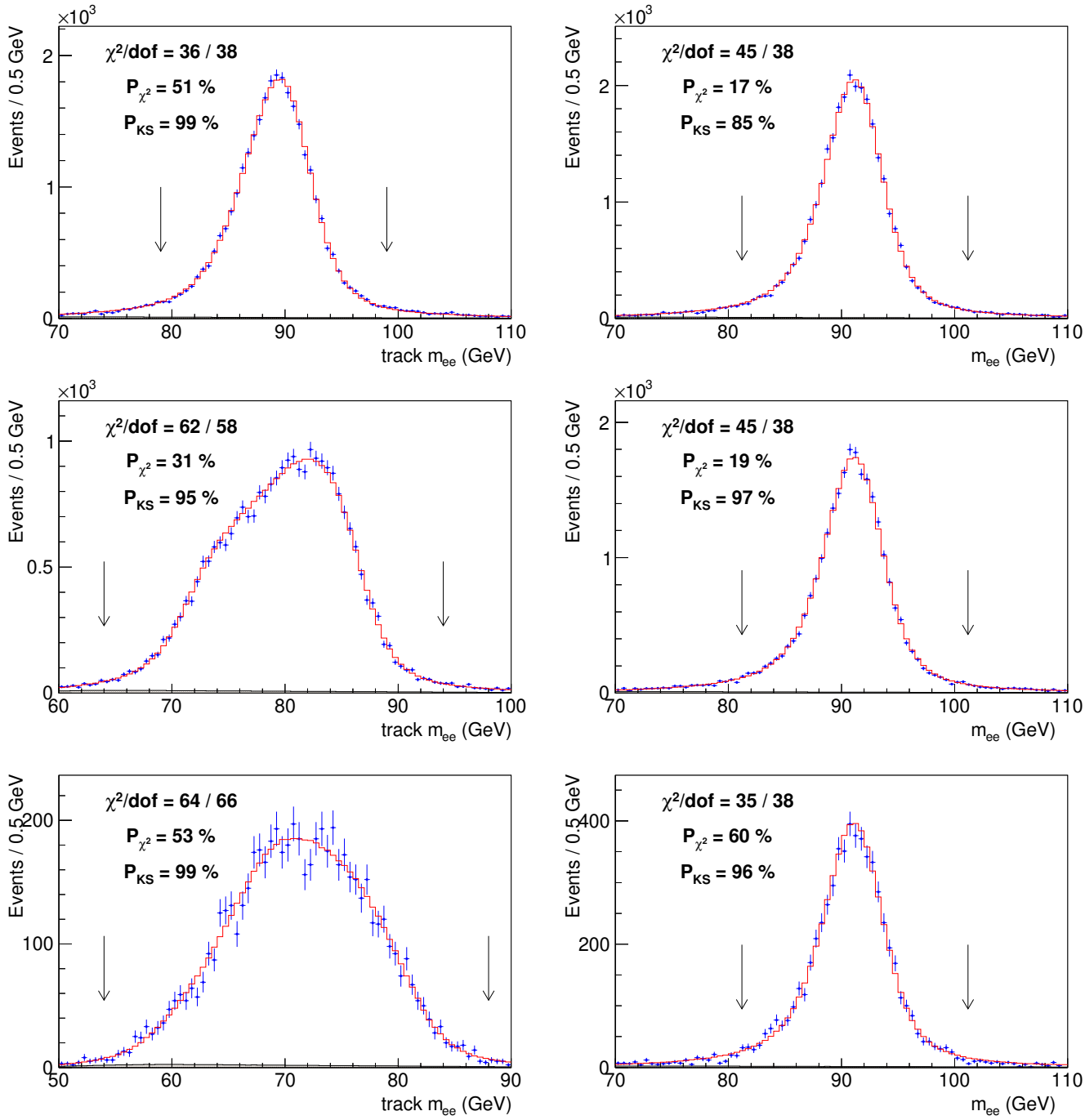

FIG. S16: Distributions (circles) of dielectron mass calculated using (left) only track information and (right) calorimeter E_T with best-fit simulation templates overlaid (histogram) for events with nonradiative electrons (top), one radiative electron (middle), or two radiative electrons (bottom). Fit ranges are enclosed by arrows.

VIII. RECOIL MEASUREMENT

In this section we describe the treatment of the data for the measurement of the hadronic recoil vector, and the parametric model used for its simulation. The model uses parameters and distributions measured in data to describe the production of hadrons and the associated detector response.

Corrections are applied to data to improve the spatial uniformity of the calorimeter response to the hadronic recoil

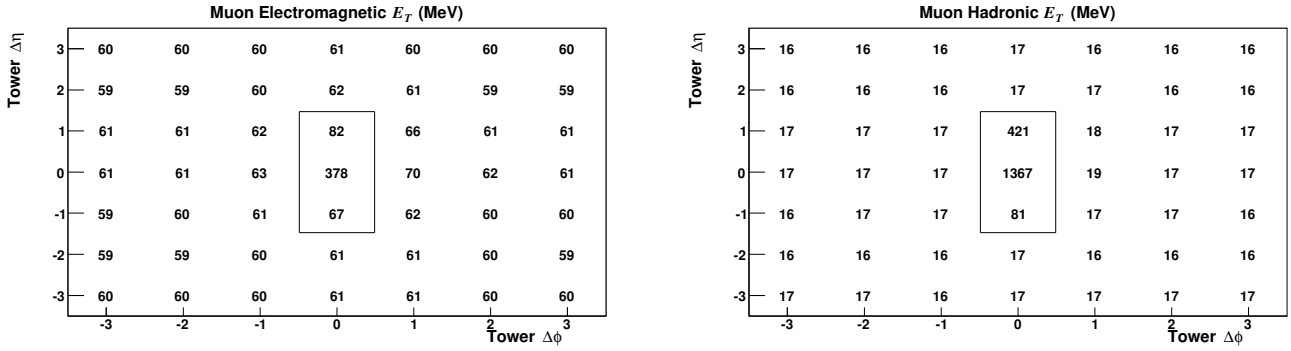

FIG. S17: Average measured energy (in MeV) in the electromagnetic (left) and hadronic (right) calorimeters in the vicinity of the muon in W-boson decays. The differences $\Delta\phi$ and $\Delta\eta$ are signed such that positive differences correspond to towers closest to the muon position at the CEM shower-maximum. The three towers inside the box are removed from the recoil measurement.

energy. The beam axis does not exactly coincide with the calorimeter cylindrical axis, which induces a sinusoidal bias as a function of azimuth in the energy flow detected from hadronic activity. The azimuthal bias increases with $|\eta|$ [39, 43]. This variation is removed by aligning each plug calorimeter in the data before computing $\vec{u}_T$, using minimum-bias data. We apply a relative energy scale between the central and plug calorimeter responses to improve uniformity and resolution [39, 43].

The parametric simulation of the recoil response and resolution is tuned using p_T-balance in $Z \to \ell\ell$ events, since the dilepton transverse momentum is measured with high precision. The recoil reconstruction and simulation is discussed in Refs. [39, 43].

A. Lepton tower removal

The calorimeter towers with lepton energy deposits are excluded from the $\vec{u}_T$ calculation to avoid double-counting the lepton energy. The exclusion of these towers also removes hadronic energy from the recoil calculation. The latter effect is included in the simulation by subtracting from $\vec{u}_T$ the estimated hadronic energy in these towers.

The average energy in the tower traversed by a muon and surrounding towers is shown in Fig. S17. The muon energy deposition is localized to the traversed tower and occasionally the neighboring towers in η, hence the three-tower region shown in Fig. S17 is removed. The energy from electron showers spreads across more towers compared to the minimum-ionizing muon trace. The seven-tower region shown in Fig. S18 fully contains the transverse shower spread, hence this region is removed for electrons. The small energy excesses (above the hadronic energy plateau) visible in nearby towers outside these regions are due to final-state QED radiation, which is modeled by the simulation. Defining the transverse direction of the lepton by the unit vector $\hat{l}$ and of the $\vec{u}_T$ vector by the unit vector $\hat{u}_T$, the components $u_{||} \equiv \vec{u}_T \cdot \hat{l}$, $u_\perp \equiv \vec{u}_T \cdot (\hat{l} \times \hat{u}_T)$ and the magnitude $u_T \equiv |\vec{u}_T|$ (Fig. S3) are defined. In the simulation, the lepton tower removal is modeled by the distribution of the hadronic energy in the three- or seven-tower regions, along with its dependence on $u_{||}$, $|u_\perp|$, and $|\eta|$.

The hadronic energy deposited in these three- and seven-tower regions is estimated in situ from the W boson candidate events. The hadronic energy detected in towers separated by 90° in azimuth from the lepton direction is not biased by QED radiation from the lepton, and also not biased by the event selection criteria as discussed in Refs. [39, 43]. Therefore, energy measurements in the three- and seven-tower regions defined at this azimuth, and at the same pseudorapidity as the lepton, are used to estimate the hadronic energy deposited in the removed towers.

Given the stochastic nature of particle production and the steeply-falling distribution of particle energies, the distribution of energy received in these regions is highly skewed. The positive-energy component of the distribution is modeled by a histogram of its logarithm, which compresses and captures its skewed tail. The probability that no particles impact this region, thereby depositing zero energy, depends on the component of the hadronic recoil vector in this region's direction. Using the measurements in the 90°-rotated regions, the fraction of zero-energy measurements is parametrized as a function of $u_{||}$, as shown in Fig. S19.

In addition to its distribution, the dependences of the mean hadronic energy on $u_{||}$, $|u_\perp|$, and $|\eta|$ are also measured (Fig. S20). These measurements are used to model the lepton removal. The predictions from the simulation are

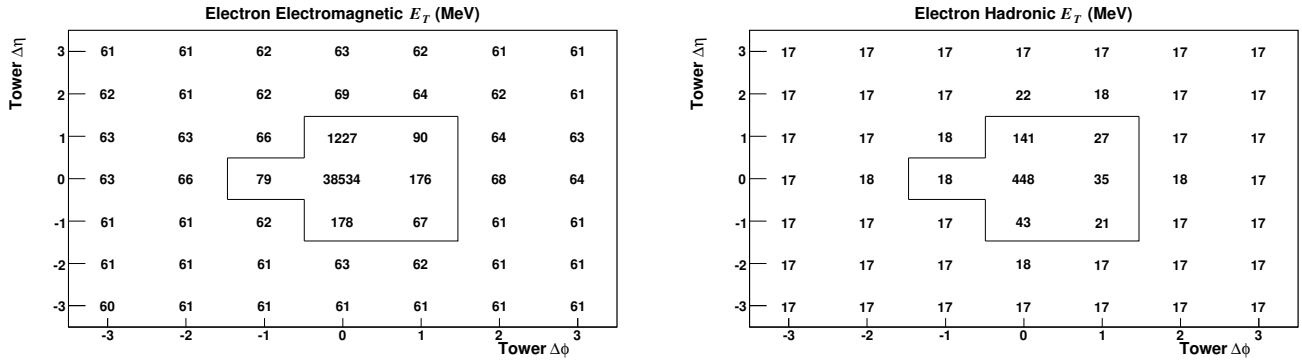

FIG. S18: Average measured energy (in MeV) in the electromagnetic (left) and hadronic (right) calorimeters in the vicinity of the electron shower in W-boson decays. The differences $\Delta\phi$ and $\Delta\eta$ are signed such that positive differences correspond to towers closest to the electron shower position at the CEM. The seven towers inside the box are removed from the recoil measurement.

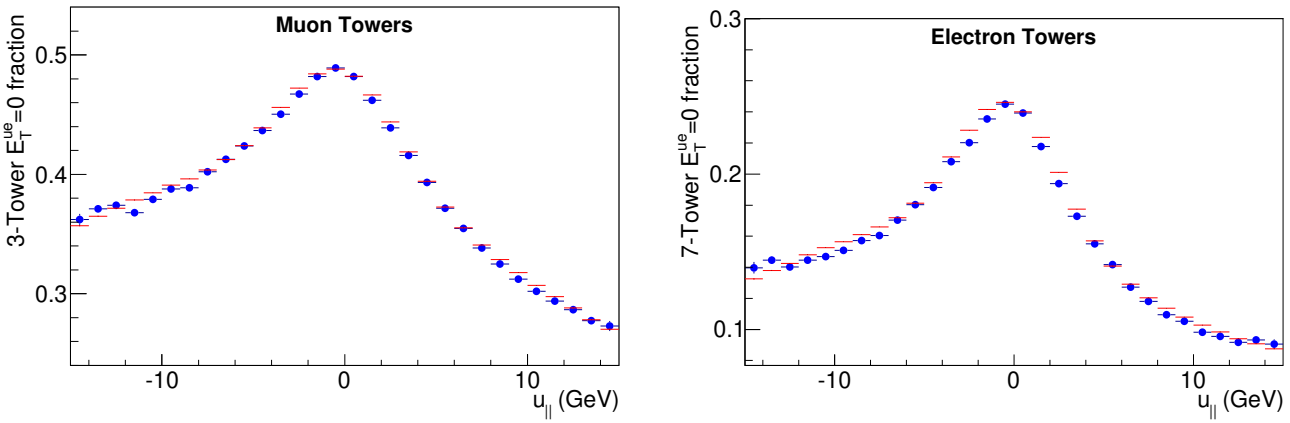

FIG. S19: Fraction of muon-data three-tower (left) and electron-data seven-tower (right) rotated windows containing zero energy, as a function of $u_{||}$. The red lines show the simulation, while the blue circles show the data.

compared to the data in Figs. S19-S20. The small differences between data and simulation visible in Fig. S20 are propagated to the M_W fits and included in the systematic uncertainties. Figure S21 shows the precision of the model for the distribution of the hadronic energy in the removed towers. In order to reduce the dependence of the lepton removal procedure on instantaneous luminosity, the following procedure is introduced in this analysis: a linear model is fit to the dependence of the hadronic tower energy on instantaneous luminosity and the result is applied as a correction in the $\vec{u}_T$ calculation for both data and simulation.

Further validation is provided by comparing the simulation to measurements in towers rotated 180° from the lepton. The consistency between the two choices of rotation angles is 1 MeV (1 MeV) in the muon (electron) channel, which is taken as a systematic uncertainty. Another systematic uncertainty of 1 MeV for the muon channel is due to the choice of parametrizations, and an additional 1 MeV is due to possible muon energy deposition leaking out of the excluded region. The total systematic uncertainty on M_W due to lepton-removal modeling in the muon (electron) channel is 1.7 MeV (1.0 MeV), 0 MeV (0 MeV), and 3.4 MeV (2.0 MeV) for the m_T, p_T^ℓ, p_T^ν fits, respectively.

B. Model parametrization

The recoil simulation parametrizes the response and resolution of the initial-state radiation accompanying the W or Z boson, and models the energy flow from the spectator-parton interactions and additional $p\bar{p}$ collisions in the same collider bunch crossing. Since there are no high-p_T neutrinos in the Z-boson data, the p_T-balance between $p_T(Z \to \ell\ell)$

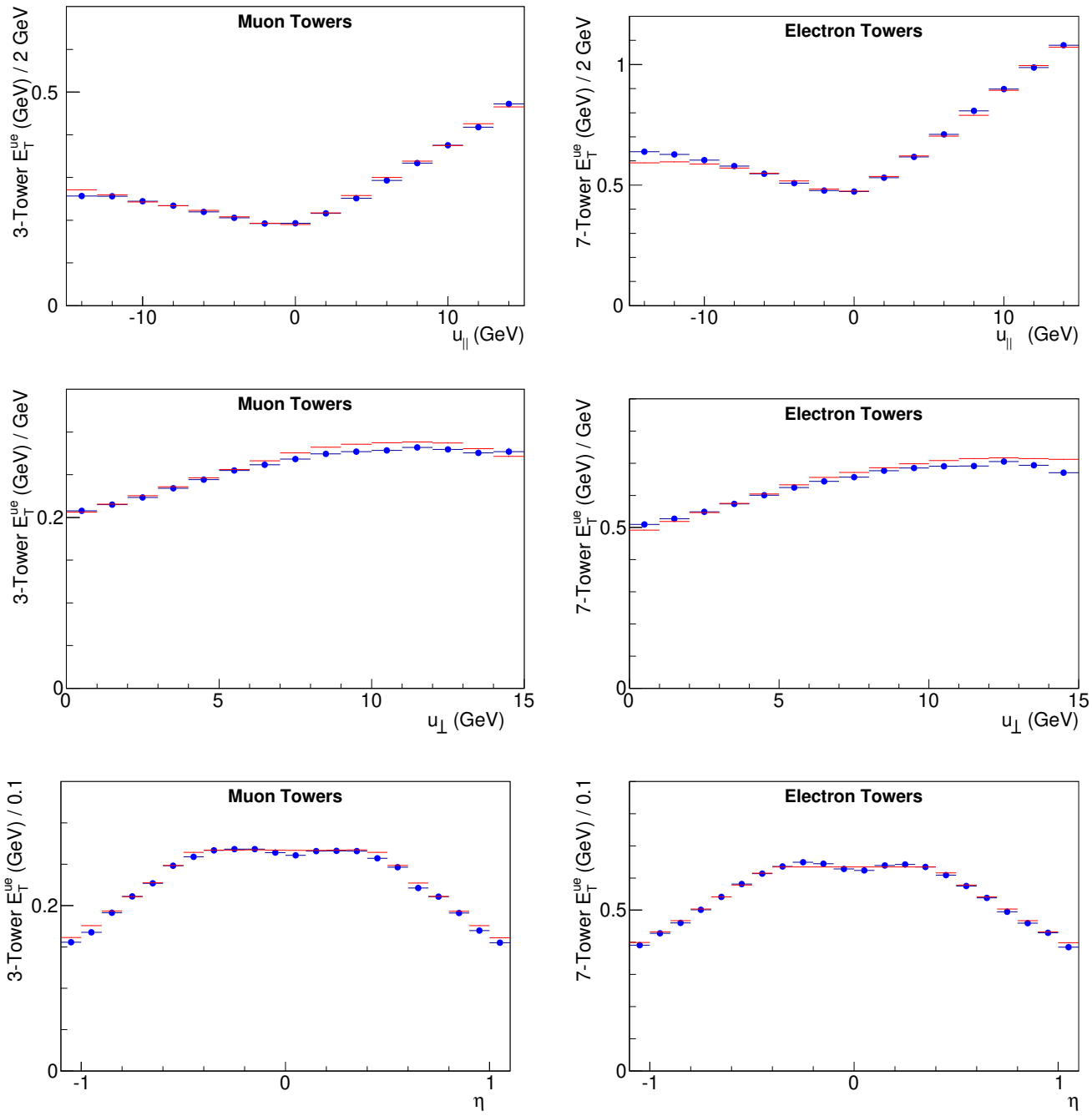

FIG. S20: Variation of hadronic E_T in the three-tower (left) and seven-tower (right) region rotated by 90° in azimuth from the muon (left) or electron (right) as a function of $u_{||}$ (top), $|u_\perp|$ (middle), and η (bottom) for $W \to \mu\nu$ (left) or $W \to e\nu$ (right) data (blue circles) and simulation (red lines).

(which is well measured) and u_T is used to fit for the model parameters. The balance is computed by projecting these transverse vectors on the "η" axis [parallel to $\vec{p}_T(Z \to \ell\ell)$] and the orthogonal "$\xi$" axis in the transverse plane, as shown in Fig. S3 [108].

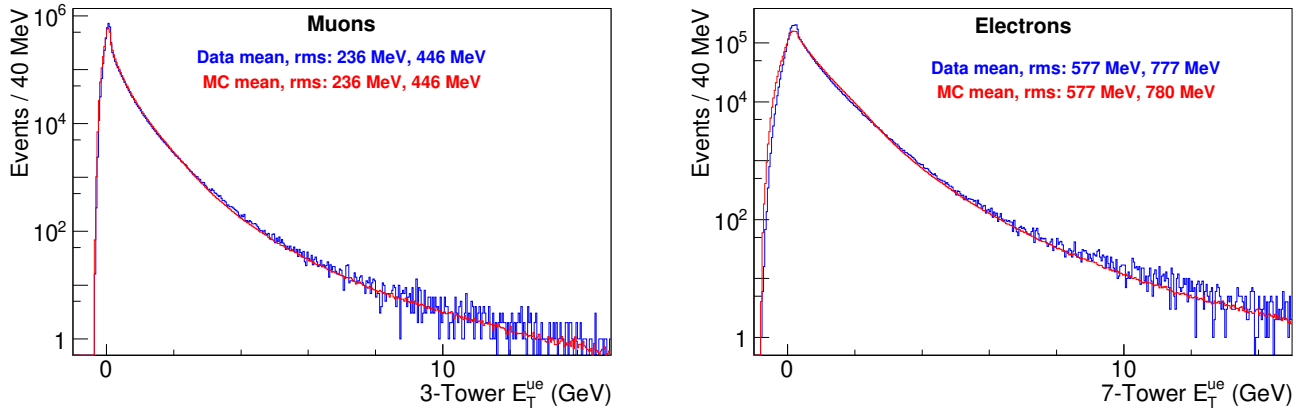

FIG. S21: Distribution of hadronic E_T in the three-tower (left) and seven-tower (right) window separated in azimuth by 90° from the muon or electron, respectively. The red histogram shows the hadronic E_T modeled in the custom simulation, while the blue histogram shows the data. The negative values occur due to the luminosity-dependent correction.

1. *Recoil energy response*

The recoil response function is defined as the ratio of measured recoil to true recoil, projected along the direction of the true recoil $R \equiv \vec{u}_T \cdot \hat{u}_T^{\rm true}/u_T^{\rm true}$, where $\vec{u}_T^{\rm true} = -\vec{p_T}^{W,Z}$ is the net $\vec{p}_T$ of the initial-state radiation. The function

$$R = a \log(b u_T^{\rm true}/{\rm GeV})/\log(15b) \quad , \tag{S15}$$

where a and b are positive constants, is empirically motivated by the approximation $R \approx R_{\rm rec} = -\vec{u}_T \cdot \hat{p}_T^{\ell\ell}/p_T^{\ell\ell}$ derived in Z-boson data (Fig. S22). The parameters a and b describe the average response and its slope with respect to $u_T^{\rm true}$ respectively, defined such that their statistical uncertainties are uncorrelated by including the logarithmic factor in the denominator.

The parameters in Eq. (S15) are determined using the balance $Rp_\eta^{\ell\ell} + u_\eta$ between the recoil and dilepton momentum projections on the η-axis. Figure S23 shows $Rp_\eta^{\ell\ell} + u_\eta$ for the best fit values of a and b,

$$a = (65.00 \pm 0.09_{\rm stat})\% \quad , \quad b = 6.7 \pm 0.6_{\rm stat} \ . \tag{S16}$$

2. *Recoil energy resolution*

The resolution on the magnitude of the simulated recoil is parametrized with a sampling term, simulated with a Laplacian random variable with rms

$$\sigma(u_T) = s_{\rm had}\sqrt{u_T^{\rm true}/\ {\rm GeV}} \quad , \tag{S17}$$

where $s_{\rm had}$ is the sampling term of the calorimeter resolution function. The rms of the p_η-balance $Rp_\eta^{\ell\ell} + u_\eta$ is used to fit for $s_{\rm had}$ in $Z \to \ell\ell$ data (Fig. S24), giving

$$s_{\rm had} = (87.15 \pm 0.68_{\rm stat})\ \% \ . \tag{S18}$$

Events in which the hadronic recoil is dominated by leading neutral pions have significantly better resolution (as the measurement is dominated by the EM energy deposit in the CEM) than events with hadronic recoil containing multiple low-momentum tracks. These variations in fragmentation add kurtosis to the resolution. We parametrize this effect by setting the recoil resolution to 10% of the average value for a fraction f_{π^0} of events. For the remaining $(1 - f_{\pi^0})$ fraction of events, the resolution is scaled up appropriately such that the average recoil resolution is given by Eq. (S17). We find that f_{π^0} is well-parametrized by an exponentially-falling distribution of $u_T^{\rm true}$, which is consistent

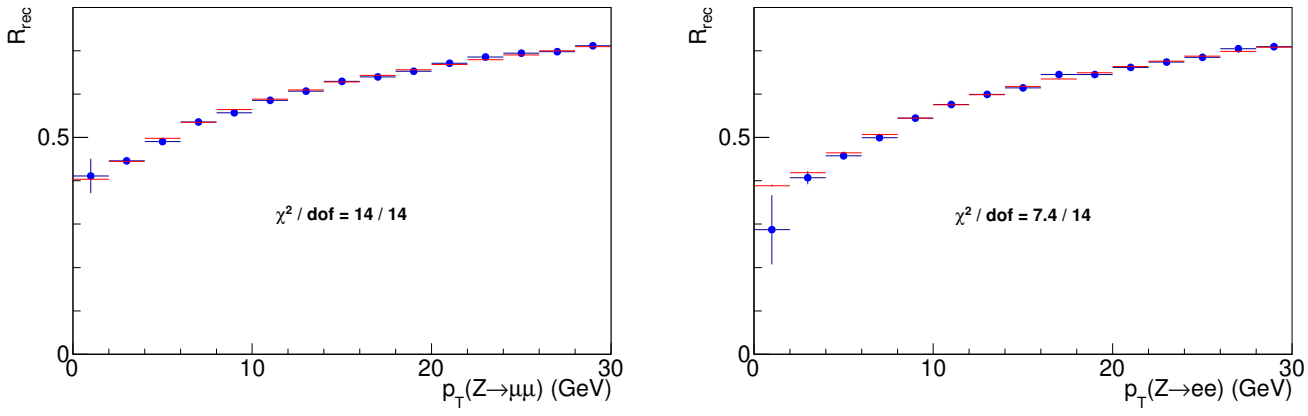

FIG. S22: Mean value of $R_{\rm rec} \equiv -\vec{u}_T \cdot \hat{p}_T^{\ell\ell}/p_T^{\ell\ell}$, which approximates the recoil response R, as a function of dimuon p_T (left) and dielectron p_T (right). The distributions motivate the logarithmic parametrization of the response in Eq. (S15). The simulation (red lines) models the data (blue circles) accurately.

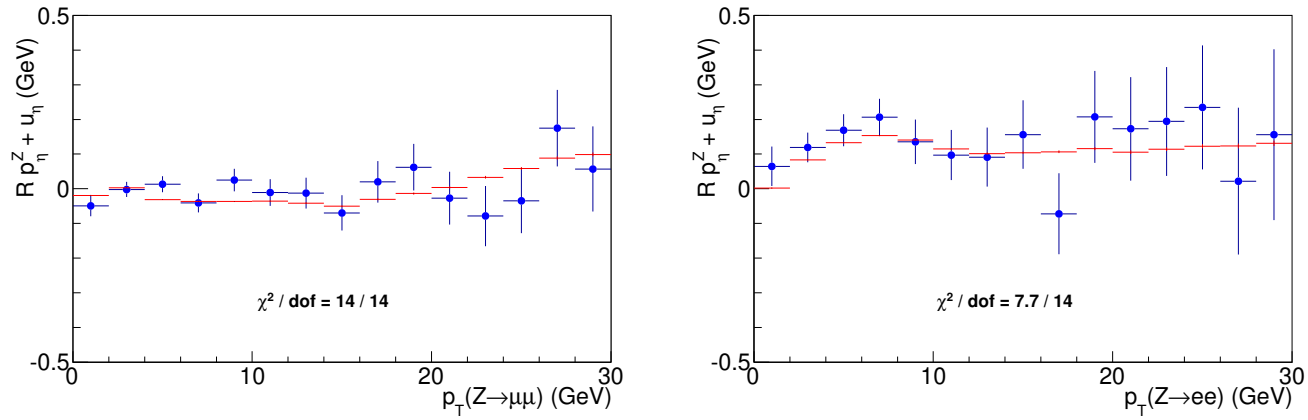

FIG. S23: Distribution of $Rp_\eta^{\ell\ell} + u_\eta$ for Z-boson decays to muons (left) and electrons (right) as a function of Z-boson p_T in simulated (lines) and experimental (circles) data. The detector response parameters a and b (Eq. S15) are obtained by minimizing the combined χ^2 of these distributions.

with the notion that event-to-event variations are prominent for very soft recoil, and are damped as the particle multiplicity in the recoil increases.

The exponential distribution of f_{π^0} is parametrized by its values at $u_T^{\rm true} = 4$ GeV and $u_T^{\rm true} = 15$ GeV, providing uncorrelated parameters. We fit the one-dimensional distributions of the p_η-balance separately for subsamples restricted to $p_T^{\ell\ell} < 8$ GeV and $8 < p_T^{\ell\ell} < 30$ GeV for these parameters, obtaining the values

$$f_{\pi^0}^4 = (89.1 \pm 1.3_{\rm stat})\% \quad , \quad f_{\pi^0}^{15} = (6.43 \pm 0.35_{\rm stat})\% \quad . \tag{S19}$$

The fits to the p_η-balance distributions are shown in Fig. S25. Other functional forms for f_{π^0} yield similar results for observable distributions with no difference in fit quality. The procedure of tuning the kurtosis of the recoil energy resolution on the distributions of p_η-balance is a new feature that incorporates additional information from the data compared to Ref. [43].

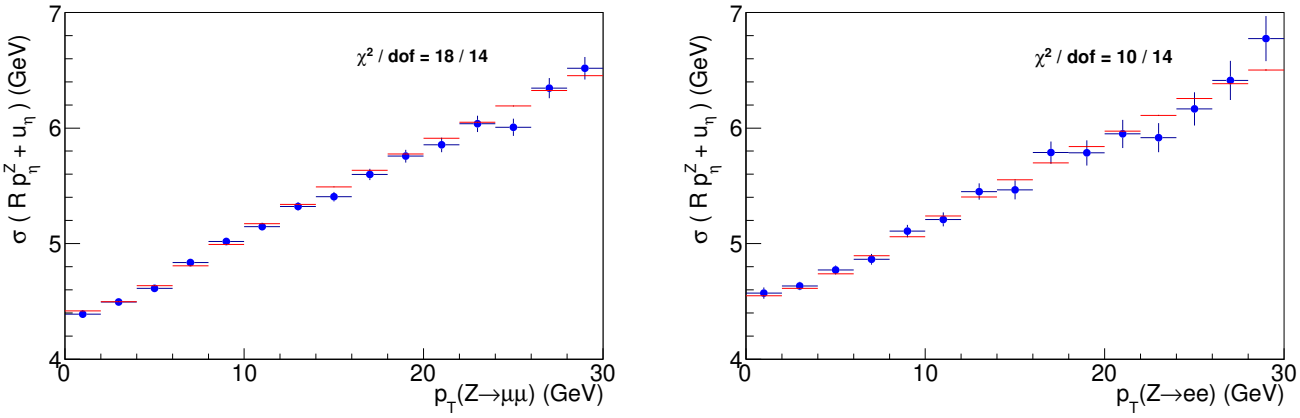

FIG. S24: Resolution on $Rp_\eta^{\ell\ell} + u_\eta$ in simulated (lines) and experimental (circles) data for Z-boson decays to muons (left) and electrons (right).

3. *Recoil angular resolution*

The jet angular resolution depends on the recoil transverse energy, with the jet(s) becoming more collimated at higher $u_T^{\rm true}$ resulting in better angular resolution. This trend is illustrated in Fig. S26, which shows distributions of $|\phi_u - \phi_{\ell\ell} - \pi|$ in four $p_T^{\ell\ell}$ ranges. The resolution of $\phi_{\ell\ell}$ (determined by tracks) is substantially better than the resolution of ϕ_u, so Fig. S26 demonstrates the variation of the ϕ_u resolution.

We parametrize the jet angular smearing $\sigma(\phi_u)$ by a continuous, piece-wise linear function in the ranges $0 < u_T^{\rm true} < 15$ GeV and $15 < u_T^{\rm true} < 30$ GeV. For $u_T^{\rm true} > 30$ GeV we assume a constant $\sigma(\phi_u)$ where the dependence on $u_T^{\rm true}$ does not matter, since we eventually require $u_T < 15$ GeV for the mass-measurement sample. The parameters of this function are its values at $u_T^{\rm true} = 9.4$ GeV, 15 GeV, and 24.5 GeV, respectively, such that the statistical uncertainties on the parameters are uncorrelated. The parameters α, β, and γ of the piece-wise linear function

$$\begin{aligned}
\sigma(\phi_u) - \alpha &\propto 9.4 - u_T^{\rm true}/\text{GeV} && u_T^{\rm true} < 15 \text{ GeV} \quad , \\
\sigma(\phi_u) &= \beta && u_T^{\rm true} = 15 \text{ GeV} \quad , \\
\sigma(\phi_u) - \gamma &\propto 24.5 - u_T^{\rm true}/\text{GeV} && 15 < u_T^{\rm true} < 30 \text{ GeV} \quad , \\
\sigma(\phi_u) &= \text{constant} && u_T^{\rm true} > 30 \text{ GeV}
\end{aligned} \tag{S20}$$

are tuned on the distributions of $|\phi_u - \phi_{\ell\ell} - \pi|$ in the four $p_T^{\ell\ell}$ ranges, shown in Fig. S26. The resulting values are

$$\begin{aligned}
\alpha &= 272.7 \pm 4.1_{\rm stat} \text{ mrad} \quad , \\
\beta &= 185.0 \pm 3.1_{\rm stat} \text{ mrad} \quad , \\
\gamma &= 143.0 \pm 2.4_{\rm stat} \text{ mrad} \, .
\end{aligned} \tag{S21}$$

The unspecified coefficients in Eq. (S20) are fixed by continuity. The procedure of tuning the recoil angular smearing model on the distributions of $|\phi_u - \phi_{\ell\ell} - \pi|$ is a new feature that incorporates additional information from the data compared to Ref. [43].

4. *Dijet resolution*

A small fraction of the W and Z boson events contain multijets recoiling against the boson. In the regime of low boson p_T selected for this analysis, most of the multijet events contain two soft jets. These dijet events contribute a resolution component perpendicular to the direction of the boson p_T. We parametrize the fraction f_2 of dijet events as a linear function of boson p_T, with the parameters f_2^a specifying the average dijet fraction and f_2^s specifying the variation in the fraction with $u_T^{\rm true}$. These resolution parameters are tuned on the rms of the p_ξ-balance as a function of $p_T^{\ell\ell}$, as shown in Fig. S27. The resulting parameter values are

$$f_2^a = (0.80 \pm 0.04_{\rm stat})\% \quad , \quad f_2^s = (44 \pm 6_{\rm stat})\% \quad . \tag{S22}$$

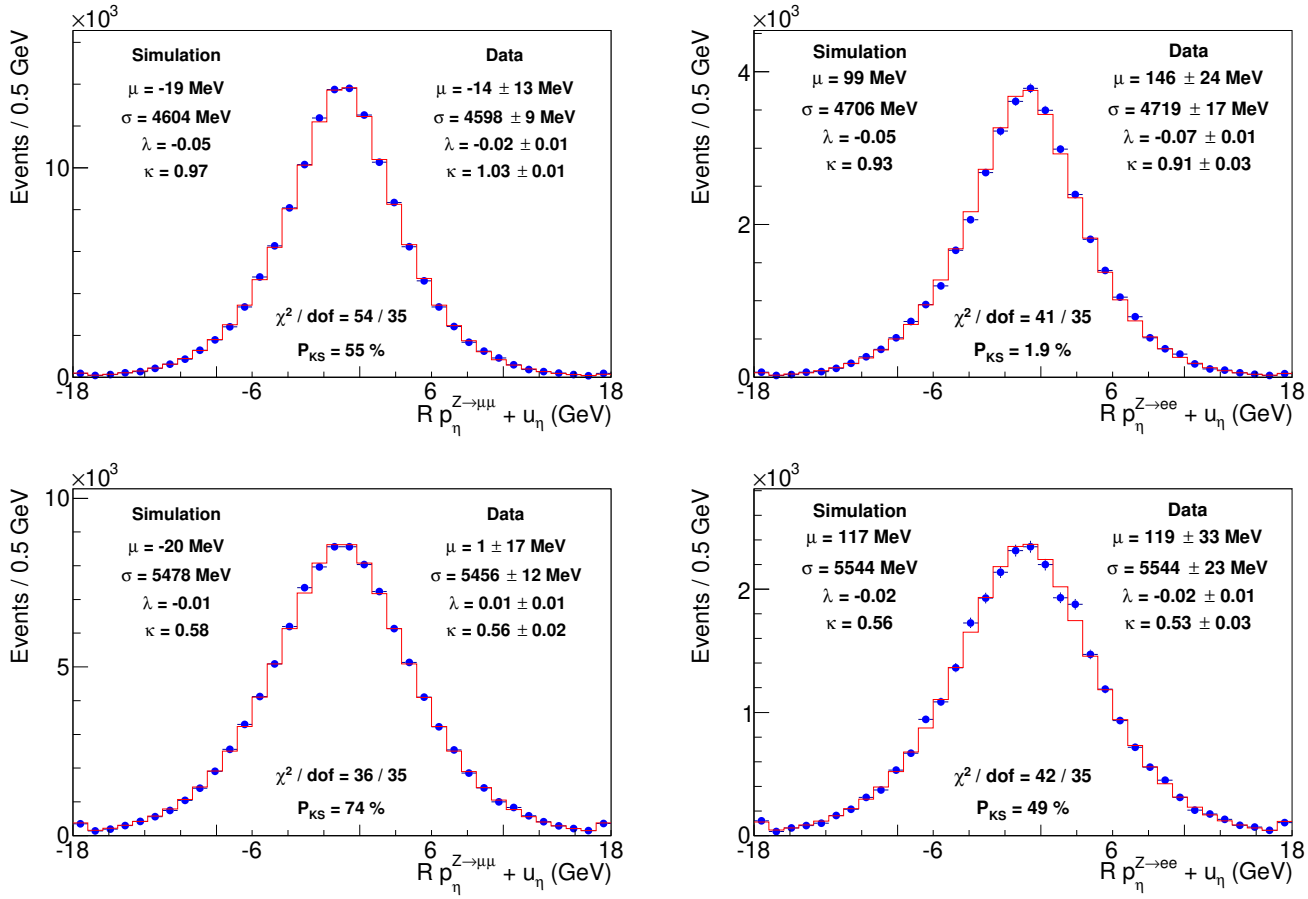

FIG. S25: Distributions of the p_η-balance for $p_T^{\ell\ell} < 8$ GeV (top) and $8 < p_T^{\ell\ell} < 30$ GeV (bottom), for the muon (left) and electron (right) channels. The first four moments [mean (μ), rms (σ), skewness (λ), and excess kurtosis (κ)] are shown.

The recoil resolution function due to the dijet component is modeled with a Gaussian distribution with mean k_ξ and rms$= k_\xi\delta_\xi$, symmetrized in the ξ-direction. The parameters k_ξ and δ_ξ are tuned on the one-dimensional distributions of the p_ξ-balance in the sub-samples $p_T^{\ell\ell} < 8$ GeV and $8 < p_T^{\ell\ell} < 30$ GeV (see Fig. S28). The fitted parameter values are

$$k_\xi = (10.0 \pm 0.2_{\rm stat})\ {\rm GeV} \quad , \quad \delta_\xi = (27.5 \pm 3.0_{\rm stat})\% \quad . \tag{S23}$$

This dijet resolution model provides an accurate description of the upper part of the p_ξ-balance spectrum, but a residual mismodeling in the lower part of this spectrum when $p_T^{\ell\ell} < 8$ GeV affects $\approx 0.2\%$ of events. We apply a correction to migrate this small fraction of events with $u_T^{\rm true} \approx 4$ GeV and $|u_\xi| \approx 2.9$ GeV, to a slightly larger or smaller value of u_ξ. We construct a two-dimensional probability distribution $P(u_T^{\rm true}, |u_\xi|) = A_\xi \mathcal{G}_{u_T^{\rm true}}(4.0, 2.0)\mathcal{G}_{|u_\xi|}(\mu_\xi, \epsilon_\xi)/2.0$ where $\mathcal{G}_{u_T^{\rm true}}$ is a Gaussian probability distribution that has support over a narrow range of $u_T^{\rm true}$ at low $u_T^{\rm true}$, and $\mathcal{G}_{|u_\xi|}$ is also a Gaussian probability distribution function with support near $|u_\xi| = \mu_\xi \pm \epsilon_\xi$. For a fraction $P(u_T^{\rm true}, |u_\xi|)$ of events, we multiply the *a-priori* simulated value of u_ξ by $S_\xi^+ = 2.1 \pm 0.07$. Otherwise, for a fraction $P(u_T^{\rm true}, |u_\xi|)/q_\xi$ of the events, we divide the *a-priori* simulated value of u_ξ by $S_\xi^- = 3.4 \pm 0.1$, where $q_\xi = 2.51 \pm 0.21$. The tuned values of the parameters, including $\mu_\xi = (2.90 \pm 0.06)$ GeV, $\epsilon_\xi = (1.037 \pm 0.035)$ GeV and $A_\xi = (7.50 \pm 1.25)\%$, are obtained by fitting the distributions of the p_ξ-balance. Following this additional tuning, the distributions of the p_ξ-balance are well-modeled by the simulation, as shown in Fig. S28. This correction also improves the agreement between simulation and data for the W- and Z-boson recoil distributions (Figs. S31 and S32), which serve as consistency checks.

The use of the p_η-balance and p_ξ-balance distributions (Figs. S25 and S28 respectively) to constrain the higher-order

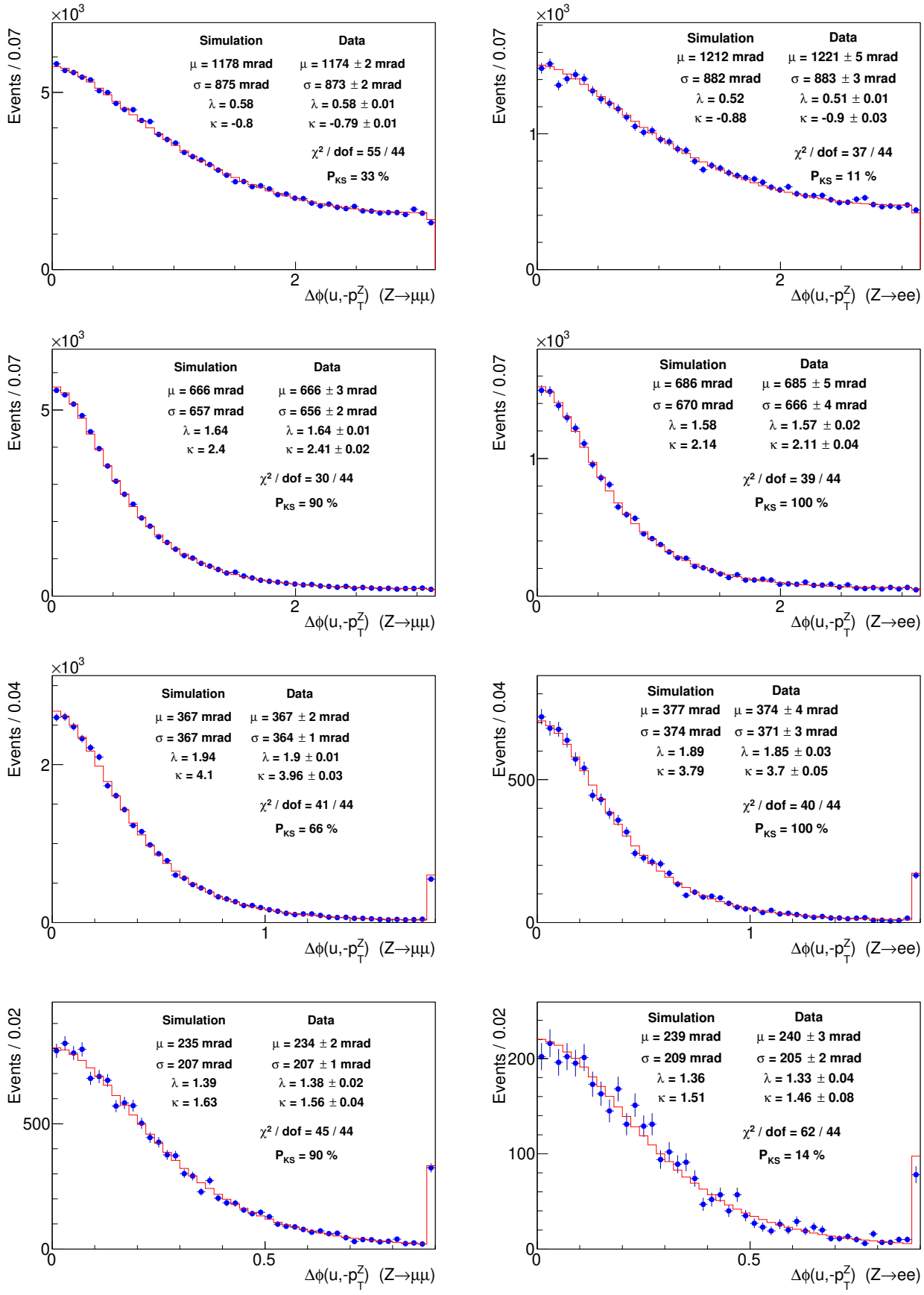

FIG. S26: Distributions of the difference in azimuthal angles of $\vec{u}$ and $-\vec{p}_T^{\,\ell\ell}$, shown in absolute value in the following $p_T^{\ell\ell}$ ranges: (top) $p_T^{\ell\ell} < 8$ GeV, (2nd row) $8 < p_T^{\ell\ell} < 15$ GeV, (3rd row) $15 < p_T^{\ell\ell} < 23$ GeV and (bottom) $23 < p_T^{\ell\ell} < 30$ GeV. The distributions from $Z \to \mu\mu$ events are shown on the left and those from $Z \to ee$ events are shown on the right. The data (blue circles) are compared to the tuned simulation (red histogram).

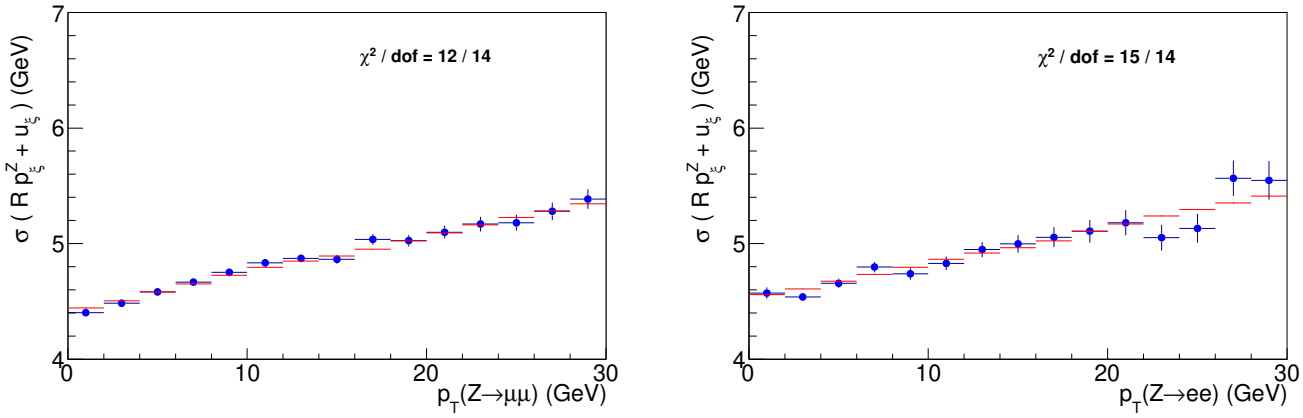

FIG. S27: Root-mean-square dispersion of the scaled p_T-balance in $Z \to \ell\ell$ data, projected onto the ξ axis, as a function of $p_T^{\ell\ell}$. The data (blue circles) for the muon (left) and electron (right) channels are compared to the tuned simulation (red histogram). These plots are used to tune the dijet resolution parameters f_2^a and f_2^s, whose values are given in Eq. (S22).

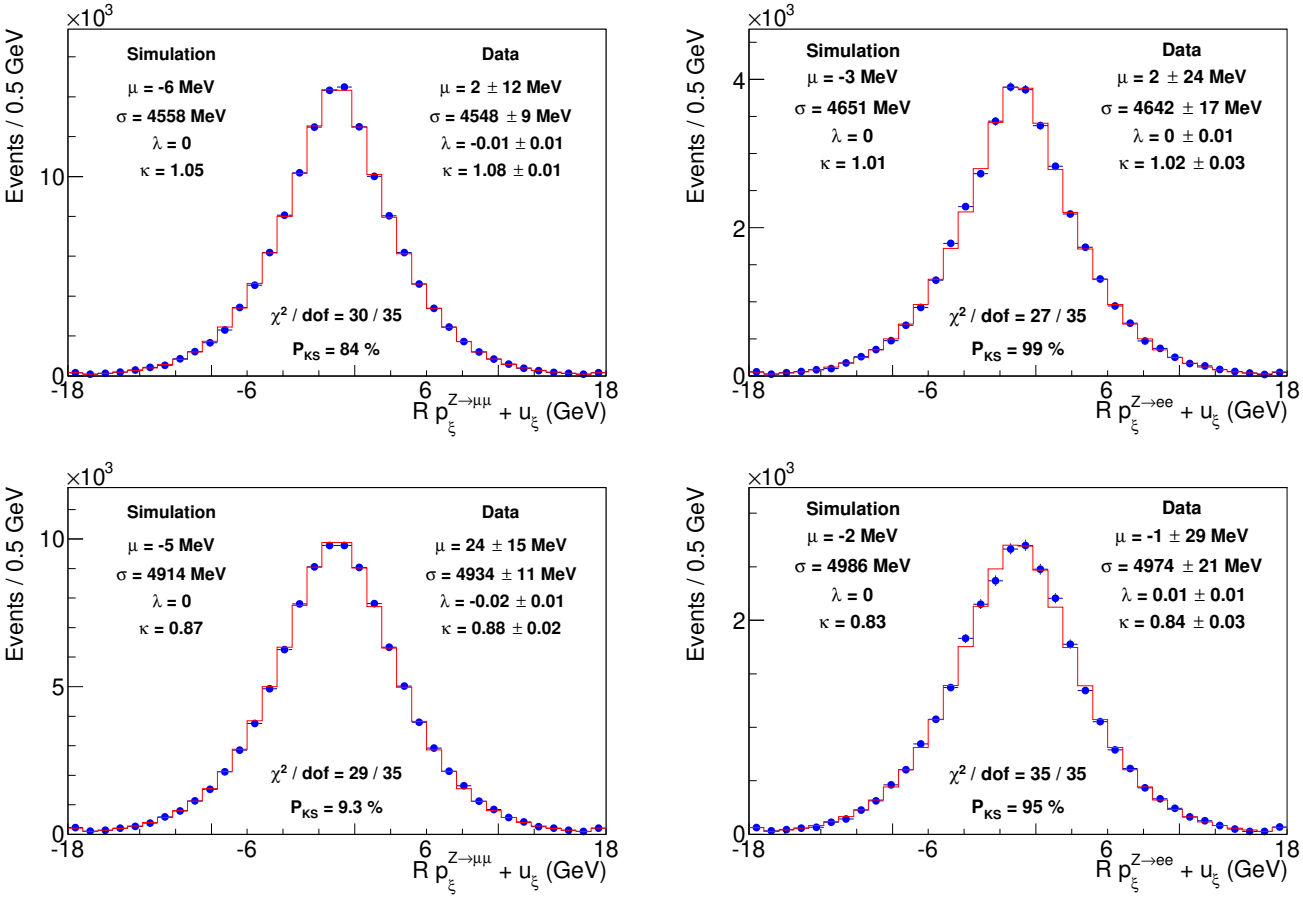

FIG. S28: Distributions of the p_ξ-balance for $p_T^{\ell\ell} < 8$ GeV (top) and $8 < p_T^{\ell\ell} < 30$ GeV (bottom), for the muon (left) and electron (right) channels. The first four moments, mean (μ), rms (σ), skewness (λ), and excess kurtosis (κ) are shown. The data (blue circles) are compared to the tuned simulation (red histogram). These plots are used to tune the dijet resolution parameters k_ξ and δ_ξ, whose values are given in Eq. (S23), as well as A_ξ, μ_ξ, ϵ_ξ, $S_\xi^\pm$ and q_ξ, which are described in the text.

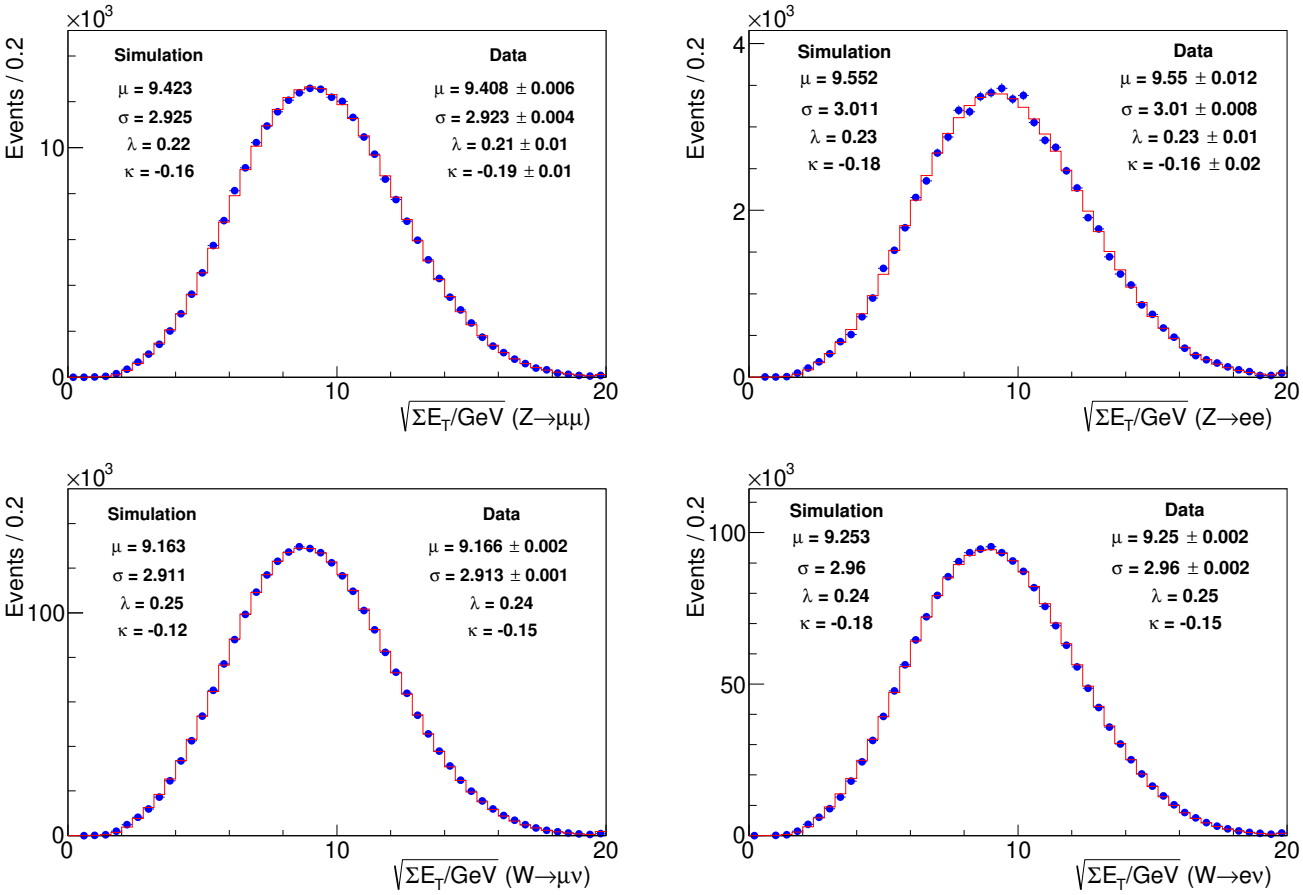

FIG. S29: Distributions of $\sqrt{\Sigma E_T}$ for the muon (left) and electron (right) channels, comparing data (blue points) and simulation (red histogram) for Z (top) and W (bottom) boson candidate events.

cumulants (beyond the rms) of the recoil fluctuations is a new feature of this analysis that incorporates additional information from the data, as compared to Ref. [43].

5. *Spectator and additional $p\bar{p}$ interactions*

In addition to the partons that annihilate to produce the W or Z boson, the colliding proton and antiproton contain other "spectator" partons that experience strong interactions with each other. The fluctuations in the energy flow from these spectator-parton interactions and additional $p\bar{p}$ collisions contribute to the recoil resolution [39, 43]. These fluctuations depend on ΣE_T, the scalar sum of transverse energies in the calorimeter towers. For simulating multiple interactions we use $\sqrt{\Sigma E_T}$ because the hadronic resolution from the multiple interactions is proportional to this quantity, as shown below. We produce a two-dimensional histogram of $\sqrt{\Sigma E_T}$ as a function of instantaneous luminosity, as measured in the zero-bias data. In order to model the distribution of $\sqrt{\Sigma E_T}$ in simulated W and Z boson events, we randomly sample the distribution of instantaneous luminosity from the Z boson data, and then randomly sample the distribution of $\sqrt{\Sigma E_T}$ corresponding to the given value of instantaneous luminosity in this two-dimensional histogram. This technique ensures that the resulting simulated distribution of $\sqrt{\Sigma E_T}$ corresponds to the instantaneous luminosity profile of the W and Z boson data, and is an improvement over the technique used in Ref. [43]. The luminosity profiles for the electron and muon channels are sampled separately since the data sets are derived from independently triggered streams. The distributions of $\sqrt{\Sigma E_T}$ for data and simulation are shown in Fig. S29.

The ΣE_T distribution for spectator interactions is obtained from minimum-bias collision data as described in Ref. [39]. A ΣE_T value sampled from this distribution is multiplied by a parameter N_V to allow for a difference in

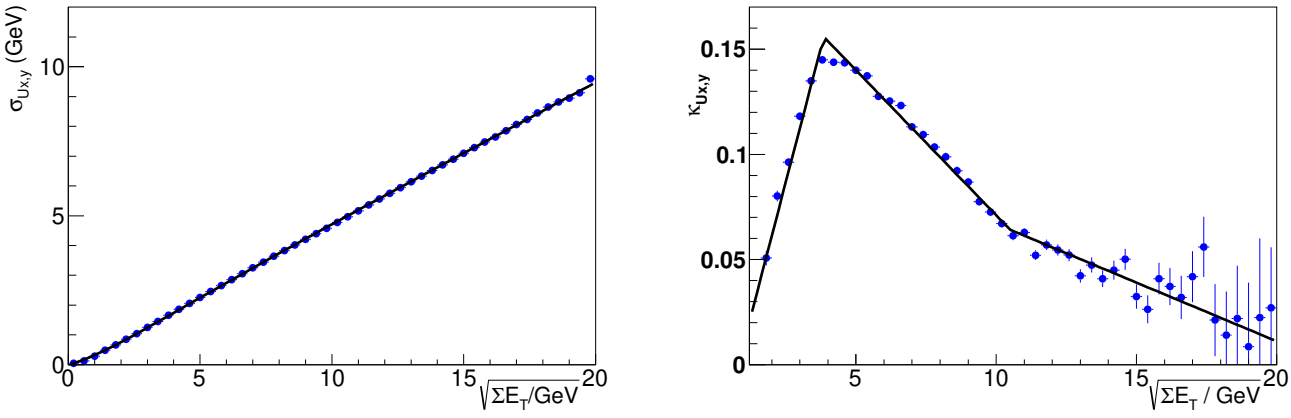

FIG. S30: (left) rms of u_x and u_y in minimum-bias data, shown as a function of the scalar $\sqrt{\Sigma E_T}$. The black curve is the function given by Eq. (S26). (right) Excess kurtosis κ of the distribution of $(u_i - \langle u_i \rangle)/\sigma_i$ $(i = x, y)$ in minimum-bias data, shown as a function of the scalar $\sqrt{\Sigma E_T}$. The black curve is a piece-wise linear fit used in the custom detector simulation.

the spectator interactions accompanying W and Z boson production. For each simulated event, the total ΣE_T is evaluated by adding the two contributions from multiple interactions and spectator interactions.

A simultaneous least-squares fit for N_V and $s_{\rm had}$ (implemented such that their statistical uncertainties are uncorrelated) is performed using the rms resolution on the p_η-balance ($Rp_\eta^{\ell\ell} + u_\eta$) as a function of $p_T^{\ell\ell}$ (see Fig. S24). The result of the fit is

$$N_V = 1.1300 \pm 0.0064_{\rm stat}. \tag{S24}$$

The resolution due to multiple and spectator interactions is simulated for each event by adding to the reconstructed recoil a vector (u_x, u_y) whose independent components are calculated using the total ΣE_T [50]. The mean values $\langle u_{x,y} \rangle$ are given by

$$\langle u_{x,y} \rangle = A_{x,y} + B_{x,y}(\Sigma E_T/\ {\rm GeV}) + \mathcal{G}_{x,y}\ , \tag{S25}$$

where the parameters $(A_x, A_y) = (-111, 10)$ MeV and $(B_x, B_y) = (0.88, -0.59)$ MeV are obtained from a linear fit to the mean $\langle u_{x,y} \rangle$ in minimum-bias data, and $\mathcal{G}_{x,y}$ is a resolution function described below. The parameters A and B capture recoil contributions due to instrumental noise and the calorimeter being off-axis with respect to the beam.

The underlying event resolution is modeled with two independent Gaussian random variables $\mathcal{G}_{x,y}$, each with rms given by

$$\sigma_i = 0.473\sqrt{\Sigma E_T/{\rm GeV}}(1.0 - 0.5e^{-\sqrt{\Sigma E_T/{\rm GeV}}/2.18})\ {\rm GeV}\ \ (i = x, y), \tag{S26}$$

as derived from minimum-bias data (see Fig. S30). The rms of $u_{x,y}$ in minimum-bias data increases linearly with $\sqrt{\Sigma E_T}$ as expected, though with an exponential suppression at low $\sqrt{\Sigma E_T}$.

As a refinement to the previous analysis [43], which only considered the first two moments of the fluctuations of energy flow from multiple interactions, we also examine the skewness and excess kurtosis of the $(u_i - \langle u_i \rangle)/\sigma_i$ distributions as functions of $\sqrt{\Sigma E_T}$. These distributions are described by double-Gaussian functions with zero mean and skewness, overall rms of unity, and a fixed ratio of normalizations of the two Gaussians. The excess kurtosis is determined by the ratio of the spreads of the two Gaussians and is shown as a function of $\sqrt{\Sigma E_T}$ in Fig. S30. To better model the resolution function arising from multiple interactions, we include these measurements of excess kurtosis to calculate the rms of each Gaussian in the custom detector simulation.

6. *Constraint from p_T^W data spectrum*

As mentioned in Sec. IV B, the theoretical p_T^W/p_T^Z spectrum ratio is constrained by the p_T^W spectrum in data in order to reduce the theoretical uncertainty in the p_T^W/p_T^Z ratio. The results of the profiled tuning of the calorimeter

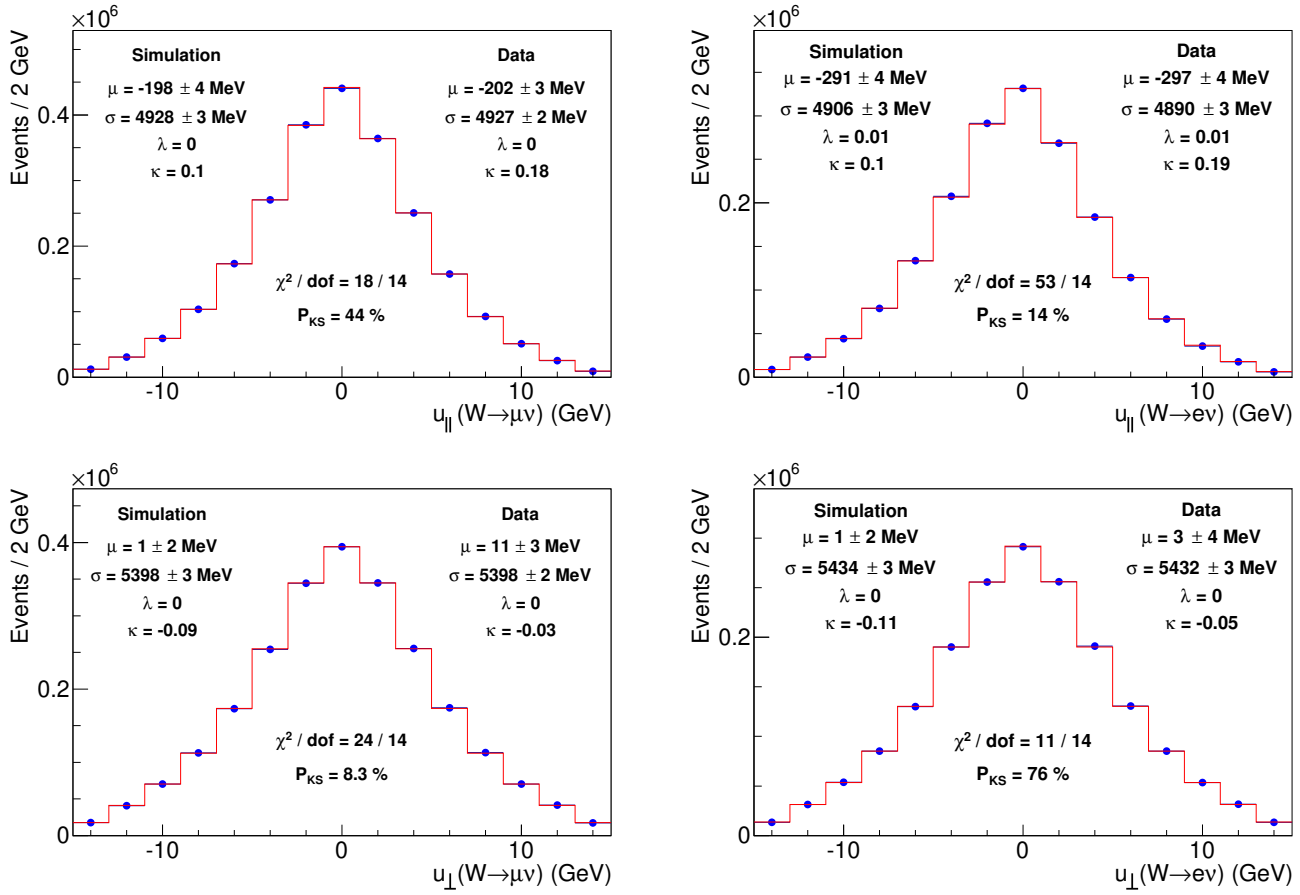

FIG. S31: Distributions of $u_{||}$ (top) and $u_{\perp}$ (bottom) from simulation (histogram) and data (circles) for W boson decays to $\mu\nu$ (left) and $e\nu$ (right) final states. The simulation uses parameters fit from W and Z boson data, and the uncertainty on the simulation is due to the statistical uncertainty on these parameters. The data mean (μ), rms spread (σ), skewness (λ), and excess kurtosis (κ) are well modeled by the simulation. The χ^2 values and the Kolmogorov-Smirnov (KS) probabilities are based only upon the statistical uncertainties in the data and do not take into account the systematic uncertainties in the simulation.

parameters with the Z boson data, including the constraint from the p_T^W spectrum from data, are shown in Table S5. For the m_T and p_T^ν fits, the p_T^W spectrum constraint from data reduces the uncertainties due to the calorimeter response and resolution parameters. For the p_T^ℓ fit these uncertainties are increased, but there is a more than compensating reduction in the theoretical uncertainty due to the p_T^W/p_T^Z spectrum ratio, to which the p_T^ℓ fit is sensitive. The constraint from the p_T^W data spectrum is another new feature that incorporates additional information compared to Ref. [43].

C. Model tests

We compare the simulated and measured recoil quantities in Z-boson and W-boson events. Comparing the $u_{||}$ and $u_{\perp}$ (Fig. S31) distributions from data and simulation shows no evidence of bias. Since these distributions are not used as inputs for model tuning, they provide independent validation of the recoil model. The u_T distributions are also well modeled by the tuned simulation (Fig. S32). Z bosons decaying to forward ($|\eta| > 1$) electrons confirm the quality of the relative central-to-plug calorimeter calibration [43, 109].

The uncertainties on the M_W fits are obtained by propagating the recoil model parameter uncertainties (Table S5). The uncertainties due to the hadronic response (resolution) model are 1.8 (1.8) MeV, 3.5 (3.6) MeV, and 0.7 (5.2) MeV respectively on the m_T, p_T^ℓ and p_T^ν fits. The total uncertainty on M_W due to the recoil model is 2.6 MeV, 5.0

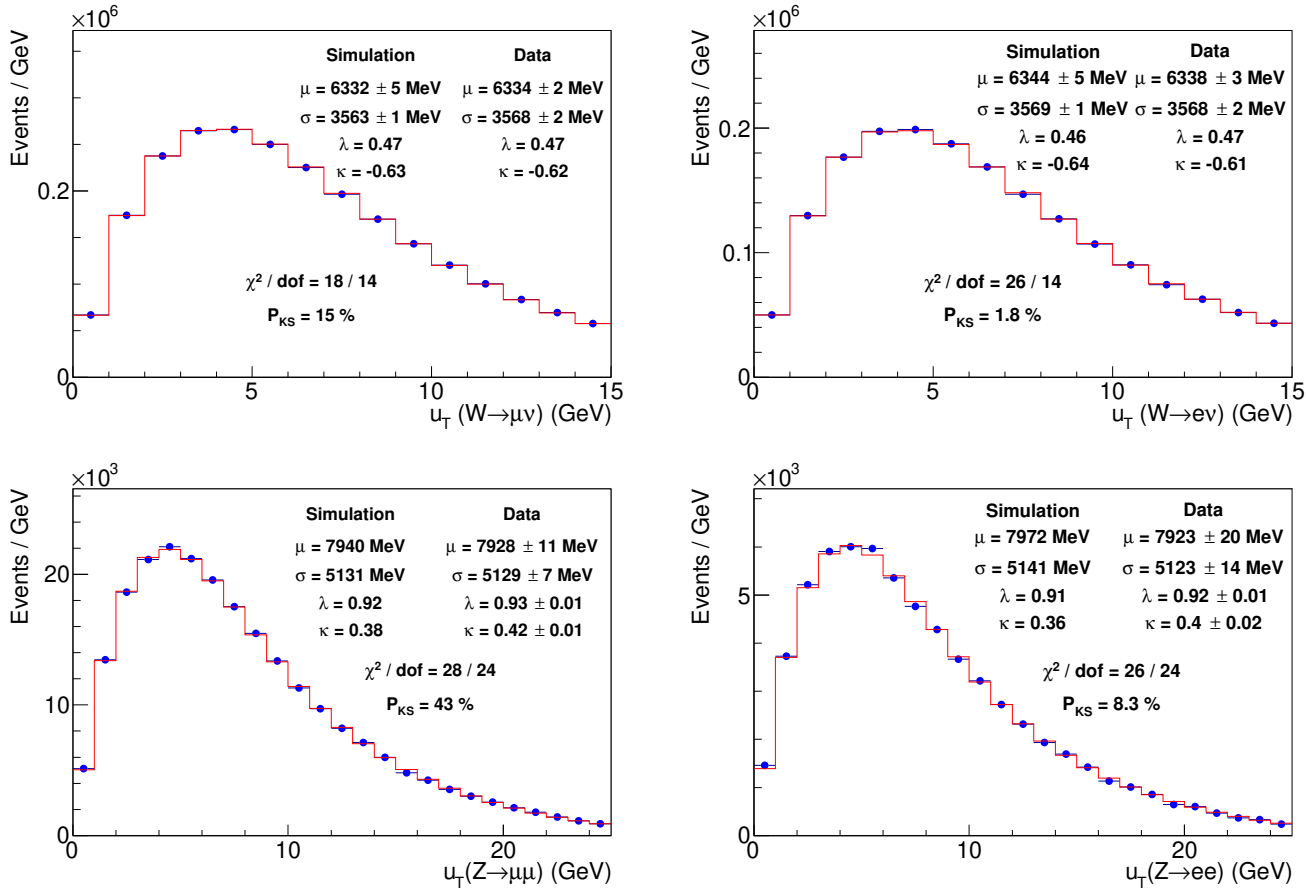

FIG. S32: Distributions of u_T from simulation (histogram) and data (circles) for W boson (top) and Z boson (bottom) decays in the muon (left) and electron (right) channels. The simulation uses parameters fit from Z boson data, and the uncertainty on the simulation is due to the statistical uncertainty on these parameters. The data mean (μ), rms spread (σ) skewness (λ), and excess kurtosis (κ) are well modeled by the simulation. The χ^2 values and the Kolmogorov-Smirnov (KS) probabilities are based only upon the statistical uncertainties in the data and do not take into account the systematic uncertainties in the simulation.

MeV, and 5.3 MeV from the m_T, p_T^ℓ, and p_T^ν fits, respectively. Since the recoil model parameters are obtained from combined fits to $Z \to ee$ and $Z \to \mu\mu$ data, with a constraint from the $W \to e\nu$ and $W \to \mu\nu$ data, the recoil model uncertainties are correlated between the electron and muon channels.

IX. BACKGROUNDS

Backgrounds in the W-boson samples arise from the following processes: $Z/\gamma^* \to \ell\ell$, where one lepton (electron or muon) is not detected; $W \to \tau\nu$ with a reconstructed lepton from the τ decay; and a jet misreconstructed as a lepton in multijet events. Backgrounds in the $W \to \mu\nu$ sample also arise from cosmic rays and long-lived hadrons decaying to muons.

A. $W \to \mu\nu$ Backgrounds

We model the $Z/\gamma^* \to \mu\mu$ background using events generated with the custom simulation. The key aspects of the custom simulation in this case are the muon-finding efficiency and the energy deposition by the muon in the calorimeters, both as functions of pseudorapidity. These detector characteristics are measured in $Z/\gamma^* \to \mu\mu$ data and

TABLE S5: Signed shifts in the M_W fit values, in MeV, due to 1σ increases in the recoil model parameters, after applying the p_T^W data spectrum as a constraint. The parameters are uncorrelated with each other and the resulting uncertainties are added in quadrature for a given fit. The signed shifts are used to propagate the correlations between fits. The "source" column indicates the distributions used for constraining each parameter.

Parameter	Description	Source	m_T	p_T^ℓ	p_T^ν
a	average response	Fig. S23	−1.6	−2.9	−0.2
b	response non-linearity	Fig. S23	−0.8	−2.0	0.7
Response			1.8	3.5	0.7
N_V	spectator interactions	Fig. S24	0.5	−3.2	3.6
$s_{\rm had}$	sampling resolution	Fig. S24	0.3	0.3	0.8
$f_{\pi^0}^4$	EM fluctuations at low u_T	Fig. S25	−0.3	−0.2	−1.0
$f_{\pi^0}^{15}$	EM fluctuations at high u_T	Fig. S25	−0.3	−0.3	−0.2
α	angular resolution at low u_T	Fig. S26	1.4	0.1	2.5
β	angular resolution at intermediate u_T	Fig. S26	0.2	0.1	0.7
γ	angular resolution at high u_T	Fig. S26	0.3	0.3	0.7
f_2^a	average dijet component	Fig. S27	0.1	−1.1	0.8
f_2^s	variation of dijet component with u_T	Fig. S27	−0.1	−0.2	−0.1
k_ξ	average dijet resolution	Fig. S28	−0.1	0.1	−0.3
δ_ξ	fluctuations in dijet resolution	Fig. S28	−0.2	0.2	−1.1
A_ξ	higher-order term in dijet resolution	Fig. S28	0.1	−1.0	0.7
μ_ξ	—"—	Fig. S28	−0.5	−0.4	−0.9
ϵ_ξ	—"—	Fig. S28	0.1	−0.2	0.4
S_ξ^+	—"—	Fig. S28	0.5	−0.4	1.4
S_ξ^-	—"—	Fig. S28	−0.3	−0.2	−0.5
q_ξ	—"—	Fig. S28	−0.2	0.0	0.2
Resolution			1.8	3.6	5.2

reproduced in the custom simulation. They are validated using a $Z/\gamma^* \to \mu\mu$ sample generated with PYTHIA [101, 102] and simulated with the full GEANT-based detector simulation. The uncertainty on this tuning is propagated to the M_W measurement as an uncertainty in the background normalization and shapes estimated for $Z/\gamma^* \to \mu\mu$ decays.

The ratio of $Z/\gamma^* \to \mu\mu$ to $W \to \mu\nu$ acceptances is determined from the custom simulation, and multiplied by the ratio of cross sections times branching ratios to obtain the $Z/\gamma^* \to \mu\mu$ background normalization. The standard model calculation of the ratio $\mathcal{R}_{W/Z} \equiv \sigma\mathcal{B}(W \to \mu\nu)/\sigma\mathcal{B}(Z \to \mu\mu)$ yields 10.96 ± 0.06 [72], including the uncertainties due to PDFs and the renormalization and factorization scale variations. We include an additional 1% uncertainty on the ratio of W and Z boson acceptances due to the uncertainty in the muon-finding efficiency, and obtain the estimate for the $Z/\gamma^* \to \mu\mu$ background in the $W \to \mu\nu$ candidate sample of $(7.37 \pm 0.10)\%$. The bulk of this background arises from muons with $|\eta| \gtrsim 1$ escaping the tracker acceptance.

The normalization and the shapes of the kinematic spectra for the $Z \to \mu\mu$ background are varied by changing the recoil model and the muon energy deposition in the calorimeters in the custom simulation by their uncertainties. The normalization has fractional uncertainties of 1.2% from $\mathcal{R}_{W/Z}$, 0.1% from the muon energy deposition, 0.2% from recoil resolution, and 0.1% from recoil scale, for a total normalization fractional uncertainty of 1.3%. The uncertainty on the W boson mass from the normalization uncertainty of this background is $(1.6, 3.6, 0.1)$ MeV respectively on the (m_T, p_T^μ, p_T^ν) fits. The variation in the shapes due to recoil response tuning, recoil resolution tuning, and the muon energy deposition causes uncertainties of $(0.1, 0.2, 0.2)$ MeV, $(0.2, 0.1, 0.4)$ MeV, and $(0.7, 0.1, 1.4)$ MeV on the (m_T, p_T^μ, p_T^ν) fits, respectively.

The $W \to \tau\nu$ background is estimated from the custom simulation, which generates $W \to \tau\nu$ events in the same way as $W \to e\nu$ and $W \to \mu\nu$ events, and which includes the τ polarization and decay dynamics as described in Ref. [43]. The custom simulation predicts $(0.880 \pm 0.004)\%$ for the $W \to \tau\nu$ background fraction, where the uncertainty is due to the uncertainty in the hadronic recoil model.

Background from multijet events where a jet mimics a muon track is estimated using an artificial neural network (NN) [110] to distinguish such misidentified muons from signal muons. The method, described in Refs. [43, 107], uses

the isolation variables, that is the calorimeter energy and track momenta in a cone surrounding the muon candidate with radius $\Delta R = \sqrt{(\Delta\eta)^2 + (\Delta\phi)^2} = 0.4$ in the $\eta - \phi$ plane. The distribution of the NN output for the W-boson data is fitted to the sum of the signal and background distributions, with the background fraction as the free parameter for χ^2 minimization. The signal sample is obtained from $W \to \mu\nu$ events generated with PYTHIA [101, 102] and the CDF GEANT-based simulation [86]. The background sample is obtained from data satisfying the $W \to \mu\nu$ selection criteria except for the additional criteria of $p_T^\nu < 10$ GeV and $u_T < 45$ GeV. The jet misidentification background is computed separately for $|\eta| < 0.6$ and $|\eta| > 0.6$ since different muon detectors operate in these regions. The background fractions are found to be consistent with each other and with zero. For the M_W measurement we use the combined best-fit fraction of $(0.01 \pm 0.04_{\rm stat})\%$.

The decay-in-flight (DIF) background is caused by low-momentum, long-lived mesons such as pions or kaons decaying to muons in the tracking volume, resulting in the reconstruction of high-p_T kinked tracks. As described in Ref. [43], the pattern of hit residuals indicating such kinks, the track impact parameter, and the fit quality are used to both reduce and estimate the DIF background. The distribution of the track fit χ^2/dof from $W \to \mu\nu$ candidates in the data are fit to a sum of signal and DIF background templates with the background fraction as the free parameter. Muons from $Z \to \mu\mu$ data are used to provide the signal template and $W \to \mu\nu$ data with large track impact parameters ($2 < d_0 < 5$ mm) provide the DIF background template. The contamination of real $W \to \mu\nu$ events in the background template due to the d_0 resolution is taken into account using the $Z \to \mu\mu$ data. The DIF background fraction is estimated to be $(0.20 \pm 0.14)\%$. Systematic uncertainties are estimated by comparing background templates made from different impact-parameter regions and from different requirements on the hit residual patterns.

Muons from cosmic rays are removed with efficiency greater than 99% using a dedicated tracking algorithm [51]. The cosmic-ray background estimated for a previous data set [39] is reduced by the ratio of run-time to integrated luminosity to obtain the background fraction of $(0.01 \pm 0.01)\%$ in the current sample.

TABLE S6: Various background fractions in the $W \to \mu\nu$ data set, and the corresponding uncertainties on the m_T, p_T^μ, and p_T^ν fits for M_W due to background normalization and shape (in parentheses). Where applicable, a negative sign is used to indicate a negative correlation between fits.

	Fraction	δM_W (MeV)		
Source	(%)	m_T fit	p_T^μ fit	p_T^ν fit
$Z/\gamma^* \to \mu\mu$	7.37 ± 0.10	1.6 (0.7)	3.6 (0.3)	0.1 (1.5)
$W \to \tau\nu$	0.880 ± 0.004	0.1 (0.0)	0.1 (0.0)	0.1 (0.0)
Hadronic jets	0.01 ± 0.04	0.1 (0.8)	-0.6 (0.8)	2.4 (0.5)
Decays in flight	0.20 ± 0.14	1.3 (3.1)	1.3 (5.0)	-5.2 (3.2)
Cosmic rays	0.01 ± 0.01	0.3 (0.0)	0.5 (0.0)	0.3 (0.3)
Total	8.47 ± 0.18	2.1 (3.3)	3.9 (5.1)	5.7 (3.6)

TABLE S7: Background fractions from various sources in the $W \to e\nu$ data set, and the corresponding uncertainties on the m_T, p_T^e, and p_T^ν fits for M_W due to background normalization and shape (in parentheses). Where applicable, a negative sign is used to indicate a negative correlation between fits.

	Fraction	δM_W (MeV)		
Source	(%)	m_T fit	p_T^e fit	p_T^ν fit
$Z/\gamma^* \to ee$	0.134 ± 0.003	0.2 (0.3)	0.3 (0.0)	0.0 (0.6)
$W \to \tau\nu$	0.94 ± 0.01	0.6 (0.0)	0.6 (0.0)	0.6 (0.0)
Hadronic jets	0.34 ± 0.08	2.2 (1.2)	0.9 (6.5)	6.2 (−1.1)
Total	1.41 ± 0.08	2.3 (1.2)	1.1 (6.5)	6.2 (1.3)

The m_T, p_T^μ, and p_T^ν distributions for the various backgrounds are added to the signal simulation templates for the M_W fits. The background templates are obtained from the custom simulation for W and Z boson backgrounds, from identified cosmic ray events for the cosmic ray background, and from muons in $W \to \mu\nu$ events with large d_0 and DIF-like hit residuals (isolation) for the decay-in-flight (hadronic jet) background. After including uncertainties on the shapes of the distributions, the total uncertainties on the background estimates result in uncertainties of 3.9, 6.4, and 6.8 MeV on M_W for the m_T, p_T^μ, and p_T^ν fits, respectively (Table S6).

B. $W \to e\nu$ Backgrounds

We model the $Z/\gamma^* \to ee$ background using the custom simulation. It is important to model the uninstrumented regions (cracks) in the EM calorimeter, and the EM and hadronic calorimeter response in these cracks. We tune the custom simulation of these detector attributes using a control sample of $Z/\gamma^* \to ee$ data, in which one electron is the fiducial electron and the second is associated with a track pointing toward a crack region. The tuned simulation reproduces the rate for the second electron to pass through the crack regions, as well as the distributions of the ratios

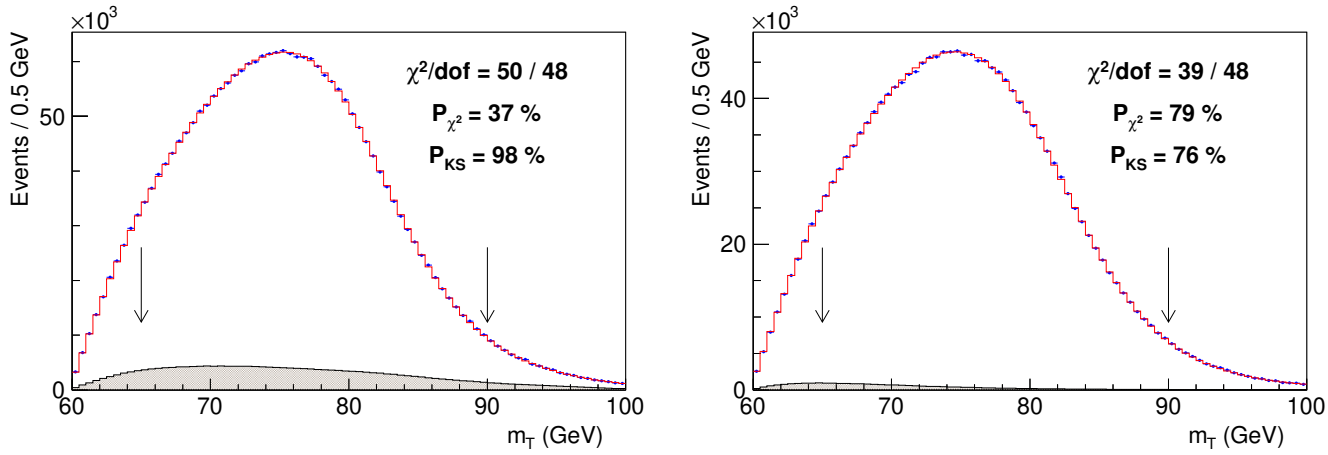

FIG. S33: Distributions of m_T for W boson decays to $\mu\nu$ (left) and $e\nu$ (right) final states in simulated (histogram) and experimental (points) data. The simulated distribution is based on the true W-boson mass value that maximizes the likelihood in data and includes backgrounds (shaded). The likelihood is computed using events between the two arrows.

of EM and hadronic energies to the track momentum of the electron in the crack. The acceptance for this background is validated with the CDF GEANT-based simulation. Following the same procedure as used to estimate the $Z/\gamma^* \to \mu\mu$ background (Sec. IX A), we estimate the $Z/\gamma^* \to ee$ background fraction to be $(0.134 \pm 0.003)\%$.

We model the $W \to \tau\nu$ background using our custom simulation, as with the $W \to \mu\nu$ channel, and find a background fraction of $(0.94 \pm 0.01)\%$, which is consistent with the CDF GEANT-based prediction.

Multijet events are a source of background because hadronic jets can be misreconstructed as electrons. As described in Ref. [43], the background fraction is determined by fitting the sum of signal and background templates to the $W \to e\nu$ sample template. The template variables used are the track isolation, an NN-based electron discriminant, and missing transverse energy. Comparing the results from these three fits, the multijet background fraction and its systematic uncertainty is estimated to be $(0.34 \pm 0.08)\%$.

The custom simulation is used to obtain the distributions of the M_W fit variables for the W and Z boson backgrounds. Electron candidates in the $W \to e\nu$ data sample with non-electron-like NN discriminant values are used to provide the hadronic jet background distributions. After including these background distributions in the M_W fits, the uncertainties on the background normalizations and shapes result in uncertainties of 2.6, 6.6, and 6.4 MeV on M_W from the m_T, p_T^e, and p_T^ν fits, respectively (Table S7).

X. LIKELIHOOD FITS FOR THE W-BOSON MASS

The W boson mass is extracted by performing binned maximum-likelihood fits to a sum of background and simulated signal templates of the m_T, p_T^ℓ, and p_T^ν distributions, as described in Ref. [43]. Templates are generated in 0.2 MeV steps in the boson mass and are normalized to the data in the fit range. The likelihood is a function of the pole mass M_W, defined by the relativistic Breit-Wigner mass distribution [43]. We use the standard model value, $\Gamma_W = 2\,089.5 \pm 0.6$ MeV [10], for the W boson width. Its uncertainty has a negligible impact on the measured value of M_W.

A. Fit results

The m_T fit is performed in the range $65 < m_T < 90$ GeV, while the p_T^ℓ and p_T^ν fits are both performed in the range $32 < p_T < 48$ GeV. Figures S33–S35 show the respective distributions in data with the best-fit simulation overlaid, and Figs. S36–S38 show the differences between data and simulation divided by the statistical uncertainties on the predictions. Table S8 lists the uncertainties in detail, and all results are summarized in Table I of the main text.

The best linear unbiased estimator is used to combine individual fit results [66]. Sources of systematic uncertainty are taken to be independent of each other for a given fit. The statistical correlation between fits to the m_T, p_T^ℓ, and p_T^ν distributions was estimated from pseudoexperiments in Ref. [43]. The values of these combinations, their respective

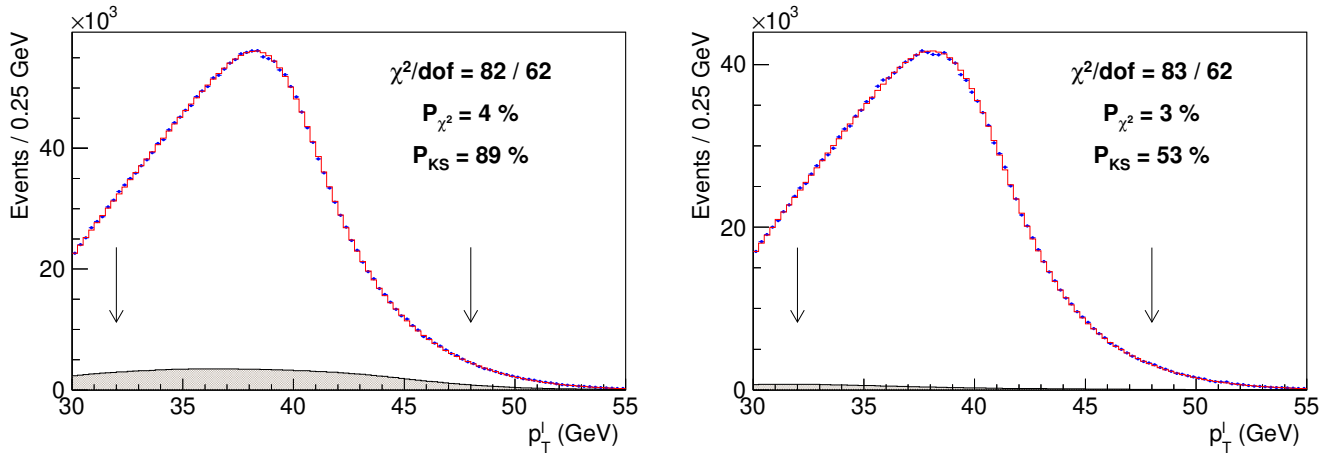

FIG. S34: Distributions of p_T^ℓ for W boson decays to $\mu\nu$ (left) and $e\nu$ (right) final states in simulated (histogram) and experimental (points) data. The simulated distribution is based on the true W-boson mass value that maximizes the likelihood in data and includes backgrounds (shaded). The likelihood is computed using events between the two arrows.

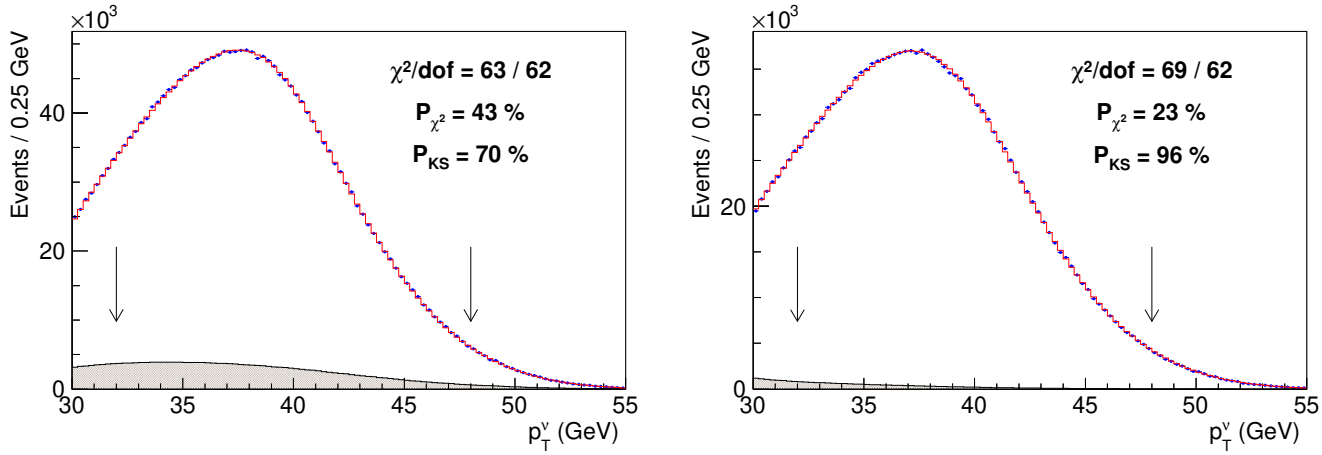

FIG. S35: Distributions of p_T^ν for W boson decays to $\mu\nu$ (left) and $e\nu$ (right) final states in simulated (histogram) and experimental (points) data. The simulated distribution is based on the true W-boson mass value that maximizes the likelihood in data and includes backgrounds (shaded). The likelihood is computed using events between the two arrows.

inputs, χ^2/dof and the probability of obtaining a χ^2/dof at least as large, are summarized in Table S9.

B. Consistency checks

We compare the electron and muon p_T^ℓ fit results obtained from subsamples of the data chosen to enhance possible residual instrumental effects (Table S10). The uncertainty on the difference between the $W^+ \to \mu^+\nu$ and $W^- \to \mu^-\nu$ fits includes the uncertainty due to the COT alignment (the uncertainty in the intercept of the linear fit in Fig. S6), which contributes to this mass splitting. The mass fit differences for the electron channel are shown with and without applying an E/p-based calibration from the corresponding subsample. The stability of the momentum and energy scales is verified by performing Z-boson mass fits in subsamples separated in chronological time (indicated by run number in Table S10).

We additionally test the stability of the mass fits as the fit ranges are varied. The variations of the fitted mass values relative to the nominal results are consistent with expected statistical fluctuations, as shown in Figs. S39-S41 [107].

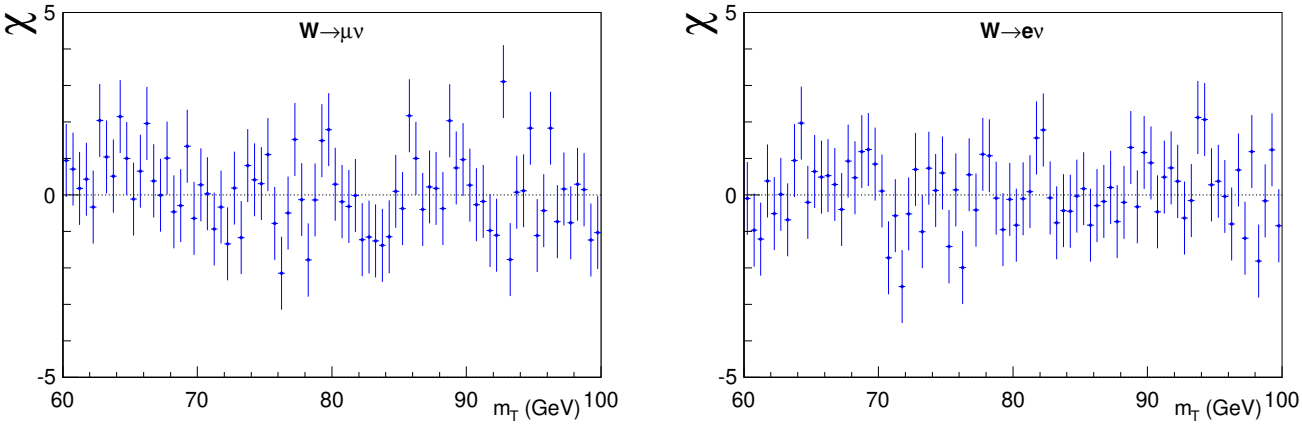

FIG. S36: Differences between the data and simulation, divided by the expected statistical uncertainty, for the m_T distributions in the muon (left) and electron (right) channels.

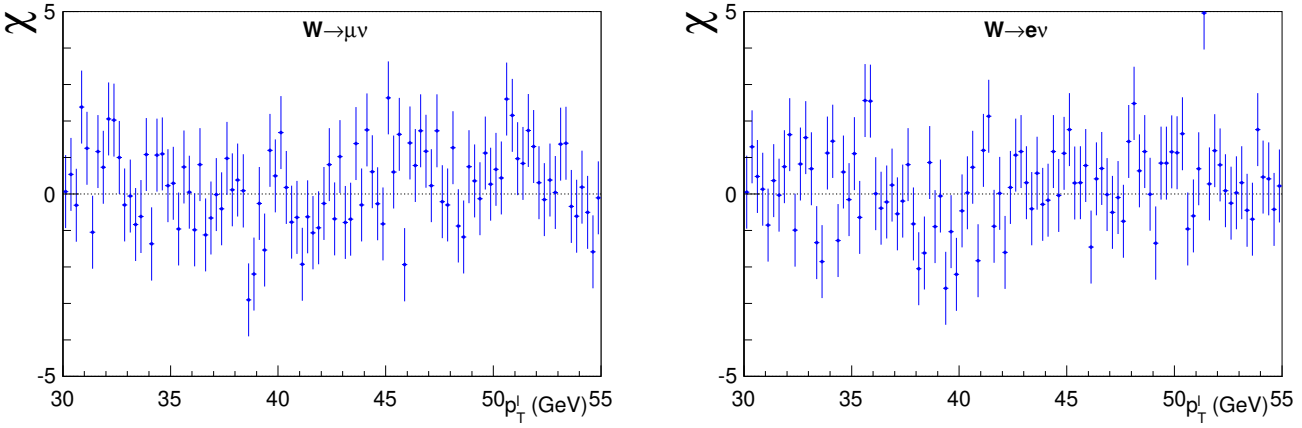

FIG. S37: Differences between the data and simulation, divided by the expected statistical uncertainty, for the p_T^ℓ distributions in the muon (left) and electron (right) channels.

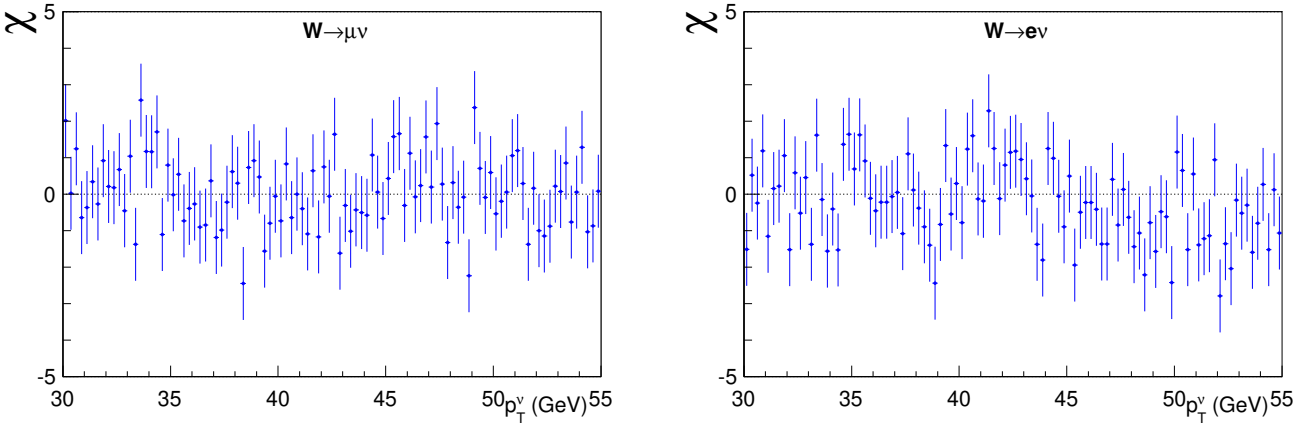

FIG. S38: Differences between the data and simulation, divided by the expected statistical uncertainty, for the p_T^ν distributions in the muon (left) and electron (right) channels.

Source of systematic uncertainty	m_T fit			p_T^ℓ fit			p_T^ν fit		
	Electrons	Muons	Common	Electrons	Muons	Common	Electrons	Muons	Common
Lepton energy scale	5.8	2.1	1.8	5.8	2.1	1.8	5.8	2.1	1.8
Lepton energy resolution	0.9	0.3	-0.3	0.9	0.3	-0.3	0.9	0.3	-0.3
Recoil energy scale	1.8	1.8	1.8	3.5	3.5	3.5	0.7	0.7	0.7
Recoil energy resolution	1.8	1.8	1.8	3.6	3.6	3.6	5.2	5.2	5.2
Lepton $u_{\|\|}$ efficiency	0.5	0.5	0	1.3	1.0	0	2.6	2.1	0
Lepton removal	1.0	1.7	0	0	0	0	2.0	3.4	0
Backgrounds	2.6	3.9	0	6.6	6.4	0	6.4	6.8	0
p_T^Z model	0.7	0.7	0.7	2.3	2.3	2.3	0.9	0.9	0.9
p_T^W/p_T^Z model	0.8	0.8	0.8	2.3	2.3	2.3	0.9	0.9	0.9
Parton distributions	3.9	3.9	3.9	3.9	3.9	3.9	3.9	3.9	3.9
QED radiation	2.7	2.7	2.7	2.7	2.7	2.7	2.7	2.7	2.7
Statistical	10.3	9.2	0	10.7	9.6	0	14.5	13.1	0
Total	13.5	11.8	5.8	16.0	14.1	7.9	18.8	17.1	7.4

TABLE S8: Uncertainties on M_W (in MeV) as resulting from the transverse-mass, charged-lepton p_T and neutrino p_T fits in the $W \to \mu\nu$ and $W \to e\nu$ samples. The third column for each fit reports the portion of the uncertainty that is common in the $\mu\nu$ and $e\nu$ results. The muon and electron energy resolutions are anti-correlated because the track p_T resolution and the electron cluster E_T resolution both contribute to the width of the E/p peak, which is used to constrain the electron cluster E_T resolution.

Combination	m_T fit		p_T^ℓ fit		p_T^ν fit		Value (MeV)	χ^2/dof	Probability (%)
	Electrons	Muons	Electrons	Muons	Electrons	Muons			
m_T	✓	✓					80 439.0 ± 9.8	1.2 / 1	28
p_T^ℓ			✓	✓			80 421.2 ± 11.9	0.9 / 1	36
p_T^ν					✓	✓	80 427.7 ± 13.8	0.0 / 1	91
m_T & p_T^ℓ	✓	✓	✓	✓			80 435.4 ± 9.5	4.8 / 3	19
m_T & p_T^ν	✓	✓			✓	✓	80 437.9 ± 9.7	2.2 / 3	53
p_T^ℓ & p_T^ν			✓	✓	✓	✓	80 424.1 ± 10.1	1.1 / 3	78
Electrons	✓		✓		✓		80 424.6 ± 13.2	3.3 / 2	19
Muons		✓		✓		✓	80 437.9 ± 11.0	3.6 / 2	17
All	✓	✓	✓	✓	✓	✓	80 433.5 ± 9.4	7.4 / 5	20

TABLE S9: Combinations of various fit results (in MeV) and the associated uncertainties, χ^2, and χ^2-probabilities.

The systematic uncertainties considered in Table S8 would induce additional expected shifts upon changing fit ranges, which are not displayed in the error bars.

TABLE S10: Differences (in MeV) between W-mass p_T^ℓ-fit results and Z-mass fit results obtained from subsamples of our data with equal statistics. For the spatial and time dependence of the electron channel fit result, we show the dependence with (without) the corresponding cluster energy calibration using the subsample E/p fit.

Fit difference	Muon channel	Electron channel
$M_W(\ell^+) - M_W(\ell^-)$	$-7.8 \pm 18.5_{\rm stat} \pm 12.7_{\rm COT}$	$14.7 \pm 21.3_{\rm stat} \pm 7.7^{\rm E/p}_{\rm stat}$ $(0.4 \pm 21.3_{\rm stat})$
$M_W(\phi_\ell > 0) - M_W(\phi_\ell < 0)$	$24.4 \pm 18.5_{\rm stat}$	$9.9 \pm 21.3_{\rm stat} \pm 7.5^{\rm E/p}_{\rm stat}$ $(-0.8 \pm 21.3_{\rm stat})$
$M_Z(\text{run} > 271100) - M_Z(\text{run} < 271100)$	$5.2 \pm 12.2_{\rm stat}$	$63.2 \pm 29.9_{\rm stat} \pm 8.2^{\rm E/p}_{\rm stat}$ $(-16.0 \pm 29.9_{\rm stat})$

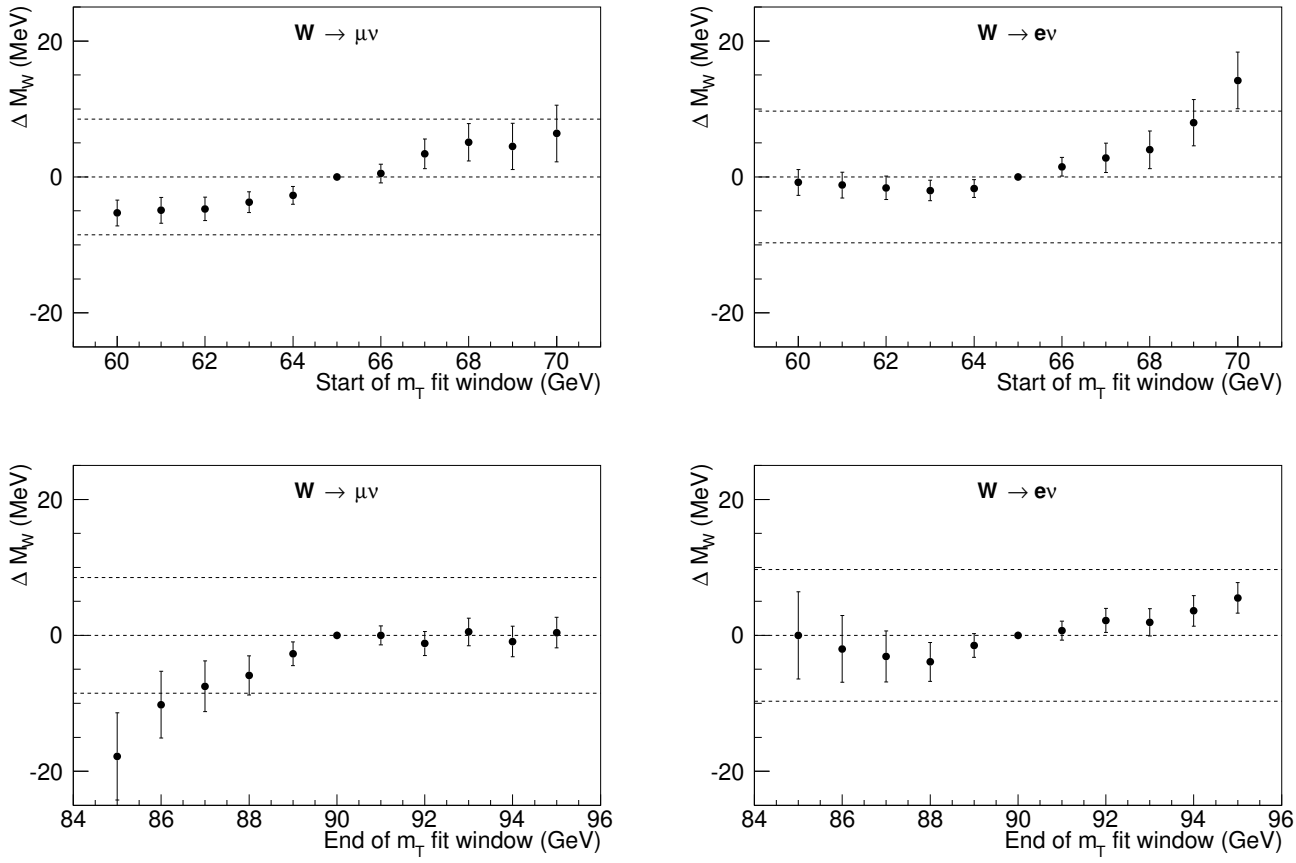

FIG. S39: Variations of the M_W value determined from the transverse-mass fit as a function of the choice of the lower (top) and upper (bottom) edge of the fit range, for the muon (left) and electron (right) channels. Uncertainty bars indicate the expected statistical variation with respect to the default fit range, as computed using pseudoexperiments. The dashed lines indicate the statistical uncertainty from the default mass fit.

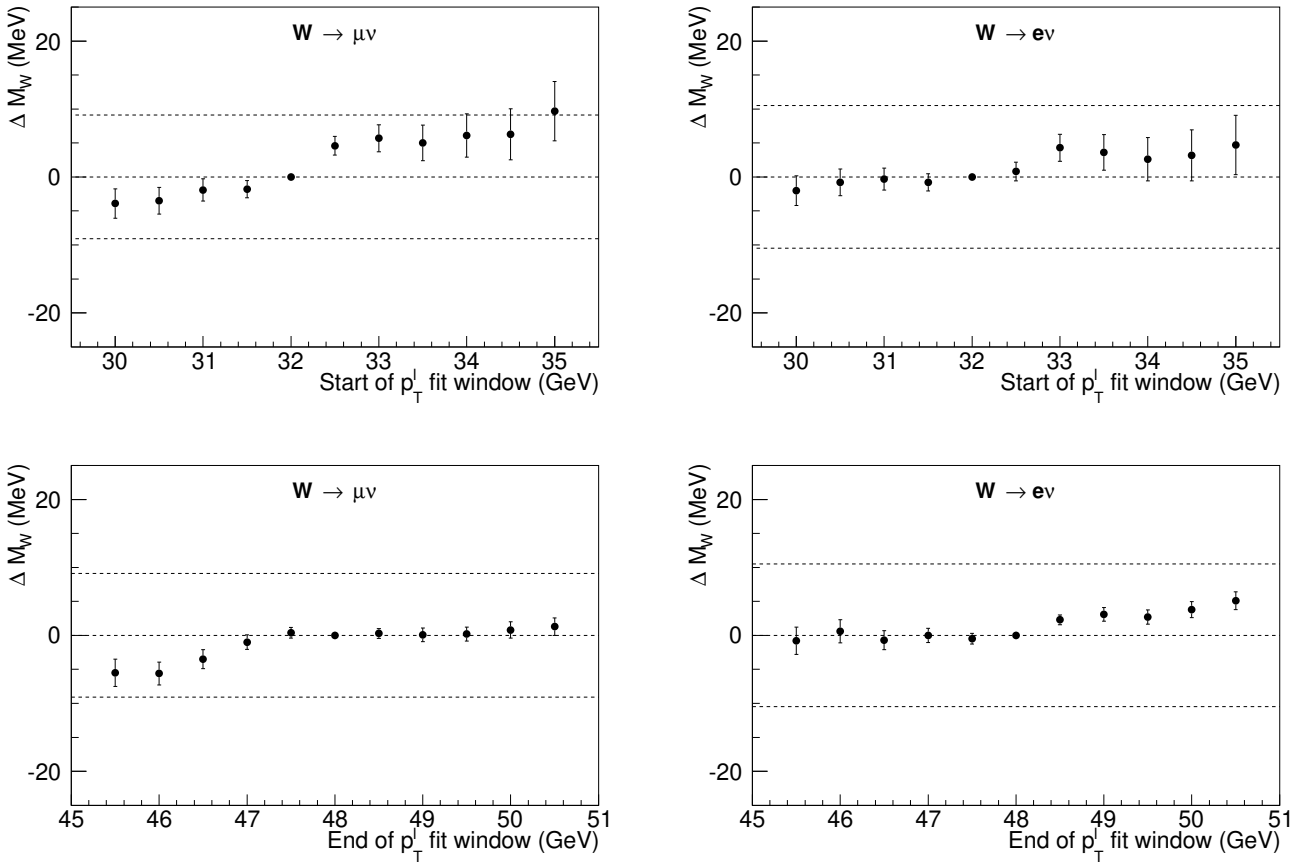

FIG. S40: Variations of the M_W value determined from the charged-lepton transverse-momentum fit as a function of the choice of the lower (top) and upper (bottom) edge of the fit range, for the muon (left) and electron (right) channels. Uncertainty bars indicate the expected statistical variation with respect to the default fit range, as computed using pseudoexperiments. The dashed lines indicate the statistical uncertainty from the default mass fit.

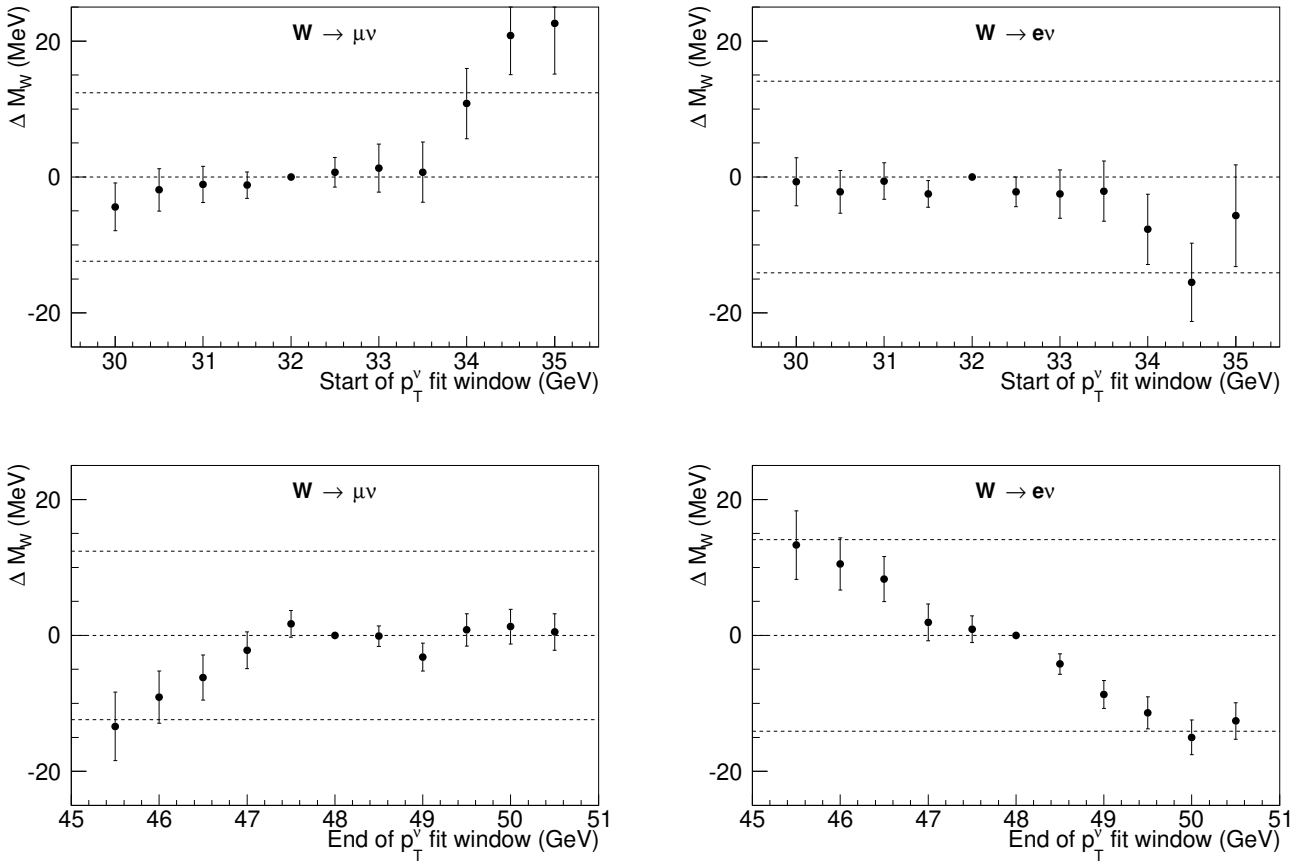

FIG. S41: Variations of the M_W value determined from the neutrino-transverse-momentum fit as a function of the choice of the lower (top) and upper (bottom) edge of the fit range, for the muon (left) and electron (right) channels. Uncertainty bars indicate the expected statistical variation with respect to the default fit range, as computed using pseudoexperiments. The dashed lines indicate the statistical uncertainty from the default mass fit.

References and Notes

1. P. W. Anderson, Plasmons, Gauge Invariance, and Mass. *Phys. Rev.* **130**, 439–442 (1963). doi:10.1103/PhysRev.130.439

2. F. Englert, R. Brout, Broken Symmetry and the Mass of Gauge Vector Mesons. *Phys. Rev. Lett.* **13**, 321–323 (1964). doi:10.1103/PhysRevLett.13.321

3. P. W. Higgs, Broken Symmetries and the Masses of Gauge Bosons. *Phys. Rev. Lett.* **13**, 508–509 (1964). doi:10.1103/PhysRevLett.13.508

4. G. S. Guralnik, C. R. Hagen, T. W. B. Kibble, Global Conservation Laws and Massless Particles. *Phys. Rev. Lett.* **13**, 585–587 (1964). doi:10.1103/PhysRevLett.13.585

5. G. Aad *et al*.; ATLAS Collaboration, Observation of a new particle in the search for the Standard Model Higgs boson with the ATLAS detector at the LHC. *Phys. Lett. B* **716**, 1–29 (2012). doi:10.1016/j.physletb.2012.08.020

6. S. Chatrchyan *et al*.; CMS Collaboration, Observation of a new boson at a mass of 125 GeV with the CMS experiment at the LHC. *Phys. Lett. B* **716**, 30–61 (2012). doi:10.1016/j.physletb.2012.08.021

7. S. Glashow, Partial-symmetries of weak interactions. *Nucl. Phys.* **22**, 579–588 (1961). doi:10.1016/0029-5582(61)90469-2

8. A. Salam, J. C. Ward, Electromagnetic and weak interactions. *Phys. Lett.* **13**, 168–171 (1964). doi:10.1016/0031-9163(64)90711-5

9. S. Weinberg, A Model of Leptons. *Phys. Rev. Lett.* **19**, 1264–1266 (1967). doi:10.1103/PhysRevLett.19.1264

10. P. A. Zyla, R. M. Barnett, J. Beringer, O. Dahl, D. A. Dwyer, D. E. Groom, C.-J. Lin, K. S. Lugovsky, E. Pianori, D. J. Robinson, C. G. Wohl, W.-M. Yao, K. Agashe, G. Aielli, B. C. Allanach, C. Amsler, M. Antonelli, E. C. Aschenauer, D. M. Asner, H. Baer, S. Banerjee, L. Baudis, C. W. Bauer, J. J. Beatty, V. I. Belousov, S. Bethke, A. Bettini, O. Biebel, K. M. Black, E. Blucher, O. Buchmuller, V. Burkert, M. A. Bychkov, R. N. Cahn, M. Carena, A. Ceccucci, A. Cerri, D. Chakraborty, R. S. Chivukula, G. Cowan, G. D'Ambrosio, T. Damour, D. de Florian, A. de Gouvêa, T. DeGrand, P. de Jong, G. Dissertori, B. A. Dobrescu, M. D'Onofrio, M. Doser, M. Drees, H. K. Dreiner, P. Eerola, U. Egede, S. Eidelman, J. Ellis, J. Erler, V. V. Ezhela, W. Fetscher, B. D. Fields, B. Foster, A. Freitas, H. Gallagher, L. Garren, H.-J. Gerber, G. Gerbier, T. Gershon, Y. Gershtein, T. Gherghetta, A. A. Godizov, M. C. Gonzalez-Garcia, M. Goodman, C. Grab, A. V. Gritsan, C. Grojean, M. Grünewald, A. Gurtu, T. Gutsche, H. E. Haber, C. Hanhart, S. Hashimoto, Y. Hayato, A. Hebecker, S. Heinemeyer, B. Heltsley, J. J. Hernández-Rey, K. Hikasa, J. Hisano, A. Höcker, J. Holder, A. Holtkamp, J. Huston, T. Hyodo, K. F. Johnson, M. Kado, M. Karliner, U. F. Katz, M. Kenzie, V. A. Khoze, S. R. Klein, E. Klempt, R. V. Kowalewski, F. Krauss, M. Kreps, B. Krusche, Y. Kwon, O. Lahav, J. Laiho, L. P. Lellouch, J. Lesgourgues, A. R. Liddle, Z. Ligeti, C. Lippmann, T. M. Liss, L. Littenberg, C. Lourengo, S. B. Lugovsky, A. Lusiani, Y. Makida, F. Maltoni, T. Mannel, A. V. Manohar, W. J. Marciano, A. Masoni, J. Matthews, U.-G. Meißner, M. Mikhasenko, D. J. Miller, D. Milstead, R. E. Mitchell, K. Mönig, P. Molaro, F. Moortgat,

M. Moskovic, K. Nakamura, M. Narain, P. Nason, S. Navas, M. Neubert, P. Nevski, Y. Nir, K. A. Olive, C. Patrignani, J. A. Peacock, S. T. Petcov, V. A. Petrov, A. Pich, A. Piepke, A. Pomarol, S. Profumo, A. Quadt, K. Rabbertz, J. Rademacker, G. Raffelt, H. Ramani, M. Ramsey-Musolf, B. N. Ratcliff, P. Richardson, A. Ringwald, S. Roesler, S. Rolli, A. Romaniouk, L. J. Rosenberg, J. L. Rosner, G. Rybka, M. Ryskin, R. A. Ryutin, Y. Sakai, G. P. Salam, S. Sarkar, F. Sauli, O. Schneider, K. Scholberg, A. J. Schwartz, J. Schwiening, D. Scott, V. Sharma, S. R. Sharpe, T. Shutt, M. Silari, T. Sjöstrand, P. Skands, T. Skwarnicki, G. F. Smoot, A. Soffer, M. S. Sozzi, S. Spanier, C. Spiering, A. Stahl, S. L. Stone, Y. Sumino, T. Sumiyoshi, M. J. Syphers, F. Takahashi, M. Tanabashi, J. Tanaka, M. Taševský, K. Terashi, J. Terning, U. Thoma, R. S. Thorne, L. Tiator, M. Titov, N. P. Tkachenko, D. R. Tovey, K. Trabelsi, P. Urquijo, G. Valencia, R. Van de Water, N. Varelas, G. Venanzoni, L. Verde, M. G. Vincter, P. Vogel, W. Vogelsang, A. Vogt, V. Vorobyev, S. P. Wakely, W. Walkowiak, C. W. Walter, D. Wands, M. O. Wascko, D. H. Weinberg, E. J. Weinberg, M. White, L. R. Wiencke, S. Willocq, C. L. Woody, R. L. Workman, M. Yokoyama, R. Yoshida, G. Zanderighi, G. P. Zeller, O. V. Zenin, R.-Y. Zhu, S.-L. Zhu, F. Zimmermann, J. Anderson, T. Basaglia, V. S. Lugovsky, P. Schaffner, W. Zheng; Particle Data Group, Review of Particle Physics. *Prog. Theor. Exp. Phys.* **2020**, 083C01 (2020). doi:10.1093/ptep/ptaa104

11. J. Feng, Naturalness and the Status of Supersymmetry. *Annu. Rev. Nucl. Part. Sci.* **63**, 351–382 (2013). doi:10.1146/annurev-nucl-102010-130447

12. R. Contino, T. Krämer, M. Son, R. Sundrum, Warped/composite phenomenology simplified. *J. High Energy Phys.* **2007**, 074 (2007). doi:10.1088/1126-6708/2007/05/074

13. G. Bertone, D. Hooper, J. Silk, Particle dark matter: Evidence, candidates and constraints. *Phys. Rep.* **405**, 279–390 (2005). doi:10.1016/j.physrep.2004.08.031

14. J. L. Feng, Dark Matter Candidates from Particle Physics and Methods of Detection. *Annu. Rev. Astron. Astrophys.* **48**, 495–545 (2010). doi:10.1146/annurev-astro-082708-101659

15. S. Heinemeyer, W. Hollik, G. Weiglein, L. Zeune, Implications of LHC search results on the W boson mass prediction in the MSSM. *J. High Energy Phys.* **2013**, 84 (2013). doi:10.1007/JHEP12(2013)084

16. S. Heinemeyer, "Electroweak precision observables and BSM physics," presented at the Snowmass EF04 meeting, 17 July 2020; https://indico.fnal.gov/event/43577/contributions/191539/attachments/131503/161060/sven.pdf.

17. D. López-Val, T. Robens, Δ*r* and the W-boson mass in the singlet extension of the standard model. *Phys. Rev. D* **90**, 114018 (2014). doi:10.1103/PhysRevD.90.114018

18. D. López-Val, J. Sola, Δ*r* in the Two-Higgs-Doublet Model at full one loop level—and beyond. *Eur. Phys. J. C* **73**, 2393 (2013). doi:10.1140/epjc/s10052-013-2393-y

19. D. Curtin, R. Essig, S. Gori, J. Shelton, Illuminating dark photons with high-energy colliders. *J. High Energy Phys.* **2015**, 157 (2015). doi:10.1007/JHEP02(2015)157

20. J. Chakrabortty, J. Gluza, R. Sevillano, R. Szafron, Left-right symmetry at LHC and precise 1-loop low energy data. *J. High Energy Phys.* **2012**, 38 (2012). doi:10.1007/JHEP07(2012)038

21. B. Bellazzini, C. Csáki, J. Serra, Composite Higgses. *Eur. Phys. J. C* **74**, 2766 (2014). doi:10.1140/epjc/s10052-014-2766-x

22. A. Pomarol, F. Riva, Towards the ultimate SM fit to close in on Higgs physics. *J. High Energy Phys.* **2014**, 151 (2014). doi:10.1007/JHEP01(2014)151

23. G. F. Giudice, C. Grojean, A. Pomarol, R. Rattazzi, The strongly-interacting light Higgs. *J. High Energy Phys.* **2007**, 045 (2007). doi:10.1088/1126-6708/2007/06/045

24. S. F. Ge, H. J. He, R. Q. Xiao, Probing new physics scales from Higgs and electroweak observables at $e^+ e^-$ Higgs factory. *J. High Energy Phys.* **2016**, 7 (2016). doi:10.1007/JHEP10(2016)007

25. We use the convention $\hbar = c \equiv 1$ throughout this paper.

26. M. Awramik, M. Czakon, A. Freitas, G. Weiglein, Precise prediction for the *W*-boson mass in the standard model. *Phys. Rev. D* **69**, 053006 (2004). doi:10.1103/PhysRevD.69.053006

27. J. Erler, M. Schott, Electroweak precision tests of the Standard Model after the discovery of the Higgs boson. *Prog. Part. Nucl. Phys.* **106**, 68–119 (2019). doi:10.1016/j.ppnp.2019.02.007

28. T. Affolder, H. Akimoto, A. Akopian, M. Albrow, P. Amaral, S. Amendolia, D. Amidei, K. Anikeev, J. Antos, G. Apollinari, T. Arisawa, T. Asakawa, W. Ashmanskas, M. Atac, F. Azfar, P. Azzi-Bacchetta, N. Bacchetta, M. Bailey, S. Bailey, P. de Barbaro, A. Barbaro-Galtieri, V. Barnes, B. Barnett, M. Barone, G. Bauer, F. Bedeschi, S. Belforte, G. Bellettini, J. Bellinger, D. Benjamin, J. Bensinger, A. Beretvas, J. Berge, J. Berryhill, B. Bevensee, A. Bhatti, M. Binkley, D. Bisello, R. Blair, C. Blocker, K. Bloom, B. Blumenfeld, S. Blusk, A. Bocci, A. Bodek, W. Bokhari, G. Bolla, Y. Bonushkin, D. Bortoletto, J. Boudreau, A. Brandl, S. van den Brink, C. Bromberg, M. Brozovic, N. Bruner, E. Buckley-Geer, J. Budagov, H. Budd, K. Burkett, G. Busetto, A. Byon-Wagner, K. Byrum, P. Calafiura, M. Campbell, W. Carithers, J. Carlson, D. Carlsmith, J. Cassada, A. Castro, D. Cauz, A. Cerri, A. Chan, P. Chang, P. Chang, J. Chapman, C. Chen, Y. Chen, M.-T. Cheng, M. Chertok, G. Chiarelli, I. Chirikov-Zorin, G. Chlachidze, F. Chlebana, L. Christofek, M. Chu, Y. Chung, C. Ciobanu, A. Clark, A. Connolly, J. Conway, J. Cooper, M. Cordelli, J. Cranshaw, D. Cronin-Hennessy, R. Cropp, R. Culbertson, D. Dagenhart, F. DeJongh, S. Dell'Agnello, M. Dell'Orso, R. Demina, L. Demortier, M. Deninno, P. Derwent, T. Devlin, J. Dittmann, S. Donati, J. Done, T. Dorigo, N. Eddy, K. Einsweiler, J. Elias, E. Engels, W. Erdmann, D. Errede, S. Errede, Q. Fan, R. Feild, C. Ferretti, R. Field, I. Fiori, B. Flaugher, G. Foster, M. Franklin, J. Freeman, J. Friedman, Y. Fukui, I. Furic, S. Galeotti, M. Gallinaro, T. Gao, M. Garcia-Sciveres, A. Garfinkel, P. Gatti, C. Gay, S. Geer, D. Gerdes, P. Giannetti, P. Giromini, V. Glagolev, M. Gold, J. Goldstein, A. Gordon, A. Goshaw, Y. Gotra, K. Goulianos, C. Green, L. Groer, C. Grosso-Pilcher, M. Guenther, G. Guillian, J. Guimaraes da Costa, R. Guo, R. Haas, C. Haber, E. Hafen, S. Hahn, C. Hall, T. Handa, R. Handler, W. Hao, F. Happacher, K. Hara, A. Hardman, R. Harris, F. Hartmann, K. Hatakeyama, J. Hauser, J. Heinrich, A. Heiss, M. Herndon, K. Hoffman, C. Holck, R. Hollebeek, L. Holloway, R. Hughes, J. Huston, J. Huth, H. Ikeda, J. Incandela, G. Introzzi, J. Iwai, Y. Iwata, E. James, H. Jensen, M. Jones, U. Joshi, H. Kambara, T. Kamon, T. Kaneko, K. Karr, H.

Kasha, Y. Kato, T. Keaffaber, K. Kelley, M. Kelly, R. Kennedy, R. Kephart, D. Khazins, T. Kikuchi, B. Kilminster, M. Kirby, M. Kirk, B. Kim, D. Kim, H. Kim, M. Kim, S. Kim, Y. Kim, L. Kirsch, S. Klimenko, P. Koehn, A. Köngeter, K. Kondo, J. Konigsberg, K. Kordas, A. Korn, A. Korytov, E. Kovacs, J. Kroll, M. Kruse, S. Kuhlmann, K. Kurino, T. Kuwabara, A. Laasanen, N. Lai, S. Lami, S. Lammel, J. Lamoureux, M. Lancaster, G. Latino, T. LeCompte, A. Lee, K. Lee, S. Leone, J. Lewis, M. Lindgren, T. Liss, J. Liu, Y. Liu, N. Lockyer, J. Loken, M. Loreti, D. Lucchesi, P. Lukens, S. Lusin, L. Lyons, J. Lys, R. Madrak, K. Maeshima, P. Maksimovic, L. Malferrari, M. Mangano, M. Mariotti, G. Martignon, A. Martin, J. Matthews, J. Mayer, P. Mazzanti, K. McFarland, P. McIntyre, E. McKigney, M. Menguzzato, A. Menzione, C. Mesropian, A. Meyer, T. Miao, R. Miller, J. Miller, H. Minato, S. Miscetti, M. Mishina, G. Mitselmakher, N. Moggi, E. Moore, R. Moore, Y. Morita, M. Mulhearn, A. Mukherjee, T. Muller, A. Munar, P. Murat, S. Murgia, M. Musy, J. Nachtman, S. Nahn, H. Nakada, T. Nakaya, I. Nakano, C. Nelson, D. Neuberger, C. Newman-Holmes, C.-Y. Ngan, P. Nicolaidi, H. Niu, L. Nodulman, A. Nomerotski, S. Oh, T. Ohmoto, T. Ohsugi, R. Oishi, T. Okusawa, J. Olsen, W. Orejudos, C. Pagliarone, F. Palmonari, R. Paoletti, V. Papadimitriou, S. Pappas, D. Partos, J. Patrick, G. Pauletta, M. Paulini, C. Paus, L. Pescara, T. Phillips, G. Piacentino, K. Pitts, R. Plunkett, A. Pompos, L. Pondrom, G. Pope, M. Popovic, F. Prokoshin, J. Proudfoot, F. Ptohos, O. Pukhov, G. Punzi, K. Ragan, A. Rakitine, D. Reher, A. Reichold, W. Riegler, A. Ribon, F. Rimondi, L. Ristori, M. Riveline, W. Robertson, A. Robinson, T. Rodrigo, S. Rolli, L. Rosenson, R. Roser, R. Rossin, A. Safonov, W. Sakumoto, D. Saltzberg, A. Sansoni, L. Santi, H. Sato, P. Savard, P. Schlabach, E. Schmidt, M. Schmidt, M. Schmitt, L. Scodellaro, A. Scott, A. Scribano, S. Segler, S. Seidel, Y. Seiya, A. Semenov, F. Semeria, T. Shah, M. Shapiro, P. Shepard, T. Shibayama, M. Shimojima, M. Shochet, J. Siegrist, G. Signorelli, A. Sill, P. Sinervo, P. Singh, A. Slaughter, K. Sliwa, C. Smith, F. Snider, A. Solodsky, J. Spalding, T. Speer, P. Sphicas, F. Spinella, M. Spiropulu, L. Spiegel, J. Steele, A. Stefanini, J. Strologas, F. Strumia, D. Stuart, K. Sumorok, T. Suzuki, T. Takano, R. Takashima, K. Takikawa, P. Tamburello, M. Tanaka, B. Tannenbaum, W. Taylor, M. Tecchio, P. Teng, K. Terashi, S. Tether, D. Theriot, R. Thurman-Keup, P. Tipton, S. Tkaczyk, K. Tollefson, A. Tollestrup, H. Toyoda, W. Trischuk, J. de Troconiz, J. Tseng, N. Turini, F. Ukegawa, T. Vaiciulis, J. Valls, S. Vejcik, G. Velev, R. Vidal, R. Vilar, I. Volobouev, D. Vucinic, R. Wagner, R. Wagner, J. Wahl, N. Wallace, A. Walsh, C. Wang, C. Wang, M. Wang, T. Watanabe, D. Waters, T. Watts, R. Webb, H. Wenzel, W. Wester, A. Wicklund, E. Wicklund, H. Williams, P. Wilson, B. Winer, D. Winn, S. Wolbers, D. Wolinski, J. Wolinski, S. Wolinski, S. Worm, X. Wu, J. Wyss, A. Yagil, W. Yao, G. Yeh, P. Yeh, J. Yoh, C. Yosef, T. Yoshida, I. Yu, S. Yu, Z. Yu, A. Zanetti, F. Zetti, S. Zucchelli; CDF Collaboration, Measurement of the W boson mass with the Collider Detector at Fermilab. *Phys. Rev. D* **64**, 052001 (2001). doi:10.1103/PhysRevD.64.052001

29. B. Abbott, M. Abolins, B. S. Acharya, I. Adam, D. L. Adams, M. Adams, S. Ahn, H. Aihara, G. A. Alves, N. Amos, E. W. Anderson, R. Astur, M. M. Baarmand, A. Baden, V. Balamurali, J. Balderston, B. Baldin, S. Banerjee, J. Bantly, E. Barberis, J. F. Bartlett, K. Bazizi, A. Belyaev, S. B. Beri, I. Bertram, V. A. Bezzubov, P. C. Bhat, V. Bhatnagar, M. Bhattacharjee, N. Biswas, G. Blazey, S. Blessing, P. Bloom, A. Boehnlein, N. I. Bojko, F. Borcherding, C. Boswell, A. Brandt, R. Brock, A. Bross, D. Buchholz, V. S. Burtovoi, J. M. Butler, W. Carvalho, D. Casey, Z. Casilum, H. Castilla-Valdez, D. Chakraborty, S.-

M. Chang, S. V. Chekulaev, L.-P. Chen, W. Chen, S. Choi, S. Chopra, B. C. Choudhary, J. H. Christenson, M. Chung, D. Claes, A. R. Clark, W. G. Cobau, J. Cochran, L. Coney, W. E. Cooper, C. Cretsinger, D. Cullen-Vidal, M. A. C. Cummings, D. Cutts, O. I. Dahl, K. Davis, K. De, K. Del Signore, M. Demarteau, D. Denisov, S. P. Denisov, H. T. Diehl, M. Diesburg, G. Di Loreto, P. Draper, Y. Ducros, L. V. Dudko, S. R. Dugad, D. Edmunds, J. Ellison, V. D. Elvira, R. Engelmann, S. Eno, G. Eppley, P. Ermolov, O. V. Eroshin, V. N. Evdokimov, T. Fahland, M. K. Fatyga, S. Feher, D. Fein, T. Ferbel, G. Finocchiaro, H. E. Fisk, Y. Fisyak, E. Flattum, G. E. Forden, M. Fortner, K. C. Frame, S. Fuess, E. Gallas, A. N. Galyaev, P. Gartung, T. L. Geld, R. J. Genik, K. Genser, C. E. Gerber, B. Gibbard, S. Glenn, B. Gobbi, A. Goldschmidt, B. Gómez, G. Gómez, P. I. Goncharov, J. L. González Solís, H. Gordon, L. T. Goss, K. Gounder, A. Goussiou, N. Graf, P. D. Grannis, D. R. Green, H. Greenlee, G. Grim, S. Grinstein, N. Grossman, P. Grudberg, S. Grünendahl, G. Guglielmo, J. A. Guida, J. M. Guida, A. Gupta, S. N. Gurzhiev, P. Gutierrez, Y. E. Gutnikov, N. J. Hadley, H. Haggerty, S. Hagopian, V. Hagopian, K. S. Hahn, R. E. Hall, P. Hanlet, S. Hansen, J. M. Hauptman, D. Hedin, A. P. Heinson, U. Heintz, R. Hernández-Montoya, T. Heuring, R. Hirosky, J. D. Hobbs, B. Hoeneisen, J. S. Hoftun, F. Hsieh, T. Hu, T. Hu, T. Huehn, A. S. Ito, E. James, J. Jaques, S. A. Jerger, R. Jesik, J. Z.-Y. Jiang, T. Joffe-Minor, K. Johns, M. Johnson, A. Jonckheere, M. Jones, H. Jöstlein, S. Y. Jun, C. K. Jung, S. Kahn, G. Kalbfleisch, J. S. Kang, D. Karmanov, D. Karmgard, R. Kehoe, M. L. Kelly, C. L. Kim, S. K. Kim, A. Klatchko, B. Klima, C. Klopfenstein, V. I. Klyukhin, V. I. Kochetkov, J. M. Kohli, D. Koltick, A. V. Kostritskiy, J. Kotcher, A. V. Kotwal, J. Kourlas, A. V. Kozelov, E. A. Kozlovski, J. Krane, M. R. Krishnaswamy, S. Krzywdzinski, S. Kunori, S. Lami, R. Lander, F. Landry, G. Landsberg, B. Lauer, A. Leflat, H. Li, J. Li, Q. Z. Li-Demarteau, J. G. R. Lima, D. Lincoln, S. L. Linn, J. Linnemann, R. Lipton, Y. C. Liu, F. Lobkowicz, S. C. Loken, S. Lökös, L. Lueking, A. L. Lyon, A. K. A. Maciel, R. J. Madaras, R. Madden, L. Magaña-Mendoza, V. Manankov, S. Mani, H. S. Mao, R. Markeloff, T. Marshall, M. I. Martin, K. M. Mauritz, B. May, A. A. Mayorov, R. McCarthy, J. McDonald, T. McKibben, J. McKinley, T. McMahon, H. L. Melanson, M. Merkin, K. W. Merritt, H. Miettinen, A. Mincer, C. S. Mishra, N. Mokhov, N. K. Mondal, H. E. Montgomery, P. Mooney, H. da Motta, C. Murphy, F. Nang, M. Narain, V. S. Narasimham, A. Narayanan, H. A. Neal, J. P. Negret, P. Nemethy, D. Norman, L. Oesch, V. Oguri, E. Oliveira, E. Oltman, N. Oshima, D. Owen, P. Padley, A. Para, Y. M. Park, R. Partridge, N. Parua, M. Paterno, B. Pawlik, J. Perkins, M. Peters, R. Piegaia, H. Piekarz, Y. Pischalnikov, V. M. Podstavkov, B. G. Pope, H. B. Prosper, S. Protopopescu, J. Qian, P. Z. Quintas, R. Raja, S. Rajagopalan, O. Ramirez, L. Rasmussen, S. Reucroft, M. Rijssenbeek, T. Rockwell, M. Roco, N. A. Roe, P. Rubinov, R. Ruchti, J. Rutherfoord, A. Sánchez-Hernández, A. Santoro, L. Sawyer, R. D. Schamberger, H. Schellman, J. Sculli, E. Shabalina, C. Shaffer, H. C. Shankar, R. K. Shivpuri, M. Shupe, H. Singh, J. B. Singh, V. Sirotenko, W. Smart, E. Smith, R. P. Smith, R. Snihur, G. R. Snow, J. Snow, S. Snyder, J. Solomon, P. M. Sood, M. Sosebee, N. Sotnikova, M. Souza, A. L. Spadafora, G. Steinbrück, R. W. Stephens, M. L. Stevenson, D. Stewart, F. Stichelbaut, D. A. Stoianova, D. Stoker, M. Strauss, K. Streets, M. Strovink, A. Sznajder, P. Tamburello, J. Tarazi, M. Tartaglia, T. L. T. Thomas, J. Thompson, T. G. Trippe, P. M. Tuts, N. Varelas, E. W. Varnes, D. Vititoe, A. A. Volkov, A. P. Vorobiev, H. D. Wahl, G. Wang, J. Warchol, G. Watts, M. Wayne, H. Weerts, A. White, J. T. White, J. A. Wightman, S.

Willis, S. J. Wimpenny, J. V. D. Wirjawan, J. Womersley, E. Won, D. R. Wood, H. Xu, R. Yamada, P. Yamin, J. Yang, T. Yasuda, P. Yepes, C. Yoshikawa, S. Youssef, J. Yu, Y. Yu, Z. H. Zhu, D. Zieminska, A. Zieminski, E. G. Zverev, A. Zylberstejn; D0 Collaboration, Measurement of the *W* boson mass. *Phys. Rev. D* **58**, 092003 (1998). doi:10.1103/PhysRevD.58.092003

30. B. Abbott *et al*.; D0 Collaboration, Measurement of the W boson mass using electrons at large rapidities. *Phys. Rev. Lett.* **84**, 222–227 (2000). doi:10.1103/PhysRevLett.84.222 Medline

31. B. Abbott, M. Abolins, V. Abramov, B. S. Acharya, I. Adam, D. L. Adams, M. Adams, S. Ahn, V. Akimov, G. A. Alves, N. Amos, E. W. Anderson, M. M. Baarmand, V. V. Babintsev, L. Babukhadia, A. Baden, B. Baldin, S. Banerjee, J. Bantly, E. Barberis, P. Baringer, J. F. Bartlett, A. Belyaev, S. B. Beri, I. Bertram, V. A. Bezzubov, P. C. Bhat, V. Bhatnagar, M. Bhattacharjee, G. Blazey, S. Blessing, P. Bloom, A. Boehnlein, N. I. Bojko, F. Borcherding, C. Boswell, A. Brandt, R. Breedon, G. Briskin, R. Brock, A. Bross, D. Buchholz, V. S. Burtovoi, J. M. Butler, W. Carvalho, D. Casey, Z. Casilum, H. Castilla-Valdez, D. Chakraborty, K. M. Chan, S. V. Chekulaev, W. Chen, D. K. Cho, S. Choi, S. Chopra, B. C. Choudhary, J. H. Christenson, M. Chung, D. Claes, A. R. Clark, W. G. Cobau, J. Cochran, L. Coney, W. E. Cooper, D. Coppage, C. Cretsinger, D. Cullen-Vidal, M. A. C. Cummings, D. Cutts, O. I. Dahl, K. Davis, K. De, K. Del Signore, M. Demarteau, D. Denisov, S. P. Denisov, H. T. Diehl, M. Diesburg, G. Di Loreto, P. Draper, Y. Ducros, L. V. Dudko, S. R. Dugad, A. Dyshkant, D. Edmunds, J. Ellison, V. D. Elvira, R. Engelmann, S. Eno, G. Eppley, P. Ermolov, O. V. Eroshin, J. Estrada, H. Evans, V. N. Evdokimov, T. Fahland, M. K. Fatyga, S. Feher, D. Fein, T. Ferbel, H. E. Fisk, Y. Fisyak, E. Flattum, G. E. Forden, M. Fortner, K. C. Frame, S. Fuess, E. Gallas, A. N. Galyaev, P. Gartung, V. Gavrilov, T. L. Geld, R. J. Genik, K. Genser, C. E. Gerber, Y. Gershtein, B. Gibbard, G. Ginther, B. Gobbi, B. Gómez, G. Gómez, P. I. Goncharov, J. L. González Solís, H. Gordon, L. T. Goss, K. Gounder, A. Goussiou, N. Graf, P. D. Grannis, D. R. Green, J. A. Green, H. Greenlee, S. Grinstein, P. Grudberg, S. Grünendahl, G. Guglielmo, J. A. Guida, J. M. Guida, A. Gupta, S. N. Gurzhiev, G. Gutierrez, P. Gutierrez, N. J. Hadley, H. Haggerty, S. Hagopian, V. Hagopian, K. S. Hahn, R. E. Hall, P. Hanlet, S. Hansen, J. M. Hauptman, C. Hays, C. Hebert, D. Hedin, A. P. Heinson, U. Heintz, R. Hernández-Montoya, T. Heuring, R. Hirosky, J. D. Hobbs, B. Hoeneisen, J. S. Hoftun, F. Hsieh, T. Hu, A. S. Ito, S. A. Jerger, R. Jesik, T. Joffe-Minor, K. Johns, M. Johnson, A. Jonckheere, M. Jones, H. Jöstlein, S. Y. Jun, S. Kahn, D. Karmanov, D. Karmgard, R. Kehoe, S. K. Kim, B. Klima, C. Klopfenstein, B. Knuteson, W. Ko, J. M. Kohli, D. Koltick, A. V. Kostritskiy, J. Kotcher, A. V. Kotwal, A. V. Kozelov, E. A. Kozlovsky, J. Krane, M. R. Krishnaswamy, S. Krzywdzinski, M. Kubantsev, S. Kuleshov, Y. Kulik, S. Kunori, F. Landry, G. Landsberg, A. Leflat, J. Li, Q. Z. Li, J. G. R. Lima, D. Lincoln, S. L. Linn, J. Linnemann, R. Lipton, J. G. Lu, A. Lucotte, L. Lueking, A. K. A. Maciel, R. J. Madaras, R. Madden, L. Magaña-Mendoza, V. Manankov, S. Mani, H. S. Mao, R. Markeloff, T. Marshall, M. I. Martin, R. D. Martin, K. M. Mauritz, B. May, A. A. Mayorov, R. McCarthy, J. McDonald, T. McKibben, J. McKinley, T. McMahon, H. L. Melanson, M. Merkin, K. W. Merritt, C. Miao, H. Miettinen, A. Mincer, C. S. Mishra, N. Mokhov, N. K. Mondal, H. E. Montgomery, M. Mostafa, H. da Motta, F. Nang, M. Narain, V. S. Narasimham, A. Narayanan, H. A. Neal, J. P. Negret, P. Nemethy, D. Norman, L. Oesch, V. Oguri, N. Oshima, D. Owen, P.

Padley, A. Para, N. Parashar, Y. M. Park, R. Partridge, N. Parua, M. Paterno, B. Pawlik, J. Perkins, M. Peters, R. Piegaia, H. Piekarz, Y. Pischalnikov, B. G. Pope, H. B. Prosper, S. Protopopescu, J. Qian, P. Z. Quintas, S. Rajagopalan, O. Ramirez, N. W. Reay, S. Reucroft, M. Rijssenbeek, T. Rockwell, M. Roco, P. Rubinov, R. Ruchti, J. Rutherfoord, A. Sánchez-Hernández, A. Santoro, L. Sawyer, R. D. Schamberger, H. Schellman, J. Sculli, E. Shabalina, C. Shaffer, H. C. Shankar, R. K. Shivpuri, D. Shpakov, M. Shupe, R. A. Sidwell, H. Singh, J. B. Singh, V. Sirotenko, P. Slattery, E. Smith, R. P. Smith, R. Snihur, G. R. Snow, J. Snow, S. Snyder, J. Solomon, X. F. Song, M. Sosebee, N. Sotnikova, M. Souza, N. R. Stanton, G. Steinbrück, R. W. Stephens, M. L. Stevenson, F. Stichelbaut, D. Stoker, V. Stolin, D. A. Stoyanova, M. Strauss, K. Streets, M. Strovink, A. Sznajder, P. Tamburello, J. Tarazi, M. Tartaglia, T. L. T. Thomas, J. Thompson, D. Toback, T. G. Trippe, P. M. Tuts, V. Vaniev, N. Varelas, E. W. Varnes, A. A. Volkov, A. P. Vorobiev, H. D. Wahl, J. Warchol, G. Watts, M. Wayne, H. Weerts, A. White, J. T. White, J. A. Wightman, S. Willis, S. J. Wimpenny, J. V. D. Wirjawan, J. Womersley, D. R. Wood, R. Yamada, P. Yamin, T. Yasuda, P. Yepes, K. Yip, C. Yoshikawa, S. Youssef, J. Yu, Y. Yu, M. Zanabria, Z. Zhou, Z. H. Zhu, M. Zielinski, D. Zieminska, A. Zieminski, V. Zutshi, E. G. Zverev, A. Zylberstejn; D0 Collaboration, Measurement of the *W* boson mass using large rapidity electrons. *Phys. Rev. D* **62**, 092006 (2000). doi:10.1103/PhysRevD.62.092006

32. V. M. Abazov, B. Abbott, A. Abdesselam, M. Abolins, V. Abramov, B. S. Acharya, D. L. Adams, M. Adams, S. N. Ahmed, G. D. Alexeev, A. Alton, G. A. Alves, E. W. Anderson, Y. Arnoud, C. Avila, M. M. Baarmand, V. V. Babintsev, L. Babukhadia, T. C. Bacon, A. Baden, B. Baldin, P. W. Balm, S. Banerjee, E. Barberis, P. Baringer, J. Barreto, J. F. Bartlett, U. Bassler, D. Bauer, A. Bean, F. Beaudette, M. Begel, A. Belyaev, S. B. Beri, G. Bernardi, I. Bertram, A. Besson, R. Beuselinck, V. A. Bezzubov, P. C. Bhat, V. Bhatnagar, M. Bhattacharjee, G. Blazey, F. Blekman, S. Blessing, A. Boehnlein, N. I. Bojko, T. A. Bolton, F. Borcherding, K. Bos, T. Bose, A. Brandt, R. Breedon, G. Briskin, R. Brock, G. Brooijmans, A. Bross, D. Buchholz, M. Buehler, V. Buescher, V. S. Burtovoi, J. M. Butler, F. Canelli, W. Carvalho, D. Casey, Z. Casilum, H. Castilla-Valdez, D. Chakraborty, K. M. Chan, S. V. Chekulaev, D. K. Cho, S. Choi, S. Chopra, J. H. Christenson, M. Chung, D. Claes, A. R. Clark, L. Coney, B. Connolly, W. E. Cooper, D. Coppage, S. Crépé-Renaudin, M. A. C. Cummings, D. Cutts, G. A. Davis, K. De, S. J. de Jong, M. Demarteau, R. Demina, P. Demine, D. Denisov, S. P. Denisov, S. Desai, H. T. Diehl, M. Diesburg, S. Doulas, Y. Ducros, L. V. Dudko, S. Duensing, L. Duflot, S. R. Dugad, A. Duperrin, A. Dyshkant, D. Edmunds, J. Ellison, J. T. Eltzroth, V. D. Elvira, R. Engelmann, S. Eno, G. Eppley, P. Ermolov, O. V. Eroshin, J. Estrada, H. Evans, V. N. Evdokimov, T. Fahland, D. Fein, T. Ferbel, F. Filthaut, H. E. Fisk, Y. Fisyak, E. Flattum, F. Fleuret, M. Fortner, H. Fox, K. C. Frame, S. Fu, S. Fuess, E. Gallas, A. N. Galyaev, M. Gao, V. Gavrilov, R. J. Genik, K. Genser, C. E. Gerber, Y. Gershtein, R. Gilmartin, G. Ginther, B. Gómez, P. I. Goncharov, H. Gordon, L. T. Goss, K. Gounder, A. Goussiou, N. Graf, P. D. Grannis, J. A. Green, H. Greenlee, Z. D. Greenwood, S. Grinstein, L. Groer, S. Grünendahl, A. Gupta, S. N. Gurzhiev, G. Gutierrez, P. Gutierrez, N. J. Hadley, H. Haggerty, S. Hagopian, V. Hagopian, R. E. Hall, S. Hansen, J. M. Hauptman, C. Hays, C. Hebert, D. Hedin, J. M. Heinmiller, A. P. Heinson, U. Heintz, M. D. Hildreth, R. Hirosky, J. D. Hobbs, B. Hoeneisen, Y. Huang, I. Iashvili, R. Illingworth, A. S. Ito, M. Jaffré, S. Jain, R. Jesik, K. Johns, M. Johnson, A.

Jonckheere, H. Jöstlein, A. Juste, W. Kahl, S. Kahn, E. Kajfasz, A. M. Kalinin, D. Karmanov, D. Karmgard, R. Kehoe, A. Khanov, A. Kharchilava, S. K. Kim, B. Klima, B. Knuteson, W. Ko, J. M. Kohli, A. V. Kostritskiy, J. Kotcher, B. Kothari, A. V. Kotwal, A. V. Kozelov, E. A. Kozlovsky, J. Krane, M. R. Krishnaswamy, P. Krivkova, S. Krzywdzinski, M. Kubantsev, S. Kuleshov, Y. Kulik, S. Kunori, A. Kupco, V. E. Kuznetsov, G. Landsberg, W. M. Lee, A. Leflat, C. Leggett, F. Lehner, C. Leonidopoulos, J. Li, Q. Z. Li, J. G. R. Lima, D. Lincoln, S. L. Linn, J. Linnemann, R. Lipton, A. Lucotte, L. Lueking, C. Lundstedt, C. Luo, A. K. A. Maciel, R. J. Madaras, V. L. Malyshev, V. Manankov, H. S. Mao, T. Marshall, M. I. Martin, A. A. Mayorov, R. McCarthy, T. McMahon, H. L. Melanson, M. Merkin, K. W. Merritt, C. Miao, H. Miettinen, D. Mihalcea, C. S. Mishra, N. Mokhov, N. K. Mondal, H. E. Montgomery, R. W. Moore, M. Mostafa, H. da Motta, Y. Mutaf, E. Nagy, F. Nang, M. Narain, V. S. Narasimham, N. A. Naumann, H. A. Neal, J. P. Negret, A. Nomerotski, T. Nunnemann, D. O'Neil, V. Oguri, B. Olivier, N. Oshima, P. Padley, L. J. Pan, K. Papageorgiou, N. Parashar, R. Partridge, N. Parua, M. Paterno, A. Patwa, B. Pawlik, O. Peters, P. Pétroff, R. Piegaia, B. G. Pope, E. Popkov, H. B. Prosper, S. Protopopescu, M. B. Przybycien, J. Qian, R. Raja, S. Rajagopalan, E. Ramberg, P. A. Rapidis, N. W. Reay, S. Reucroft, M. Ridel, M. Rijssenbeek, F. Rizatdinova, T. Rockwell, M. Roco, C. Royon, P. Rubinov, R. Ruchti, J. Rutherfoord, B. M. Sabirov, G. Sajot, A. Santoro, L. Sawyer, R. D. Schamberger, H. Schellman, A. Schwartzman, N. Sen, E. Shabalina, R. K. Shivpuri, D. Shpakov, M. Shupe, R. A. Sidwell, V. Simak, H. Singh, V. Sirotenko, P. Slattery, E. Smith, R. P. Smith, R. Snihur, G. R. Snow, J. Snow, S. Snyder, J. Solomon, Y. Song, V. Sorín, M. Sosebee, N. Sotnikova, K. Soustruznik, M. Souza, N. R. Stanton, G. Steinbrück, R. W. Stephens, D. Stoker, V. Stolin, A. Stone, D. A. Stoyanova, M. A. Strang, M. Strauss, M. Strovink, L. Stutte, A. Sznajder, M. Talby, W. Taylor, S. Tentindo-Repond, S. M. Tripathi, T. G. Trippe, A. S. Turcot, P. M. Tuts, V. Vaniev, R. Van Kooten, N. Varelas, L. S. Vertogradov, F. Villeneuve-Seguier, A. A. Volkov, A. P. Vorobiev, H. D. Wahl, H. Wang, Z.-M. Wang, J. Warchol, G. Watts, M. Wayne, H. Weerts, A. White, J. T. White, D. Whiteson, D. A. Wijngaarden, S. Willis, S. J. Wimpenny, J. Womersley, D. R. Wood, Q. Xu, R. Yamada, P. Yamin, T. Yasuda, Y. A. Yatsunenko, K. Yip, S. Youssef, J. Yu, M. Zanabria, X. Zhang, H. Zheng, B. Zhou, Z. Zhou, M. Zielinski, D. Zieminska, A. Zieminski, V. Zutshi, E. G. Zverev, A. Zylberstejn; D0 Collaboration, Improved W boson mass measurement with the DØ detector. *Phys. Rev. D* **66**, 012001 (2002). doi:10.1103/PhysRevD.66.012001

33. V. M. Abazov *et al.*; CDF Collaboration, D0 Collaboration, Combination of CDF and D0 results on the *W* boson mass and width. *Phys. Rev. D* **70**, 092008 (2004). doi:10.1103/PhysRevD.70.092008

34. S. Schael, R. Barate, R. Brunelière, I. De Bonis, D. Decamp, C. Goy, S. Jézéquel, J.-P. Lees, F. Martin, E. Merle, M.-N. Minard, B. Pietrzyk, B. Trocmé, S. Bravo, M. P. Casado, M. Chmeissani, J. M. Crespo, E. Fernandez, M. Fernandez-Bosman, L. Garrido, M. Martinez, A. Pacheco, H. Ruiz, A. Colaleo, D. Creanza, N. De Filippis, M. de Palma, G. Iaselli, G. Maggi, M. Maggi, S. Nuzzo, A. Ranieri, G. Raso, F. Ruggieri, G. Selvaggi, L. Silvestris, P. Tempesta, A. Tricomi, G. Zito, X. Huang, J. Lin, Q. Ouyang, T. Wang, Y. Xie, R. Xu, S. Xue, J. Zhang, L. Zhang, W. Zhao, D. Abbaneo, T. Barklow, O. Buchmüller, M. Cattaneo, B. Clerbaux, H. Drevermann, R. W. Forty, M. Frank, F. Gianotti, J. B. Hansen, J. Harvey, D. E. Hutchcroft, P. Janot, B. Jost, M. Kado, P. Mato,

A. Moutoussi, F. Ranjard, L. Rolandi, D. Schlatter, F. Teubert, A. Valassi, I. Videau, F. Badaud, S. Dessagne, A. Falvard, D. Fayolle, P. Gay, J. Jousset, B. Michel, S. Monteil, D. Pallin, J. M. Pascolo, P. Perret, J. D. Hansen, J. R. Hansen, P. H. Hansen, A. C. Kraan, B. S. Nilsson, A. Kyriakis, C. Markou, E. Simopoulou, A. Vayaki, K. Zachariadou, A. Blondel, J.-C. Brient, F. Machefert, A. Rougé, H. Videau, V. Ciulli, E. Focardi, G. Parrini, A. Antonelli, M. Antonelli, G. Bencivenni, F. Bossi, G. Capon, F. Cerutti, V. Chiarella, P. Laurelli, G. Mannocchi, G. P. Murtas, L. Passalacqua, J. Kennedy, J. G. Lynch, P. Negus, V. O'Shea, A. S. Thompson, S. Wasserbaech, R. Cavanaugh, S. Dhamotharan, C. Geweniger, P. Hanke, V. Hepp, E. E. Kluge, A. Putzer, H. Stenzel, K. Tittel, M. Wunsch, R. Beuselinck, W. Cameron, G. Davies, P. J. Dornan, M. Girone, N. Marinelli, J. Nowell, S. A. Rutherford, J. K. Sedgbeer, J. C. Thompson, R. White, V. M. Ghete, P. Girtler, E. Kneringer, D. Kuhn, G. Rudolph, E. Bouhova-Thacker, C. K. Bowdery, D. P. Clarke, G. Ellis, A. J. Finch, F. Foster, G. Hughes, R. W. L. Jones, M. R. Pearson, N. A. Robertson, T. Sloan, M. Smizanska, O. van der Aa, C. Delaere, G. Leibenguth, V. Lemaitre, U. Blumenschein, F. Hölldorfer, K. Jakobs, F. Kayser, A.-S. Müller, B. Renk, H.-G. Sander, S. Schmeling, H. Wachsmuth, C. Zeitnitz, T. Ziegler, A. Bonissent, P. Coyle, C. Curtil, A. Ealet, D. Fouchez, P. Payre, A. Tilquin, F. Ragusa, A. David, H. Dietl, G. Ganis, K. Hüttmann, G. Lütjens, W. Männer, H.-G. Moser, R. Settles, M. Villegas, G. Wolf, J. Boucrot, O. Callot, M. Davier, L. Duflot, J.-F. Grivaz, P. Heusse, A. Jacholkowska, L. Serin, J.-J. Veillet, P. Azzurri, G. Bagliesi, T. Boccali, L. Foà, A. Giammanco, A. Giassi, F. Ligabue, A. Messineo, F. Palla, G. Sanguinetti, A. Sciabà, G. Sguazzoni, P. Spagnolo, R. Tenchini, A. Venturi, P. G. Verdini, O. Awunor, G. A. Blair, G. Cowan, A. Garcia-Bellido, M. G. Green, T. Medcalf, A. Misiejuk, J. A. Strong, P. Teixeira-Dias, R. W. Clifft, T. R. Edgecock, P. R. Norton, I. R. Tomalin, J. J. Ward, B. Bloch-Devaux, D. Boumediene, P. Colas, B. Fabbro, E. Lançon, M.-C. Lemaire, E. Locci, P. Perez, J. Rander, A. Trabelsi, B. Tuchming, B. Vallage, A. M. Litke, G. Taylor, C. N. Booth, S. Cartwright, F. Combley, P. N. Hodgson, M. Lehto, L. F. Thompson, A. Böhrer, S. Brandt, C. Grupen, J. Hess, A. Ngac, G. Prange, C. Borean, G. Giannini, H. He, J. Putz, J. Rothberg, S. R. Armstrong, K. Berkelman, K. Cranmer, D. P. S. Ferguson, Y. Gao, S. González, O. J. Hayes, H. Hu, S. Jin, J. Kile, P. A. McNamara III, J. Nielsen, Y. B. Pan, J. H. von Wimmersperg-Toeller, W. Wiedenmann, J. Wu, S. L. Wu, X. Wu, G. Zobernig, G. Dissertori; ALEPH Collaboration, Measurement of the W boson mass and width in e^+e^- collisions at LEP. *Eur. Phys. J. C* **47**, 309–335 (2006). doi:10.1140/epjc/s2006-02576-8

35. J. Abdallah, P. Abreu, W. Adam, P. Adzic, T. Albrecht, R. Alemany-Fernandez, T. Allmendinger, P. P. Allport, U. Amaldi, N. Amapane, S. Amato, E. Anashkin, A. Andreazza, S. Andringa, N. Anjos, P. Antilogus, W.-D. Apel, Y. Arnoud, S. Ask, B. Asman, J. E. Augustin, A. Augustinus, P. Baillon, A. Ballestrero, P. Bambade, R. Barbier, D. Bardin, G. J. Barker, A. Baroncelli, M. Battaglia, M. Baubillier, K.-H. Becks, M. Begalli, A. Behrmann, E. Ben-Haim, N. Benekos, A. Benvenuti, C. Berat, M. Berggren, D. Bertrand, M. Besancon, N. Besson, D. Bloch, M. Blom, M. Bluj, M. Bonesini, M. Boonekamp, P. S. L. Booth, G. Borisov, O. Botner, B. Bouquet, T. J. V. Bowcock, I. Boyko, M. Bracko, R. Brenner, E. Brodet, P. Bruckman, J. M. Brunet, B. Buschbeck, P. Buschmann, M. Calvi, T. Camporesi, V. Canale, F. Carena, N. Castro, F. Cavallo, M. Chapkin, P. Charpentier, P. Checchia, R. Chierici, P. Chliapnikov, J. Chudoba, S. U. Chung, K. Cieslik, P. Collins, R. Contri, G. Cosme, F. Cossutti, M. J.

Costa, D. Crennell, J. Cuevas, J. D'Hondt, T. da Silva, W. Da Silva, G. Della Ricca, A. De Angelis, W. De Boer, C. De Clercq, B. De Lotto, N. De Maria, A. De Min, L. de Paula, L. Di Ciaccio, A. Di Simone, K. Doroba, J. Drees, A. Duperrin, G. Eigen, T. Ekelof, M. Ellert, M. Elsing, M. C. Espirito Santo, G. Fanourakis, D. Fassouliotis, M. Feindt, J. Fernandez, A. Ferrer, F. Ferro, U. Flagmeyer, H. Foeth, E. Fokitis, F. Fulda-Quenzer, J. Fuster, M. Gandelman, C. Garcia, P. Gavillet, E. Gazis, R. Gokieli, B. Golob, G. Gomez-Ceballos, P. Goncalves, E. Graziani, G. Grosdidier, K. Grzelak, J. Guy, C. Haag, A. Hallgren, K. Hamacher, K. Hamilton, S. Haug, F. Hauler, V. Hedberg, M. Hennecke, J. Hoffman, S.-O. Holmgren, P. J. Holt, M. A. Houlden, J. N. Jackson, G. Jarlskog, P. Jarry, D. Jeans, E. K. Johansson, P. Jonsson, C. Joram, L. Jungermann, F. Kapusta, S. Katsanevas, E. Katsoufis, G. Kernel, B. P. Kersevan, U. Kerzel, B. T. King, N. J. Kjaer, P. Kluit, P. Kokkinias, C. Kourkoumelis, O. Kouznetsov, Z. Krumstein, M. Kucharczyk, J. Lamsa, G. Leder, F. Ledroit, L. Leinonen, R. Leitner, J. Lemonne, V. Lepeltier, T. Lesiak, W. Liebig, D. Liko, A. Lipniacka, J. H. Lopes, J. M. Lopez, D. Loukas, P. Lutz, L. Lyons, J. MacNaughton, A. Malek, S. Maltezos, F. Mandl, J. Marco, R. Marco, B. Marechal, M. Margoni, J.-C. Marin, C. Mariotti, A. Markou, C. Martinez-Rivero, J. Masik, N. Mastroyiannopoulos, F. Matorras, C. Matteuzzi, F. Mazzucato, M. Mazzucato, R. Mc Nulty, C. Meroni, E. Migliore, W. Mitaroff, U. Mjoernmark, T. Moa, M. Moch, K. Moenig, R. Monge, J. Montenegro, D. Moraes, S. Moreno, P. Morettini, U. Mueller, K. Muenich, M. Mulders, L. Mundim, W. Murray, B. Muryn, G. Myatt, T. Myklebust, M. Nassiakou, F. Navarria, K. Nawrocki, R. Nicolaidou, M. Nikolenko, A. Oblakowska-Mucha, V. Obraztsov, A. Olshevski, A. Onofre, R. Orava, K. Osterberg, A. Ouraou, A. Oyanguren, M. Paganoni, S. Paiano, J. P. Palacios, H. Palka, T. D. Papadopoulou, L. Pape, C. Parkes, F. Parodi, U. Parzefall, A. Passeri, O. Passon, L. Peralta, V. Perepelitsa, A. Perrotta, A. Petrolini, J. Piedra, L. Pieri, F. Pierre, M. Pimenta, E. Piotto, T. Podobnik, V. Poireau, M. E. Pol, G. Polok, V. Pozdniakov, N. Pukhaeva, A. Pullia, D. Radojicic, J. Rames, A. Read, P. Rebecchi, J. Rehn, D. Reid, R. Reinhardt, P. Renton, F. Richard, J. Ridky, M. Rivero, D. Rodriguez, A. Romero, P. Ronchese, P. Roudeau, T. Rovelli, V. Ruhlmann-Kleider, D. Ryabtchikov, A. Sadovsky, L. Salmi, J. Salt, C. Sander, A. Savoy-Navarro, U. Schwickerath, R. Sekulin, M. Siebel, L. Simard, A. Sisakian, G. Smadja, O. Smirnova, A. Sokolov, A. Sopczak, R. Sosnowski, T. Spassov, M. Stanitzki, A. Stocchi, J. Strauss, B. Stugu, M. Szczekowski, M. Szeptycka, T. Szumlak, T. Tabarelli, F. Tegenfeldt, J. Thomas, J. Timmermans, L. Tkatchev, M. Tobin, S. Todorovova, B. Tome, A. Tonazzo, P. Tortosa, P. Travnicek, D. Treille, G. Tristram, M. Trochimczuk, C. Troncon, M.-L. Turluer, I. A. Tyapkin, P. Tyapkin, S. Tzamarias, V. Uvarov, G. Valenti, P. Van Dam, J. Van Eldik, N. van Remortel, I. Van Vulpen, G. Vegni, F. Veloso, W. Venus, P. Verdier, V. Verzi, D. Vilanova, L. Vitale, V. Vrba, H. Wahlen, A. J. Washbrook, C. Weiser, D. Wicke, J. Wickens, G. Wilkinson, M. Winter, M. Witek, O. Yushchenko, A. Zalewska, P. Zalewski, D. Zavrtanik, V. Zhuravlov, N. I. Zimin, A. Zintchenko, M. Zupan; DELPHI Collaboration, Measurement of the mass and width of the W boson in e^+e^- collisions at $\sqrt{s} = 161 - 209$ GeV. *Eur. Phys. J. C* **55**, 1 (2008). doi:10.1140/epjc/s10052-008-0585-7

36. P. Achard *et al.*; L3 Collaboration, Measurement of the mass and the width of the W boson at LEP. *Eur. Phys. J. C* **45**, 569–587 (2006). doi:10.1140/epjc/s2005-02459-6

37. G. Abbiendi *et al*.; OPAL Collaboration, Measurement of the mass and width of the W boson. *Eur. Phys. J. C* **45**, 307–335 (2006). doi:10.1140/epjc/s2005-02440-5

38. T. Aaltonen, A. Abulencia, J. Adelman, T. Affolder, T. Akimoto, M. G. Albrow, S. Amerio, D. Amidei, A. Anastassov, K. Anikeev, A. Annovi, J. Antos, M. Aoki, G. Apollinari, T. Arisawa, A. Artikov, W. Ashmanskas, A. Attal, A. Aurisano, F. Azfar, P. Azzi-Bacchetta, P. Azzurri, N. Bacchetta, W. Badgett, A. Barbaro-Galtieri, V. E. Barnes, B. A. Barnett, S. Baroiant, V. Bartsch, G. Bauer, P.-H. Beauchemin, F. Bedeschi, S. Behari, G. Bellettini, J. Bellinger, A. Belloni, D. Benjamin, A. Beretvas, J. Beringer, T. Berry, A. Bhatti, M. Binkley, D. Bisello, I. Bizjak, R. E. Blair, C. Blocker, B. Blumenfeld, A. Bocci, A. Bodek, V. Boisvert, G. Bolla, A. Bolshov, D. Bortoletto, J. Boudreau, A. Boveia, B. Brau, L. Brigliadori, C. Bromberg, E. Brubaker, J. Budagov, H. S. Budd, S. Budd, K. Burkett, G. Busetto, P. Bussey, A. Buzatu, K. L. Byrum, S. Cabrera, M. Campanelli, M. Campbell, F. Canelli, A. Canepa, S. Carrillo, D. Carlsmith, R. Carosi, S. Carron, B. Casal, M. Casarsa, A. Castro, P. Catastini, D. Cauz, M. Cavalli-Sforza, A. Cerri, L. Cerrito, S. H. Chang, Y. C. Chen, M. Chertok, G. Chiarelli, G. Chlachidze, F. Chlebana, I. Cho, K. Cho, D. Chokheli, J. P. Chou, G. Choudalakis, S. H. Chuang, K. Chung, W. H. Chung, Y. S. Chung, M. Cilijak, C. I. Ciobanu, M. A. Ciocci, A. Clark, D. Clark, M. Coca, G. Compostella, M. E. Convery, J. Conway, B. Cooper, K. Copic, M. Cordelli, G. Cortiana, F. Crescioli, C. C. Almenar, J. Cuevas, R. Culbertson, J. C. Cully, S. Daronco, M. Datta, S. D'Auria, T. Davies, D. Dagenhart, P. de Barbaro, S. De Cecco, A. Deisher, G. De Lentdecker, G. De Lorenzo, M. Dell'orso, F. Delli Paoli, L. Demortier, J. Deng, M. Deninno, D. De Pedis, P. F. Derwent, G. P. Di Giovanni, C. Dionisi, B. Di Ruzza, J. R. Dittmann, M. D'Onofrio, C. Dörr, S. Donati, P. Dong, J. Donini, T. Dorigo, S. Dube, J. Efron, R. Erbacher, D. Errede, S. Errede, R. Eusebi, H. C. Fang, S. Farrington, I. Fedorko, W. T. Fedorko, R. G. Feild, M. Feindt, J. P. Fernandez, R. Field, G. Flanagan, R. Forrest, S. Forrester, M. Franklin, J. C. Freeman, I. Furic, M. Gallinaro, J. Galyardt, J. E. Garcia, F. Garberson, A. F. Garfinkel, C. Gay, H. Gerberich, D. Gerdes, S. Giagu, P. Giannetti, K. Gibson, J. L. Gimmell, C. Ginsburg, N. Giokaris, M. Giordani, P. Giromini, M. Giunta, G. Giurgiu, V. Glagolev, D. Glenzinski, M. Gold, N. Goldschmidt, J. Goldstein, A. Golossanov, G. Gomez, G. Gomez-Ceballos, M. Goncharov, O. González, I. Gorelov, A. T. Goshaw, K. Goulianos, A. Gresele, S. Grinstein, C. Grosso-Pilcher, U. Grundler, J. G. da Costa, Z. Gunay-Unalan, C. Haber, K. Hahn, S. R. Hahn, E. Halkiadakis, A. Hamilton, B. Y. Han, J. Y. Han, R. Handler, F. Happacher, K. Hara, D. Hare, M. Hare, S. Harper, R. F. Harr, R. M. Harris, M. Hartz, K. Hatakeyama, J. Hauser, C. Hays, M. Heck, A. Heijboer, B. Heinemann, J. Heinrich, C. Henderson, M. Herndon, J. Heuser, D. Hidas, C. S. Hill, D. Hirschbuehl, A. Hocker, A. Holloway, S. Hou, M. Houlden, S. C. Hsu, B. T. Huffman, R. E. Hughes, U. Husemann, J. Huston, J. Incandela, G. Introzzi, M. Iori, A. Ivanov, B. Iyutin, E. James, D. Jang, B. Jayatilaka, D. Jeans, E. J. Jeon, S. Jindariani, W. Johnson, M. Jones, K. K. Joo, S. Y. Jun, J. E. Jung, T. R. Junk, T. Kamon, P. E. Karchin, Y. Kato, Y. Kemp, R. Kephart, U. Kerzel, V. Khotilovich, B. Kilminster, D. H. Kim, H. S. Kim, J. E. Kim, M. J. Kim, S. B. Kim, S. H. Kim, Y. K. Kim, N. Kimura, L. Kirsch, S. Klimenko, M. Klute, B. Knuteson, B. R. Ko, K. Kondo, D. J. Kong, J. Konigsberg, A. Korytov, A. V. Kotwal, A. C. Kraan, J. Kraus, M. Kreps, J. Kroll, N. Krumnack, M. Kruse, V. Krutelyov, T. Kubo, S. E. Kuhlmann, T. Kuhr, N. P. Kulkarni, Y. Kusakabe, S. Kwang, A. T. Laasanen, S. Lai, S. Lami, S. Lammel, M. Lancaster, R. L. Lander, K. Lannon, A. Lath, G. Latino, I.

Lazzizzera, T. Lecompte, J. Lee, J. Lee, Y. J. Lee, S. W. Lee, R. Lefèvre, N. Leonardo, S. Leone, S. Levy, J. D. Lewis, C. Lin, C. S. Lin, M. Lindgren, E. Lipeles, T. M. Liss, A. Lister, D. O. Litvintsev, T. Liu, N. S. Lockyer, A. Loginov, M. Loreti, R. S. Lu, D. Lucchesi, P. Lujan, P. Lukens, G. Lungu, L. Lyons, J. Lys, R. Lysak, E. Lytken, P. Mack, D. Macqueen, R. Madrak, K. Maeshima, K. Makhoul, T. Maki, P. Maksimovic, S. Malde, S. Malik, G. Manca, A. Manousakis, F. Margaroli, R. Marginean, C. Marino, C. P. Marino, A. Martin, M. Martin, V. Martin, M. Martínez, R. Martínez-Ballarín, T. Maruyama, P. Mastrandrea, T. Masubuchi, H. Matsunaga, M. E. Mattson, R. Mazini, P. Mazzanti, K. S. McFarland, P. McIntyre, R. McNulty, A. Mehta, P. Mehtala, S. Menzemer, A. Menzione, P. Merkel, C. Mesropian, A. Messina, T. Miao, N. Miladinovic, J. Miles, R. Miller, C. Mills, M. Milnik, A. Mitra, G. Mitselmakher, A. Miyamoto, S. Moed, N. Moggi, B. Mohr, C. S. Moon, R. Moore, M. Morello, P. M. Fernandez, J. Mülmenstädt, A. Mukherjee, T. Muller, R. Mumford, P. Murat, M. Mussini, J. Nachtman, A. Nagano, J. Naganoma, K. Nakamura, I. Nakano, A. Napier, V. Necula, C. Neu, M. S. Neubauer, J. Nielsen, L. Nodulman, O. Norniella, E. Nurse, S. H. Oh, Y. D. Oh, I. Oksuzian, T. Okusawa, R. Oldeman, R. Orava, K. Osterberg, C. Pagliarone, E. Palencia, V. Papadimitriou, A. Papaikonomou, A. A. Paramonov, B. Parks, S. Pashapour, J. Patrick, G. Pauletta, M. Paulini, C. Paus, D. E. Pellett, A. Penzo, T. J. Phillips, G. Piacentino, J. Piedra, L. Pinera, K. Pitts, C. Plager, L. Pondrom, X. Portell, O. Poukhov, N. Pounder, F. Prakoshyn, A. Pronko, J. Proudfoot, F. Ptohos, G. Punzi, J. Pursley, J. Rademacker, A. Rahaman, V. Ramakrishnan, N. Ranjan, I. Redondo, B. Reisert, V. Rekovic, P. Renton, M. Rescigno, S. Richter, F. Rimondi, L. Ristori, A. Robson, T. Rodrigo, E. Rogers, S. Rolli, R. Roser, M. Rossi, R. Rossin, P. Roy, A. Ruiz, J. Russ, V. Rusu, H. Saarikko, A. Safonov, W. K. Sakumoto, G. Salamanna, O. Saltó, L. Santi, S. Sarkar, L. Sartori, K. Sato, P. Savard, A. Savoy-Navarro, T. Scheidle, P. Schlabach, E. E. Schmidt, M. P. Schmidt, M. Schmitt, T. Schwarz, L. Scodellaro, A. L. Scott, A. Scribano, F. Scuri, A. Sedov, S. Seidel, Y. Seiya, A. Semenov, L. Sexton-Kennedy, A. Sfyrla, S. Z. Shalhout, M. D. Shapiro, T. Shears, P. F. Shepard, D. Sherman, M. Shimojima, M. Shochet, Y. Shon, I. Shreyber, A. Sidoti, P. Sinervo, A. Sisakyan, A. J. Slaughter, J. Slaunwhite, K. Sliwa, J. R. Smith, F. D. Snider, R. Snihur, M. Soderberg, A. Soha, S. Somalwar, V. Sorin, J. Spalding, F. Spinella, T. Spreitzer, P. Squillacioti, M. Stanitzki, A. Staveris-Polykalas, R. S. Denis, B. Stelzer, O. Stelzer-Chilton, D. Stentz, J. Strologas, D. Stuart, J. S. Suh, A. Sukhanov, H. Sun, I. Suslov, T. Suzuki, A. Taffard, R. Takashima, Y. Takeuchi, R. Tanaka, M. Tecchio, P. K. Teng, K. Terashi, J. Thom, A. S. Thompson, E. Thomson, P. Tipton, V. Tiwari, S. Tkaczyk, D. Toback, S. Tokar, K. Tollefson, T. Tomura, D. Tonelli, S. Torre, D. Torretta, S. Tourneur, W. Trischuk, S. Tsuno, Y. Tu, N. Turini, F. Ukegawa, S. Uozumi, S. Vallecorsa, N. van Remortel, A. Varganov, E. Vataga, F. Vazquez, G. Velev, C. Vellidis, G. Veramendi, V. Veszpremi, M. Vidal, R. Vidal, I. Vila, R. Vilar, T. Vine, M. Vogel, I. Vollrath, I. Volobouev, G. Volpi, F. Würthwein, P. Wagner, R. G. Wagner, R. L. Wagner, J. Wagner, W. Wagner, R. Wallny, S. M. Wang, A. Warburton, D. Waters, M. Weinberger, W. C. Wester 3rd, B. Whitehouse, D. Whiteson, A. B. Wicklund, E. Wicklund, G. Williams, H. H. Williams, P. Wilson, B. L. Winer, P. Wittich, S. Wolbers, C. Wolfe, T. Wright, X. Wu, S. M. Wynne, A. Yagil, K. Yamamoto, J. Yamaoka, T. Yamashita, C. Yang, U. K. Yang, Y. C. Yang, W. M. Yao, G. P. Yeh, J. Yoh, K. Yorita, T. Yoshida, G. B. Yu, I. Yu, S. S. Yu, J. C. Yun, L. Zanello, A. Zanetti, I. Zaw, X. Zhang, J. Zhou, S. Zucchelli, S. Zucchelli;

CDF Collaboration, First measurement of the W-boson mass in run II of the Tevatron. *Phys. Rev. Lett.* **99**, 151801 (2007). doi:10.1103/PhysRevLett.99.151801 Medline

39. T. Aaltonen *et al*.; CDF Collaboration, First run II measurement of the *W* boson mass at the Fermilab Tevatron. *Phys. Rev. D* **77**, 112001 (2008). doi:10.1103/PhysRevD.77.112001

40. V. M. Abazov, B. Abbott, M. Abolins, B. S. Acharya, M. Adams, T. Adams, E. Aguilo, M. Ahsan, G. D. Alexeev, G. Alkhazov, A. Alton, G. Alverson, G. A. Alves, L. S. Ancu, T. Andeen, M. S. Anzelc, M. Aoki, Y. Arnoud, M. Arov, M. Arthaud, A. Askew, B. Åsman, O. Atramentov, C. Avila, J. Backusmayes, F. Badaud, L. Bagby, B. Baldin, D. V. Bandurin, S. Banerjee, E. Barberis, A.-F. Barfuss, P. Bargassa, P. Baringer, J. Barreto, J. F. Bartlett, U. Bassler, D. Bauer, S. Beale, A. Bean, M. Begalli, M. Begel, C. Belanger-Champagne, L. Bellantoni, A. Bellavance, J. A. Benitez, S. B. Beri, G. Bernardi, R. Bernhard, I. Bertram, M. Besançon, R. Beuselinck, V. A. Bezzubov, P. C. Bhat, V. Bhatnagar, G. Blazey, S. Blessing, K. Bloom, A. Boehnlein, D. Boline, T. A. Bolton, E. E. Boos, G. Borissov, T. Bose, A. Brandt, R. Brock, G. Brooijmans, A. Bross, D. Brown, X. B. Bu, D. Buchholz, M. Buehler, V. Buescher, V. Bunichev, S. Burdin, T. H. Burnett, C. P. Buszello, P. Calfayan, B. Calpas, S. Calvet, J. Cammin, M. A. Carrasco-Lizarraga, E. Carrera, W. Carvalho, B. C. K. Casey, H. Castilla-Valdez, S. Chakrabarti, D. Chakraborty, K. M. Chan, A. Chandra, E. Cheu, D. K. Cho, S. W. Cho, S. Choi, B. Choudhary, T. Christoudias, S. Cihangir, D. Claes, J. Clutter, M. Cooke, W. E. Cooper, M. Corcoran, F. Couderc, M.-C. Cousinou, D. Cutts, M. Ćwiok, A. Das, G. Davies, K. De, S. J. de Jong, E. De La Cruz-Burelo, K. Devaughan, F. Déliot, M. Demarteau, R. Demina, D. Denisov, S. P. Denisov, S. Desai, H. T. Diehl, M. Diesburg, A. Dominguez, T. Dorland, A. Dubey, L. V. Dudko, L. Duflot, D. Duggan, A. Duperrin, S. Dutt, A. Dyshkant, M. Eads, D. Edmunds, J. Ellison, V. D. Elvira, Y. Enari, S. Eno, M. Escalier, H. Evans, A. Evdokimov, V. N. Evdokimov, G. Facini, A. V. Ferapontov, T. Ferbel, F. Fiedler, F. Filthaut, W. Fisher, H. E. Fisk, M. Fortner, H. Fox, S. Fu, S. Fuess, T. Gadfort, C. F. Galea, A. Garcia-Bellido, V. Gavrilov, P. Gay, W. Geist, W. Geng, C. E. Gerber, Y. Gershtein, D. Gillberg, G. Ginther, B. Gómez, A. Goussiou, P. D. Grannis, S. Greder, H. Greenlee, Z. D. Greenwood, E. M. Gregores, G. Grenier, P. Gris, J.-F. Grivaz, A. Grohsjean, S. Grünendahl, M. W. Grünewald, F. Guo, J. Guo, G. Gutierrez, P. Gutierrez, A. Haas, P. Haefner, S. Hagopian, J. Haley, I. Hall, R. E. Hall, L. Han, K. Harder, A. Harel, J. M. Hauptman, J. Hays, T. Hebbeker, D. Hedin, J. G. Hegeman, A. P. Heinson, U. Heintz, C. Hensel, I. Heredia-De La Cruz, K. Herner, G. Hesketh, M. D. Hildreth, R. Hirosky, T. Hoang, J. D. Hobbs, B. Hoeneisen, M. Hohlfeld, S. Hossain, P. Houben, Y. Hu, Z. Hubacek, N. Huske, V. Hynek, I. Iashvili, R. Illingworth, A. S. Ito, S. Jabeen, M. Jaffré, S. Jain, K. Jakobs, D. Jamin, R. Jesik, K. Johns, C. Johnson, M. Johnson, D. Johnston, A. Jonckheere, P. Jonsson, A. Juste, E. Kajfasz, D. Karmanov, P. A. Kasper, I. Katsanos, V. Kaushik, R. Kehoe, S. Kermiche, N. Khalatyan, A. Khanov, A. Kharchilava, Y. N. Kharzheev, D. Khatidze, M. H. Kirby, M. Kirsch, B. Klima, J. M. Kohli, J.-P. Konrath, A. V. Kozelov, J. Kraus, T. Kuhl, A. Kumar, A. Kupco, T. Kurča, V. A. Kuzmin, J. Kvita, F. Lacroix, D. Lam, S. Lammers, G. Landsberg, P. Lebrun, H. S. Lee, W. M. Lee, A. Leflat, J. Lellouch, L. Li, Q. Z. Li, S. M. Lietti, J. K. Lim, D. Lincoln, J. Linnemann, V. V. Lipaev, R. Lipton, Y. Liu, Z. Liu, A. Lobodenko, M. Lokajicek, P. Love, H. J. Lubatti, R. Luna-Garcia, A. L. Lyon, A. K. A. Maciel, D. Mackin, P. Mättig, R. Magaña-Villalba, P. K. Mal, S. Malik, V. L. Malyshev, Y. Maravin, B. Martin, R. McCarthy, C. L. McGivern, M. M. Meijer, A. Melnitchouk, L.

Mendoza, D. Menezes, P. G. Mercadante, M. Merkin, K. W. Merritt, A. Meyer, J. Meyer, N. K. Mondal, H. E. Montgomery, R. W. Moore, T. Moulik, G. S. Muanza, M. Mulhearn, O. Mundal, L. Mundim, E. Nagy, M. Naimuddin, M. Narain, H. A. Neal, J. P. Negret, P. Neustroev, H. Nilsen, H. Nogima, S. F. Novaes, T. Nunnemann, G. Obrant, C. Ochando, D. Onoprienko, J. Orduna, N. Oshima, N. Osman, J. Osta, R. Otec, G. J. Otero Y Garzón, M. Owen, M. Padilla, P. Padley, M. Pangilinan, N. Parashar, S.-J. Park, S. K. Park, J. Parsons, R. Partridge, N. Parua, A. Patwa, B. Penning, M. Perfilov, K. Peters, Y. Peters, P. Pétroff, R. Piegaia, J. Piper, M.-A. Pleier, P. L. M. Podesta-Lerma, V. M. Podstavkov, Y. Pogorelov, M.-E. Pol, P. Polozov, A. V. Popov, M. Prewitt, S. Protopopescu, J. Qian, A. Quadt, B. Quinn, A. Rakitine, M. S. Rangel, K. Ranjan, P. N. Ratoff, P. Renkel, P. Rich, M. Rijssenbeek, I. Ripp-Baudot, F. Rizatdinova, S. Robinson, M. Rominsky, C. Royon, P. Rubinov, R. Ruchti, G. Safronov, G. Sajot, A. Sánchez-Hernández, M. P. Sanders, B. Sanghi, G. Savage, L. Sawyer, T. Scanlon, D. Schaile, R. D. Schamberger, Y. Scheglov, H. Schellman, T. Schliephake, S. Schlobohm, C. Schwanenberger, R. Schwienhorst, J. Sekaric, H. Severini, E. Shabalina, M. Shamim, V. Shary, A. A. Shchukin, R. K. Shivpuri, V. Siccardi, V. Simak, V. Sirotenko, P. Skubic, P. Slattery, D. Smirnov, G. R. Snow, J. Snow, S. Snyder, S. Söldner-Rembold, L. Sonnenschein, A. Sopczak, M. Sosebee, K. Soustruznik, B. Spurlock, J. Stark, V. Stolin, D. A. Stoyanova, J. Strandberg, M. A. Strang, E. Strauss, M. Strauss, R. Ströhmer, D. Strom, L. Stutte, S. Sumowidagdo, P. Svoisky, M. Takahashi, A. Tanasijczuk, W. Taylor, B. Tiller, M. Titov, V. V. Tokmenin, I. Torchiani, D. Tsybychev, B. Tuchming, C. Tully, P. M. Tuts, R. Unalan, L. Uvarov, S. Uvarov, S. Uzunyan, P. J. van den Berg, R. Van Kooten, W. M. van Leeuwen, N. Varelas, E. W. Varnes, I. A. Vasilyev, P. Verdier, L. S. Vertogradov, M. Verzocchi, M. Vesterinen, D. Vilanova, P. Vint, P. Vokac, R. Wagner, H. D. Wahl, M. H. L. S. Wang, J. Warchol, G. Watts, M. Wayne, G. Weber, M. Weber, L. Welty-Rieger, A. Wenger, M. Wetstein, A. White, D. Wicke, M. R. J. Williams, G. W. Wilson, S. J. Wimpenny, M. Wobisch, D. R. Wood, T. R. Wyatt, Y. Xie, C. Xu, S. Yacoob, R. Yamada, W.-C. Yang, T. Yasuda, Y. A. Yatsunenko, Z. Ye, H. Yin, K. Yip, H. D. Yoo, S. W. Youn, J. Yu, C. Zeitnitz, S. Zelitch, T. Zhao, B. Zhou, J. Zhu, M. Zielinski, D. Zieminska, L. Zivkovic, V. Zutshi, E. G. Zverev; D0 Collaboration, Measurement of the W boson mass. *Phys. Rev. Lett.* **103**, 141801 (2009). doi:10.1103/PhysRevLett.103.141801 Medline

41. T. Aaltonen, B. Álvarez González, S. Amerio, D. Amidei, A. Anastassov, A. Annovi, J. Antos, G. Apollinari, J. A. Appel, T. Arisawa, A. Artikov, J. Asaadi, W. Ashmanskas, B. Auerbach, A. Aurisano, F. Azfar, W. Badgett, T. Bae, A. Barbaro-Galtieri, V. E. Barnes, B. A. Barnett, P. Barria, P. Bartos, M. Bauce, F. Bedeschi, D. Beecher, S. Behari, G. Bellettini, J. Bellinger, D. Benjamin, A. Beretvas, A. Bhatti, M. Binkley, D. Bisello, I. Bizjak, K. R. Bland, B. Blumenfeld, A. Bocci, A. Bodek, D. Bortoletto, J. Boudreau, A. Boveia, L. Brigliadori, C. Bromberg, E. Brucken, J. Budagov, H. S. Budd, K. Burkett, G. Busetto, P. Bussey, A. Buzatu, A. Calamba, C. Calancha, S. Camarda, M. Campanelli, M. Campbell, F. Canelli, B. Carls, D. Carlsmith, R. Carosi, S. Carrillo, S. Carron, B. Casal, M. Casarsa, A. Castro, P. Catastini, D. Cauz, V. Cavaliere, M. Cavalli-Sforza, A. Cerri, L. Cerrito, Y. C. Chen, M. Chertok, G. Chiarelli, G. Chlachidze, F. Chlebana, K. Cho, D. Chokheli, W. H. Chung, Y. S. Chung, M. A. Ciocci, A. Clark, C. Clarke, G. Compostella, M. E. Convery, J. Conway, M. Corbo, M. Cordelli, C. A. Cox, D. J. Cox, F. Crescioli, J. Cuevas, R. Culbertson, D. Dagenhart, N. d'Ascenzo, M. Datta, P. de

Barbaro, M. Dell'Orso, L. Demortier, M. Deninno, F. Devoto, M. d'Errico, A. Di Canto, B. Di Ruzza, J. R. Dittmann, M. D'Onofrio, S. Donati, P. Dong, M. Dorigo, T. Dorigo, K. Ebina, A. Elagin, A. Eppig, R. Erbacher, S. Errede, N. Ershaidat, R. Eusebi, S. Farrington, M. Feindt, J. P. Fernandez, R. Field, G. Flanagan, R. Forrest, M. J. Frank, M. Franklin, J. C. Freeman, Y. Funakoshi, I. Furic, M. Gallinaro, J. E. Garcia, A. F. Garfinkel, P. Garosi, H. Gerberich, E. Gerchtein, S. Giagu, V. Giakoumopoulou, P. Giannetti, K. Gibson, C. M. Ginsburg, N. Giokaris, P. Giromini, G. Giurgiu, V. Glagolev, D. Glenzinski, M. Gold, D. Goldin, N. Goldschmidt, A. Golossanov, G. Gomez, G. Gomez-Ceballos, M. Goncharov, O. González, I. Gorelov, A. T. Goshaw, K. Goulianos, S. Grinstein, C. Grosso-Pilcher, R. C. Group, J. Guimaraes da Costa, S. R. Hahn, E. Halkiadakis, A. Hamaguchi, J. Y. Han, F. Happacher, K. Hara, D. Hare, M. Hare, R. F. Harr, K. Hatakeyama, C. Hays, M. Heck, J. Heinrich, M. Herndon, S. Hewamanage, A. Hocker, W. Hopkins, D. Horn, S. Hou, R. E. Hughes, M. Hurwitz, U. Husemann, N. Hussain, M. Hussein, J. Huston, G. Introzzi, M. Iori, A. Ivanov, E. James, D. Jang, B. Jayatilaka, E. J. Jeon, S. Jindariani, M. Jones, K. K. Joo, S. Y. Jun, T. R. Junk, T. Kamon, P. E. Karchin, A. Kasmi, Y. Kato, W. Ketchum, J. Keung, V. Khotilovich, B. Kilminster, D. H. Kim, H. S. Kim, J. E. Kim, M. J. Kim, S. B. Kim, S. H. Kim, Y. K. Kim, Y. J. Kim, N. Kimura, M. Kirby, S. Klimenko, K. Knoepfel, K. Kondo, D. J. Kong, J. Konigsberg, A. V. Kotwal, M. Kreps, J. Kroll, D. Krop, M. Kruse, V. Krutelyov, T. Kuhr, M. Kurata, S. Kwang, A. T. Laasanen, S. Lami, S. Lammel, M. Lancaster, R. L. Lander, K. Lannon, A. Lath, G. Latino, T. LeCompte, E. Lee, H. S. Lee, J. S. Lee, S. W. Lee, S. Leo, S. Leone, J. D. Lewis, A. Limosani, C.-J. Lin, M. Lindgren, E. Lipeles, A. Lister, D. O. Litvintsev, C. Liu, H. Liu, Q. Liu, T. Liu, S. Lockwitz, A. Loginov, D. Lucchesi, J. Lueck, P. Lujan, P. Lukens, G. Lungu, J. Lys, R. Lysak, R. Madrak, K. Maeshima, P. Maestro, S. Malik, G. Manca, A. Manousakis-Katsikakis, F. Margaroli, C. Marino, M. Martínez, P. Mastrandrea, K. Matera, M. E. Mattson, A. Mazzacane, P. Mazzanti, K. S. McFarland, P. McIntyre, R. McNulty, A. Mehta, P. Mehtala, C. Mesropian, T. Miao, D. Mietlicki, A. Mitra, H. Miyake, S. Moed, N. Moggi, M. N. Mondragon, C. S. Moon, R. Moore, M. J. Morello, J. Morlock, P. Movilla Fernandez, A. Mukherjee, T. Muller, P. Murat, M. Mussini, J. Nachtman, Y. Nagai, J. Naganoma, I. Nakano, A. Napier, J. Nett, C. Neu, M. S. Neubauer, J. Nielsen, L. Nodulman, S. Y. Noh, O. Norniella, E. Nurse, L. Oakes, S. H. Oh, Y. D. Oh, I. Oksuzian, T. Okusawa, R. Orava, L. Ortolan, S. Pagan Griso, C. Pagliarone, E. Palencia, V. Papadimitriou, A. A. Paramonov, J. Patrick, G. Pauletta, M. Paulini, C. Paus, D. E. Pellett, A. Penzo, T. J. Phillips, G. Piacentino, E. Pianori, J. Pilot, K. Pitts, C. Plager, L. Pondrom, S. Poprocki, K. Potamianos, F. Prokoshin, A. Pranko, F. Ptohos, G. Punzi, A. Rahaman, V. Ramakrishnan, N. Ranjan, I. Redondo, P. Renton, M. Rescigno, T. Riddick, F. Rimondi, L. Ristori, A. Robson, T. Rodrigo, T. Rodriguez, E. Rogers, S. Rolli, R. Roser, F. Ruffini, A. Ruiz, J. Russ, V. Rusu, A. Safonov, W. K. Sakumoto, Y. Sakurai, L. Santi, K. Sato, V. Saveliev, A. Savoy-Navarro, P. Schlabach, A. Schmidt, E. E. Schmidt, T. Schwarz, L. Scodellaro, A. Scribano, F. Scuri, S. Seidel, Y. Seiya, A. Semenov, F. Sforza, S. Z. Shalhout, T. Shears, R. Shekhar, P. F. Shepard, M. Shimojima, M. Shochet, I. Shreyber-Tecker, A. Simonenko, P. Sinervo, K. Sliwa, J. R. Smith, F. D. Snider, A. Soha, V. Sorin, H. Song, P. Squillacioti, M. Stancari, R. St Denis, B. Stelzer, O. Stelzer-Chilton, D. Stentz, J. Strologas, G. L. Strycker, Y. Sudo, A. Sukhanov, S. Sun, I. Suslov, K. Takemasa, Y. Takeuchi, J. Tang, M. Tecchio, P. K. Teng, J. Thom, J. Thome, D. S.

Thompson, G. A. Thompson, E. Thomson, D. Toback, S. Tokar, K. Tollefson, T. Tomura, D. Tonelli, S. Torre, D. Torretta, P. Totaro, M. Trovato, F. Ukegawa, S. Uozumi, A. Varganov, F. Vázquez, G. Velev, C. Vellidis, M. Vidal, I. Vila, R. Vilar, J. Vizán, M. Vogel, G. Volpi, P. Wagner, R. L. Wagner, T. Wakisaka, R. Wallny, S. M. Wang, A. Warburton, D. Waters, W. C. Wester 3rd, D. Whiteson, A. B. Wicklund, E. Wicklund, S. Wilbur, F. Wick, H. H. Williams, J. S. Wilson, P. Wilson, B. L. Winer, P. Wittich, S. Wolbers, H. Wolfe, T. Wright, X. Wu, Z. Wu, K. Yamamoto, D. Yamato, T. Yang, U. K. Yang, Y. C. Yang, W.-M. Yao, G. P. Yeh, K. Yi, J. Yoh, K. Yorita, T. Yoshida, G. B. Yu, I. Yu, S. S. Yu, J. C. Yun, A. Zanetti, Y. Zeng, C. Zhou, S. Zucchelli; CDF Collaboration, Precise measurement of the W-boson mass with the CDF II detector. *Phys. Rev. Lett.* **108**, 151803 (2012). doi:10.1103/PhysRevLett.108.151803 Medline

42. V. M. Abazov, B. Abbott, B. S. Acharya, M. Adams, T. Adams, G. D. Alexeev, G. Alkhazov, A. Alton, G. Alverson, M. Aoki, A. Askew, B. Åsman, S. Atkins, O. Atramentov, K. Augsten, C. Avila, F. Badaud, L. Bagby, B. Baldin, D. V. Bandurin, S. Banerjee, E. Barberis, P. Baringer, J. Barreto, J. F. Bartlett, U. Bassler, V. Bazterra, A. Bean, M. Begalli, C. Belanger-Champagne, L. Bellantoni, S. B. Beri, G. Bernardi, R. Bernhard, I. Bertram, M. Besançon, R. Beuselinck, V. A. Bezzubov, P. C. Bhat, S. Bhatia, V. Bhatnagar, G. Blazey, S. Blessing, K. Bloom, A. Boehnlein, D. Boline, E. E. Boos, G. Borissov, T. Bose, A. Brandt, O. Brandt, R. Brock, G. Brooijmans, A. Bross, D. Brown, J. Brown, X. B. Bu, M. Buehler, V. Buescher, V. Bunichev, S. Burdin, C. P. Buszello, E. Camacho-Pérez, B. C. K. Casey, H. Castilla-Valdez, S. Caughron, S. Chakrabarti, D. Chakraborty, K. M. Chan, A. Chandra, E. Chapon, G. Chen, S. Chevalier-Théry, D. K. Cho, S. W. Cho, S. Choi, B. Choudhary, S. Cihangir, D. Claes, J. Clutter, M. Cooke, W. E. Cooper, M. Corcoran, F. Couderc, M.-C. Cousinou, A. Croc, D. Cutts, A. Das, G. Davies, S. J. de Jong, E. De la Cruz-Burelo, F. Déliot, R. Demina, D. Denisov, S. P. Denisov, S. Desai, C. Deterre, K. DeVaughan, H. T. Diehl, M. Diesburg, P. F. Ding, A. Dominguez, T. Dorland, A. Dubey, L. V. Dudko, D. Duggan, A. Duperrin, S. Dutt, A. Dyshkant, M. Eads, D. Edmunds, J. Ellison, V. D. Elvira, Y. Enari, H. Evans, A. Evdokimov, V. N. Evdokimov, G. Facini, L. Feng, T. Ferbel, F. Fiedler, F. Filthaut, W. Fisher, H. E. Fisk, M. Fortner, H. Fox, S. Fuess, A. Garcia-Bellido, G. A. García-Guerra, V. Gavrilov, P. Gay, W. Geng, D. Gerbaudo, C. E. Gerber, Y. Gershtein, G. Ginther, G. Golovanov, A. Goussiou, P. D. Grannis, S. Greder, H. Greenlee, G. Grenier, P. Gris, J.-F. Grivaz, A. Grohsjean, S. Grünendahl, M. W. Grünewald, T. Guillemin, G. Gutierrez, P. Gutierrez, A. Haas, S. Hagopian, J. Haley, L. Han, K. Harder, A. Harel, J. M. Hauptman, J. Hays, T. Head, T. Hebbeker, D. Hedin, H. Hegab, A. P. Heinson, U. Heintz, C. Hensel, I. Heredia-De la Cruz, K. Herner, G. Hesketh, M. D. Hildreth, R. Hirosky, T. Hoang, J. D. Hobbs, B. Hoeneisen, M. Hohlfeld, I. Howley, Z. Hubacek, V. Hynek, I. Iashvili, Y. Ilchenko, R. Illingworth, A. S. Ito, S. Jabeen, M. Jaffré, A. Jayasinghe, R. Jesik, K. Johns, E. Johnson, M. Johnson, A. Jonckheere, P. Jonsson, J. Joshi, A. W. Jung, A. Juste, K. Kaadze, E. Kajfasz, D. Karmanov, P. A. Kasper, I. Katsanos, R. Kehoe, S. Kermiche, N. Khalatyan, A. Khanov, A. Kharchilava, Y. N. Kharzheev, J. M. Kohli, A. V. Kozelov, J. Kraus, S. Kulikov, A. Kumar, A. Kupco, T. Kurča, V. A. Kuzmin, S. Lammers, G. Landsberg, P. Lebrun, H. S. Lee, S. W. Lee, W. M. Lee, J. Lellouch, H. Li, L. Li, Q. Z. Li, J. K. Lim, D. Lincoln, J. Linnemann, V. V. Lipaev, R. Lipton, H. Liu, Y. Liu, A. Lobodenko, M. Lokajicek, R. Lopes de Sa, H. J. Lubatti, R. Luna-Garcia, A. L. Lyon, A. K. A. Maciel, R. Madar, R. Magaña-Villalba, S.

Malik, V. L. Malyshev, Y. Maravin, J. Martínez-Ortega, R. McCarthy, C. L. McGivern, M. M. Meijer, A. Melnitchouk, D. Menezes, P. G. Mercadante, M. Merkin, A. Meyer, J. Meyer, F. Miconi, N. K. Mondal, H. E. Montgomery, M. Mulhearn, E. Nagy, M. Naimuddin, M. Narain, R. Nayyar, H. A. Neal, J. P. Negret, P. Neustroev, T. Nunnemann, G. Obrant, J. Orduna, N. Osman, J. Osta, M. Padilla, A. Pal, N. Parashar, V. Parihar, S. K. Park, R. Partridge, N. Parua, A. Patwa, B. Penning, M. Perfilov, Y. Peters, K. Petridis, G. Petrillo, P. Pétroff, M.-A. Pleier, P. L. M. Podesta-Lerma, V. M. Podstavkov, P. Polozov, A. V. Popov, M. Prewitt, D. Price, N. Prokopenko, J. Qian, A. Quadt, B. Quinn, M. S. Rangel, K. Ranjan, P. N. Ratoff, I. Razumov, P. Renkel, I. Ripp-Baudot, F. Rizatdinova, M. Rominsky, A. Ross, C. Royon, P. Rubinov, R. Ruchti, G. Safronov, G. Sajot, P. Salcido, A. Sánchez-Hernández, M. P. Sanders, B. Sanghi, A. S. Santos, G. Savage, L. Sawyer, T. Scanlon, R. D. Schamberger, Y. Scheglov, H. Schellman, S. Schlobohm, C. Schwanenberger, R. Schwienhorst, J. Sekaric, H. Severini, E. Shabalina, V. Shary, S. Shaw, A. A. Shchukin, R. K. Shivpuri, V. Simak, P. Skubic, P. Slattery, D. Smirnov, K. J. Smith, G. R. Snow, J. Snow, S. Snyder, S. Söldner-Rembold, L. Sonnenschein, K. Soustruznik, J. Stark, V. Stolin, D. A. Stoyanova, M. Strauss, L. Stutte, L. Suter, P. Svoisky, M. Takahashi, M. Titov, V. V. Tokmenin, Y.-T. Tsai, K. Tschann-Grimm, D. Tsybychev, B. Tuchming, C. Tully, L. Uvarov, S. Uvarov, S. Uzunyan, R. Van Kooten, W. M. van Leeuwen, N. Varelas, E. W. Varnes, I. A. Vasilyev, P. Verdier, A. Y. Verkheev, L. S. Vertogradov, M. Verzocchi, M. Vesterinen, D. Vilanova, P. Vokac, H. D. Wahl, M. H. L. S. Wang, J. Warchol, G. Watts, M. Wayne, J. Weichert, L. Welty-Rieger, A. White, D. Wicke, M. R. J. Williams, G. W. Wilson, M. Wobisch, D. R. Wood, T. R. Wyatt, Y. Xie, S. Yacoob, R. Yamada, W.-C. Yang, T. Yasuda, Y. A. Yatsunenko, W. Ye, Z. Ye, H. Yin, K. Yip, S. W. Youn, T. Zhao, T. G. Zhao, B. Zhou, J. Zhu, M. Zielinski, D. Zieminska, L. Zivkovic; D0 Collaboration, Measurement of the W boson mass with the D0 detector. *Phys. Rev. Lett.* **108**, 151804 (2012). doi:10.1103/PhysRevLett.108.151804 Medline

43. T. Aaltonen *et al*.; CDF Collaboration, Precise measurement of the *W*-boson mass with the Collider Detector at Fermilab. *Phys. Rev. D* **89**, 072003 (2014). doi:10.1103/PhysRevD.89.072003

44. ALEPH Collaboration, CDF Collaboration, D0 Collaboration, DELPHI Collaboration, L3 Collaboration, OPAL Collaboration, SLD Collaboration, LEP Electroweak Working Group, Tevatron Electroweak Working Group, SLD electroweak heavy flavour groups, Precision electroweak measurements and constraints on the standard model. arXiv:1012.2367 [hep-ex] (2010) and references therein.

45. T. Aaltonen *et al*.; CDF Collaboration, D0 Collaboration, Combination of CDF and D0 *W*-boson mass measurements. *Phys. Rev. D* **88**, 052018 (2013). doi:10.1103/PhysRevD.88.052018

46. M. Aaboud *et al*.; ATLAS Collaboration, Measurement of the *W*-boson mass in pp collisions at $\sqrt{s} = 7$ TeV with the ATLAS detector. *Eur. Phys. J. C* **78**, 110 (2018). doi:10.1140/epjc/s10052-017-5475-4 Medline

47. M. Aaboud *et al.*; ATLAS Collaboration, Erratum to: Measurement of the *W*-boson mass in pp collisions at $\sqrt{s} = 7$ TeV with the ATLAS detector. *Eur. Phys. J. C* **78**, 898 (2018). doi:10.1140/epjc/s10052-018-6354-3

48. T. Affolder, D. Allspach, D. Ambrose, J. Bialek, W. Bokhari, M. Brozovic, M. Binkley, K. Burkett, A. Byon-Wagner, F. Cogswell, N. Dressnandt, Z. Feng, M. Franklin, L. Galtieri, D. W. Gerdes, J. Greenwood, V. Guarino, J. Guimaraes da Costa, R. Haggerty, C. Hall, J. Heinrich, A. Holloway, T. Jacobi, K. Kephart, D. Khazins, Y. K. Kim, M. Kirby, W. Kononenko, A. V. Kotwal, J. Kraus, T. M. Liss, N. Lockyer, R. Madrak, T. Miao, A. Mukherjee, C. Neu, M. Newcomer, J. M. Niczyporuk, L. Nodulman, W. Orejudous, T. J. Phillips, K. T. Pitts, W. Reigler, R. Richards, C. Rivetta, W. J. Robertson, R. Roser, L. Sadler, R. Sandberg, S. Sansone, R. Schmitt, K. Schultz, D. Shuman, R. Silva, P. Singh, R. Snihur, P. Tamburello, J. Taylor, R. Thurman-Keup, D. Tousignant, F. Ukegawa, R. Van Berg, G. Veramendi, T. Vickey, J. Wacker, R. L. Wagner, R. Weidenbach, W. C. Wester III, H. H. Williams, P. Wilson, P. Wittich, A. Yagil, I. Yu, S. Yu, J. C. Yun, CDF Central Outer Tracker. *Nucl. Instrum. Methods Phys. Res. A* **526**, 249–299 (2004). doi:10.1016/j.nima.2004.02.020

49. G. Ascoli, L. E. Holloway, I. Karliner, U. E. Kruse, R. D. Sard, V. J. Simaitis, D. A. Smith, T. K. Westhusing, CDF central muon detector. *Nucl. Instrum. Methods Phys. Res. A* **268**, 33–40 (1988). doi:10.1016/0168-9002(88)90590-6

50. The CDF II detector is centered on the beam (z) axis, which points in the proton direction. The $+x$ axis points outward and the $+y$ axis points upward, respectively, from the Tevatron ring. Corresponding cylindrical coordinates are defined with $r \equiv \sqrt{x^2 + y^2}$ and azimuthal angle $\phi \equiv \tan^{-1}(y/x)$. Pseudorapidity is defined as $\eta = -\ln[\tan(\theta/2)]$, where θ is the polar angle from the z axis. Energy (momentum) transverse to the beam is denoted as E_T (p_T).

51. A. V. Kotwal, H. K. Gerberich, C. Hays, Identification of cosmic rays using drift chamber hit timing. *Nucl. Instrum. Methods Phys. Res. A* **506**, 110–118 (2003). doi:10.1016/S0168-9002(03)01371-8

52. F. Abe *et al.*; CDF Collaboration, The CDF detector: An overview. *Nucl. Instrum. Methods Phys. Res. A* **271**, 387 (1988). doi:10.1016/0168-9002(88)90298-7

53. J. Smith, W. L. van Neerven, J. A. M. Vermaseren, Transverse Mass and Width of the W Boson. *Phys. Rev. Lett.* **50**, 1738–1740 (1983). doi:10.1103/PhysRevLett.50.1738

54. C. Balázs, C.-P. Yuan, Soft gluon effects on lepton pairs at hadron colliders. *Phys. Rev. D* **56**, 5558–5583 (1997). doi:10.1103/PhysRevD.56.5558

55. G. A. Ladinsky, C. Yuan, Nonperturbative regime in QCD resummation for gauge boson production at hadron colliders. *Phys. Rev. D* **50**, R4239–R4243 (1994). doi:10.1103/PhysRevD.50.R4239 Medline

56. F. Landry, R. Brock, P. M. Nadolsky, C.-P. Yuan, Fermilab Tevatron run-1 *Z* boson data and the Collins-Soper-Sterman resummation formalism. *Phys. Rev. D* **67**, 073016 (2003). doi:10.1103/PhysRevD.67.073016

57. P. Golonka, Z. Was, PHOTOS Monte Carlo: A precision tool for QED correctionsin Z and W decays. *Eur. Phys. J. C* **45**, 97–107 (2006). doi:10.1140/epjc/s2005-02396-4

58. C. M. Carloni Calame, G. Montagna, O. Nicrosini, A. Vicini, Precision electroweak calculation of the production of a high transverse-momentum lepton pair at hadron colliders. *J. High Energy Phys.* **2007**, 109 (2007). doi:10.1088/1126-6708/2007/10/109

59. A. V. Kotwal, B. Jayatilaka, Comparison of horace and photos Algorithms for Multiphoton Emission in the Context of W Boson Mass Measurement. *Adv. High Energy Phys.* **2016**, 1615081 (2016). doi:10.1155/2016/1615081

60. R. D. Ball, V. Bertone, S. Carrazza, L. D. Debbio, S. Forte, P. Groth-Merrild, A. Guffanti, N. P. Hartland, Z. Kassabov, J. I. Latorre, E. R. Nocera, J. Rojo, L. Rottoli, E. Slade, M. Ubiali, Parton distributions from high-precision collider data: NNPDF Collaboration. *Eur. Phys. J. C* **77**, 663 (2017). doi:10.1140/epjc/s10052-017-5199-5 Medline

61. T. J. Hou, J. Gao, T. J. Hobbs, K. Xie, S. Dulat, M. Guzzi, J. Huston, P. Nadolsky, J. Pumplin, C. Schmidt, I. Sitiwaldi, D. Stump, C.-P. Yuan, New CTEQ global analysis of quantum chromodynamics with high-precision data from the LHC. *Phys. Rev. D* **103**, 014013 (2021). doi:10.1103/PhysRevD.103.014013

62. L. A. Harland-Lang, A. D. Martin, P. Motylinski, R. S. Thorne, Parton distributions in the LHC era: MMHT 2014 PDFs. *Eur. Phys. J. C* **75**, 204 (2015). doi:10.1140/epjc/s10052-015-3397-6 Medline

63. Supplementary materials.

64. A. V. Kotwal, C. Hays, Electromagnetic shower properties in a lead-scintillator sampling calorimeter. *Nucl. Instrum. Methods Phys. Res. A* **729**, 25–35 (2013). doi:10.1016/j.nima.2013.05.185

65. A. V. Kotwal, C. Hays, Drift chamber alignment using cosmic rays. *Nucl. Instrum. Methods Phys. Res. A* **762**, 85–99 (2014). doi:10.1016/j.nima.2014.05.050

66. L. Lyons, D. Gibaut, P. Clifford, How to combine correlated estimates of a single physical quantity. *Nucl. Instrum. Methods Phys. Res. A* **270**, 110–117 (1988). doi:10.1016/0168-9002(88)90018-6

67. T. Aaltonen *et al*. (CDF Collaboration), High precision measurement of the W-boson mass with the CDF II detector, Zenodo (2022); https://doi.org/10.5281/zenodo.6245867.

68. G. Arnison, A. Astbury, B. Aubert, C. Bacci, G. Bauer, A. Bézaguet, R. Böck, T. J. V. Bowcock, M. Calvetti, T. Carroll, P. Catz, P. Cennini, S. Centro, F. Ceradini, S. Cittolin, D. Cline, C. Cochet, J. Colas, M. Corden, D. Dallman, M. DeBeer, M. Della Negra, M. Demoulin, D. Denegri, A. Di Ciaccio, D. DiBitonto, L. Dobrzynski, J. D. Dowell, M. Edwards, K. Eggert, E. Eisenhandler, N. Ellis, P. Erhard, H. Faissner, G. Fontaine, R. Frey, R. Frühwirth, J. Garvey, S. Geer, C. Ghesquière, P. Ghez, K. L. Giboni, W. R. Gibson, Y. Giraud-Héraud, A. Givernaud, A. Gonidec, G. Grayer, P. Gutierrez, T. Hansl-Kozanecka, W. J. Haynes, L. O. Hertzberger, C. Hodges, D. Hoffmann, H. Hoffmann, D. J. Holthuizen, R. J. Homer, A. Honma, W. Jank, G. Jorat, P. I. P. Kalmus, V. Karimäki, R. Keeler, I. Kenyon, A. Kernan, R. Kinnunen, H. Kowalski, W. Kozanecki, D. Kryn, F. Lacava, J.-P. Laugier, J.-P. Lees, H. Lehmann, K. Leuchs, A. Lévêque, E. Linglin, E. Locci, M. Loret, J.-J. Malosse, T. Markiewicz, G. Maurin, T. McMahon, J.-P.

Mendiburu, M.-N. Minard, M. Moricca, H. Muirhead, F. Muller, A. K. Nandi, L. Naumann, A. Norton, A. Orkin-Lecourtois, L. Paoluzi, G. Petrucci, G. P. Mortari, M. Pimiä, A. Placci, E. Radermacher, J. Ransdell, H. Reithler, J.-P. Revol, J. Rich, M. Rijssenbeek, C. Roberts, J. Rohlf, P. Rossi, C. Rubbia, B. Sadoulet, G. Sajot, G. Salvi, J. Salvini, J. Sass, A. Saudraix, A. Savoy-Navarro, D. Schinzel, W. Scott, T. P. Shah, M. Spiro, J. Strauss, K. Sumorok, F. Szoncso, D. Smith, C. Tao, G. Thompson, J. Timmer, E. Tscheslog, J. Tuominiemi, S. Van der Meer, J.-P. Vialle, J. Vrana, V. Vuillemin, H. D. Wahl, P. Watkins, J. Wilson, Y. G. Xie, M. Yvert, E. Zurfluh; UA1 Collaboration, Experimental observation of isolated large transverse energy electrons with associated missing energy at s = 540 GeV. *Phys. Lett. B* **122**, 103–116 (1983). doi:10.1016/0370-2693(83)91177-2

69. M. Banner, R. Battiston, P. Bloch, F. Bonaudi, K. Borer, M. Borghini, J.-C. Chollet, A. G. Clark, C. Conta, P. Darriulat, L. Di Lella, J. Dines-Hansen, P.-A. Dorsaz, L. Fayard, M. Fraternali, D. Froidevaux, J.-M. Gaillard, O. Gildemeister, V. G. Goggi, H. Grote, B. Hahn, H. Hänni, J. R. Hansen, P. Hansen, T. Himel, V. Hungerbühler, P. Jenni, O. Kofoed-Hansen, E. Lançon, M. Livan, S. Loucatos, B. Madsen, P. Mani, B. Mansoulie, G. C. Mantovani, L. Mapelli, B. Merkel, M. Mermikides, R. Møllerud, B. Nilsson, C. Onions, G. Parrour, F. Pastore, H. Plothow-Besch, M. Polverel, J.-P. Repellin, A. Rothenberg, A. Roussarie, G. Sauvage, J. Schacher, J. L. Siegrist, H. M. Steiner, G. Stimpfl, F. Stocker, J. Teiger, V. Vercesi, A. Weidberg, H. Zaccone, W. Zeller; UA2 Collaboration, Observation of single isolated electrons of high transverse momentum in events with missing transverse energy at the CERN p collider. *Phys. Lett. B* **122**, 476–485 (1983). doi:10.1016/0370-2693(83)91605-2

70. G. Arnison, A. Astbury, B. Aubert, C. Bacci, G. Bauer, A. Bézaguet, R. Böck, T. J. V. Bowcock, M. Calvetti, P. Catz, P. Cennini, S. Centro, F. Ceradini, S. Cittolin, D. Cline, C. Cochet, J. Colas, M. Corden, D. Dallman, D. Dau, M. DeBeer, M. D. Negra, M. Demoulin, D. Denegri, A. Di Ciaccio, D. Dibitonto, L. Dobrzynski, J. D. Dowell, K. Eggert, E. Eisenhandler, N. Ellis, P. Erhard, H. Faissner, M. Fincke, G. Fontaine, R. Frey, R. Frühwirth, J. Garvey, S. Geer, C. Ghesquière, P. Ghez, K. Giboni, W. R. Gibson, Y. Giraud-Héraud, A. Givernaud, A. Gonidec, G. Grayer, T. Hansl-Kozaàecka, W. J. Haynes, L. O. Hertzberger, C. Hodges, D. Hoffmann, H. Hoffmann, D. J. Holthuizen, R. J. Homer, A. Honma, W. Jank, G. Jorat, P. I. P. Kalmus, V. Karimäki, R. Keeler, I. Kenyon, A. Kernan, R. Kinnunen, W. Kozanecki, D. Kryn, F. Lacava, J.-P. Laugier, J.-P. Lees, H. Lehmann, R. Leuchs, A. Lévêque, D. Linglin, E. Locci, J.-J. Malosse, T. Markiewicz, G. Maurin, T. McMahon, J.-P. Mendiburu, M.-N. Minard, M. Mohammadi, M. Moricca, K. Morgan, H. Muirhead, F. Muller, A. K. Nandi, L. Naumann, A. Norton, A. Orkin-Lecourtois, L. Paoluzi, F. Pauss, G. P. Mortari, E. Pietarinen, M. Pimiä, A. Placci, J. P. Porte, E. Radermacher, J. Ransdell, H. Reithler, J.-P. Revol, J. Rich, M. Rijssenbeek, C. Roberts, J. Rohlf, P. Rossi, C. Rubbia, B. Sadoulet, G. Sajot, G. Salvi, G. Salvini, J. Sass, J. Saudraix, A. Savoy-Navarro, D. Schinzel, W. Scott, T. P. Shah, M. Spiro, J. Strauss, J. Streets, K. Sumorok, F. Szoncso, D. Smith, C. Tao, G. Thompson, J. Timmer, E. Tscheslog, J. Touminiemi, B. Van Eijk, J.-P. Vialle, J. Vrana, V. Vuillemin, H. D. Wahl, P. Watkins, J. Wilson, C. Wulz, G. Y. Xie, M. Yvert, E. Zurfluh; UA1 Collaboration, Experimental observation of lepton pairs of invariant mass around 95 GeV/c^2 at the CERN SPS collider. *Phys. Lett. B* **126**, 398–410 (1983). doi:10.1016/0370-2693(83)90188-0

71. P. Bagnaia, M. Banner, R. Battiston, P. Bloch, F. Bonaudi, K. Borer, M. Borghini, J.-C. Chollet, A. G. Clark, C. Conta, P. Darriulat, L. Di Lella, J. Dines-Hansen, P. A. Dorsaz, L. Fayard, M. Fraternali, D. Froidevaux, G. Fumagalli, J.-M. Gaillard, O. Gildemeister, V. G. Goggi, H. Grote, B. Hahn, H. Hänni, J. R. Hansen, P. Hansen, T. Himel, V. Hungerbühler, P. Jenni, O. Kofoed-Hansen, E. Lançon, M. Livan, S. Loucatos, B. Madsen, P. Mani, B. Mansoulié, G. C. Mantovani, L. Mapelli, B. Merkel, M. Mermikides, R. Møllerud, B. Nilsson, C. Onions, G. Parrour, F. Pastore, H. Plothow-Besch, M. Polverel, J.-P. Repellin, A. Rimoldi, A. Rothenberg, A. Roussarie, G. Sauvage, J. Schacher, J. L. Siegrist, H. M. Steiner, G. Stimpfl, F. Stocker, J. Teiger, V. Vercesi, A. R. Weidberg, H. Zaccone, J. A. Zakrzewski, W. Zeller; UA2 Collaboration, Evidence for $Z^0 \rightarrow e^+e^-$ at the CERN p collider. *Phys. Lett. B* **129**, 130–140 (1983). doi:10.1016/0370-2693(83)90744-X

72. A. D. Martin, W. J. Stirling, R. S. Thorne, G. Watt, Parton distributions for the LHC. *Eur. Phys. J. C* **63**, 189–285 (2009). doi:10.1140/epjc/s10052-009-1072-5

73. D. Acosta *et al.*; CDF Collaboration, Measurement of the J/ψ meson and *b*-hadron prduction cross sections in $p\overline{p}$ collisions at $\sqrt{s} = 1960$ GeV. *Phys. Rev. D* **71**, 032001 (2005). doi:10.1103/PhysRevD.71.032001

74. A. Sill *et al.*, CDF Run II silicon tracking projects. *Nucl. Instrum. Methods Phys. Res. A* **447**, 1–8 (2000). doi:10.1016/S0168-9002(00)00166-2

75. H. Minemura, S. Mori, M. Noguchi, R. Yoshizaki, K. Kondo, R. Fast, R. Kephart, R. Wands, R. Yamada, K. Aihara, K. Asano, I. Kamishita, I. Kurita, H. Ogata, R. Saito, T. Suzuki, T. Yamagiwa, Construction and testing of a 3 m diameter × 5 m superconducting solenoid for the Fermilab collider detector facility (CDF). *Nucl. Instrum. Methods Phys. Res. A* **238**, 18–34 (1985). doi:10.1016/0168-9002(85)91023-X

76. L. Balka, K. Coover, R. Diebold, W. Evans, N. Hill, L. Nodulman, J. Proudfoot, R. Rezmer, J. R. Sauer, P. Schoessow, D. Underwood, R. G. Wagner, E. Walschon, A. B. Wicklund, T. Kamon, Y. Kikuchi, K. Kondo, K. Takikawa, A. Yamashita, J. E. Elias, H. Jensen, H. Kautzky, R. Krull, K. Yasuoka, T. Devlin, U. Joshi, D. Bauer, D. Connor, J. W. Cooper, S. R. Hahn, M. Miller, R. VanBerg, H. H. Williams, S. Kobayashi, A. Murakami, S. Mikamo, The CDF central electromagnetic calorimeter. *Nucl. Instrum. Methods Phys. Res. A* **267**, 272–279 (1988). doi:10.1016/0168-9002(88)90474-3

77. K. Yasuoka, S. Mikamo, T. Kamon, A. Yamashita, Response maps of the CDF central electromagnetic calorimeter with electrons. *Nucl. Instrum. Methods Phys. Res. A* **267**, 315–329 (1988). doi:10.1016/0168-9002(88)90477-9

78. S. Bertolucci, M. Cordelli, B. Esposito, M. Curatolo, P. Giromini, S. Miscetti, A. Sansoni, G. Apollinari, F. Bedeschi, S. Belforte, G. Bellettini, N. Bonavita, F. Cervelli, G. Chiarelli, R. Del Fabbro, M. Dell'Orso, E. Focardi, P. Giannetti, A. Menzione, R. Paoletti, G. Punzi, L. Ristori, A. Scribano, P. Sestini, A. Stefanini, G. Tonelli, F. Zetti, V. E. Barnes, A. Di Virgilio, A. F. Garfinkel, S. E. Kuhlmann, A. T. Laasanen, H. Jensen, H. Kautzky, The CDF central and endwall hadron calorimeter. *Nucl. Instrum. Methods Phys. Res. A* **267**, 301–314 (1988). doi:10.1016/0168-9002(88)90476-7

79. G. Apollinari, K. Goulianos, P. Melese, M. Lindgren, Shower maximum detector for the CDF plug upgrade calorimeter. *Nucl. Instrum. Methods Phys. Res. A* **412**, 515–526 (1998). doi:10.1016/S0168-9002(98)00286-1

80. M. Albrow, S. Aota, G. Apollinari, T. Asakawa, M. Bailey, P. de Barbaro, V. Barnes, K. Biery, A. Bodek, L. Breccia, R. Brunetti, H. Budd, D. Cauz, L. Demortier, I. Fiori, M. Frautschi, Y. Fukui, O. Ganel, Y. Gotra, S. Hahn, T. Handa, K. Hatakeyama, H. Ikeda, G. Introzzi, J. Iwai, T. Kikuchi, S. H. Kim, W. Kowald, A. Laasanen, J. Lamoureux, M. Lindgren, J. Liu, S. Lusin, P. Melese, H. Minato, S. Murgia, H. Nakada, J. Patrick, G. Pauletta, W. Sakumoto, L. Santi, Y. Seiya, A. Solodsky, R. Wigmans, S. Zucchelli, The CDF plug upgrade electromagnetic calorimeter: Test beam results. *Nucl. Instrum. Methods Phys. Res. A* **480**, 524–546 (2002). doi:10.1016/S0168-9002(01)01238-4

81. Y.-S. Tsai, Pair production and bremsstrahlung of charged leptons. *Rev. Mod. Phys.* **46**, 815–851 (1974). doi:10.1103/RevModPhys.46.815

82. L. D. Landau, I. J. Pomeranchuk, Limits of Applicability of the Theory of Bremsstrahlung Electrons and Pair Production for High Energies. [in Russian] *Dokl. Akad. Nauk SSSR* **92**, 535 (1953).

83. L. D. Landau, I. J. Pomeranchuk, Electron-cascade processes at very high energies. [in Russian] *Dokl. Akad. Nauk SSSR* **92**, 735 (1953).

84. A. B. Migdal, Bremsstrahlung and Pair Production in Condensed Media at High Energies. *Phys. Rev.* **103**, 1811–1820 (1956). doi:10.1103/PhysRev.103.1811

85. A. B. Migdal, *Zh. Eksp. Tear. Fiz.* **32**, 633 (1957) [in Russian; Engl. transl.: Bremsstrahlung and pair production at high energies in condensed media. *Sov. Phys. JETP* **5**, 527 (1957)].

86. E. Gerchtein, M. Paulini, CDF detector simulation framework and performance. arXiv:physics/0306031 [physics.comp-ph] (2003).

87. R. Brun, F. Bruyant, F. Carminati, S. Giani, M. Maire, A. McPherson, G. Patrick, L. Urban, "GEANT: Detector description and simulation tool," CERN Program Library Long Writeup W5013, version 3.15 (1993); https://cds.cern.ch/record/1082634.

88. S. Agostinelli, J. Allison, K. Amako, J. Apostolakis, H. Araujo, P. Arce, M. Asai, D. Axen, S. Banerjee, G. Barrand, F. Behner, L. Bellagamba, J. Boudreau, L. Broglia, A. Brunengo, H. Burkhardt, S. Chauvie, J. Chuma, R. Chytracek, G. Cooperman, G. Cosmo, P. Degtyarenko, A. Dell'Acqua, G. Depaola, D. Dietrich, R. Enami, A. Feliciello, C. Ferguson, H. Fesefeldt, G. Folger, F. Foppiano, A. Forti, S. Garelli, S. Giani, R. Giannitrapani, D. Gibin, J. J. Gómez Cadenas, I. González, G. Gracia Abril, G. Greeniaus, W. Greiner, V. Grichine, A. Grossheim, S. Guatelli, P. Gumplinger, R. Hamatsu, K. Hashimoto, H. Hasui, A. Heikkinen, A. Howard, V. Ivanchenko, A. Johnson, F. W. Jones, J. Kallenbach, N. Kanaya, M. Kawabata, Y. Kawabata, M. Kawaguti, S. Kelner, P. Kent, A. Kimura, T. Kodama, R. Kokoulin, M. Kossov, H. Kurashige, E. Lamanna, T. Lampén, V. Lara, V. Lefebure, F. Lei, M. Liendl, W. Lockman, F. Longo, S. Magni, M. Maire, E. Medernach, K. Minamimoto, P. Mora de Freitas, Y. Morita, K. Murakami, M. Nagamatu, R. Nartallo, P. Nieminen, T. Nishimura, K. Ohtsubo, M. Okamura, S. O'Neale, Y. Oohata, K. Paech, J. Perl, A. Pfeiffer, M. G. Pia, F. Ranjard, A. Rybin, S. Sadilov, E. Di Salvo, G. Santin, T. Sasaki, N. Savvas, Y. Sawada, S. Scherer, S. Sei, V. Sirotenko, D. Smith, N. Starkov, H. Stoecker, J. Sulkimo,

M. Takahata, S. Tanaka, E. Tcherniaev, E. Safai Tehrani, M. Tropeano, P. Truscott, H. Uno, L. Urban, P. Urban, M. Verderi, A. Walkden, W. Wander, H. Weber, J. P. Wellisch, T. Wenaus, D. C. Williams, D. Wright, T. Yamada, H. Yoshida, D. Zschiesche, GEANT4—A simulation toolkit. *Nucl. Instrum. Methods Phys. Res. A* **506**, 250–303 (2003). doi:10.1016/S0168-9002(03)01368-8

89. D. Stump, J. Huston, J. Pumplin, W.-K. Tung, H.-L. Lai, S. Kuhlmann, J. F. Owens, Inclusive jet production, parton distributions, and the search for new physics. *J. High Energy Phys.* **2003**, 046 (2003). doi:10.1088/1126-6708/2003/10/046

90. S. Alekhin, J. Blümlein, S. Moch, R. Plačakyte, Parton distribution functions, α_s, and heavy-quark masses for LHC Run II. *Phys. Rev. D* **96**, 014011 (2017). doi:10.1103/PhysRevD.96.014011

91. A. Accardi, L. T. Brady, W. Melnitchouk, J. F. Owens, N. Sato, Constraints on large-*x* parton distributions from new weak boson production and deep-inelastic scattering data. *Phys. Rev. D* **93**, 114017 (2016). doi:10.1103/PhysRevD.93.114017

92. A. V. Kotwal, Novel methods of constraining the parton distribution function uncertainty in the measurement of the *W*-boson mass. *Phys. Rev. D* **98**, 033008 (2018). doi:10.1103/PhysRevD.98.033008

93. S. Carrazza, S. Forte, Z. Kassabov, J. I. Latorre, J. Rojo, An unbiased Hessian representation for Monte Carlo PDFs. *Eur. Phys. J. C* **75**, 369 (2015). doi:10.1140/epjc/s10052-015-3590-7 Medline

94. S. Carrazza, S. Forte, Z. Kassabov, J. Rojo, Specialized minimal PDFs for optimized LHC calculations. *Eur. Phys. J. C* **76**, 205 (2016). doi:10.1140/epjc/s10052-016-4042-8 Medline

95. N. Baillie, S. Tkachenko, J. Zhang, P. Bosted, S. Bültmann, M. E. Christy, H. Fenker, K. A. Griffioen, C. E. Keppel, S. E. Kuhn, W. Melnitchouk, V. Tvaskis, K. P. Adhikari, D. Adikaram, M. Aghasyan, M. J. Amaryan, M. Anghinolfi, J. Arrington, H. Avakian, H. Baghdasaryan, M. Battaglieri, A. S. Biselli, D. Branford, W. J. Briscoe, W. K. Brooks, V. D. Burkert, D. S. Carman, A. Celentano, S. Chandavar, G. Charles, P. L. Cole, M. Contalbrigo, V. Crede, A. D'Angelo, A. Daniel, N. Dashyan, R. De Vita, E. De Sanctis, A. Deur, B. Dey, C. Djalali, G. Dodge, J. Domingo, D. Doughty, R. Dupre, D. Dutta, R. Ent, H. Egiyan, A. El Alaoui, L. El Fassi, L. Elouadrhiri, P. Eugenio, G. Fedotov, S. Fegan, A. Fradi, M. Y. Gabrielyan, N. Gevorgyan, G. P. Gilfoyle, K. L. Giovanetti, F. X. Girod, W. Gohn, E. Golovatch, R. W. Gothe, L. Graham, B. Guegan, M. Guidal, N. Guler, L. Guo, K. Hafidi, D. Heddle, K. Hicks, M. Holtrop, E. Hungerford, C. E. Hyde, Y. Ilieva, D. G. Ireland, M. Ispiryan, E. L. Isupov, S. S. Jawalkar, H. S. Jo, N. Kalantarians, M. Khandaker, P. Khetarpal, A. Kim, W. Kim, P. M. King, A. Klein, F. J. Klein, A. Klimenko, V. Kubarovsky, S. V. Kuleshov, N. D. Kvaltine, K. Livingston, H. Y. Lu, I. J. D. MacGregor, Y. Mao, N. Markov, B. McKinnon, T. Mineeva, B. Morrison, H. Moutarde, E. Munevar, P. Nadel-Turonski, A. Ni, S. Niccolai, I. Niculescu, G. Niculescu, M. Osipenko, A. I. Ostrovidov, L. Pappalardo, K. Park, S. Park, E. Pasyuk, S. Anefalos Pereira, S. Pisano, S. Pozdniakov, J. W. Price, S. Procureur, Y. Prok, D. Protopopescu, B. A. Raue, G. Ricco, D. Rimal, M. Ripani, G. Rosner, P. Rossi, F. Sabatié, M. S. Saini, C. Salgado, D. Schott, R. A. Schumacher, E. Seder, Y. G.

Sharabian, D. I. Sober, D. Sokhan, S. Stepanyan, S. S. Stepanyan, P. Stoler, S. Strauch, M. Taiuti, W. Tang, M. Ungaro, M. F. Vineyard, E. Voutier, D. P. Watts, L. B. Weinstein, D. P. Weygand, M. H. Wood, L. Zana, B. Zhao; CLAS Collaboration, Measurement of the neutron F_2 structure function via spectator tagging with CLAS. *Phys. Rev. Lett.* **108**, 142001 (2012). doi:10.1103/PhysRevLett.108.142001 Medline

96. S. Tkachenko, N. Baillie, S. E. Kuhn, J. Zhang, J. Arrington, P. Bosted, S. Bültmann, M. E. Christy, D. Dutta, R. Ent, H. Fenker, K. A. Griffioen, M. Ispiryan, N. Kalantarians, C. E. Keppel, W. Melnitchouk, V. Tvaskis, K. P. Adhikari, M. Aghasyan, M. J. Amaryan, S. Anefalos Pereira, H. Avakian, J. Ball, N. A. Baltzell, M. Battaglieri, I. Bedlinskiy, A. S. Biselli, W. J. Briscoe, W. K. Brooks, V. D. Burkert, D. S. Carman, A. Celentano, S. Chandavar, G. Charles, P. L. Cole, M. Contalbrigo, O. Cortes, V. Crede, A. D'Angelo, N. Dashyan, R. De Vita, E. De Sanctis, A. Deur, C. Djalali, G. E. Dodge, D. Doughty, R. Dupre, H. Egiyan, A. El Alaoui, L. El Fassi, L. Elouadrhiri, P. Eugenio, G. Fedotov, J. A. Fleming, B. Garillon, N. Gevorgyan, Y. Ghandilyan, G. P. Gilfoyle, K. L. Giovanetti, F. X. Girod, J. T. Goetz, E. Golovatch, R. W. Gothe, M. Guidal, L. Guo, K. Hafidi, H. Hakobyan, C. Hanretty, N. Harrison, M. Hattawy, K. Hicks, D. Ho, M. Holtrop, C. E. Hyde, Y. Ilieva, D. G. Ireland, B. S. Ishkhanov, H. S. Jo, D. Keller, M. Khandaker, A. Kim, W. Kim, P. M. King, A. Klein, F. J. Klein, S. Koirala, V. Kubarovsky, S. V. Kuleshov, P. Lenisa, S. Lewis, K. Livingston, H. Lu, M. MacCormick, I. J. D. MacGregor, N. Markov, M. Mayer, B. McKinnon, T. Mineeva, M. Mirazita, V. Mokeev, R. A. Montgomery, H. Moutarde, C. Munoz Camacho, P. Nadel-Turonski, S. Niccolai, G. Niculescu, I. Niculescu, M. Osipenko, L. L. Pappalardo, R. Paremuzyan, K. Park, E. Pasyuk, J. J. Phillips, S. Pisano, O. Pogorelko, S. Pozdniakov, J. W. Price, S. Procureur, D. Protopopescu, A. J. R. Puckett, D. Rimal, M. Ripani, A. Rizzo, G. Rosner, P. Rossi, P. Roy, F. Sabatié, D. Schott, R. A. Schumacher, E. Seder, I. Senderovich, Y. G. Sharabian, A. Simonyan, G. D. Smith, D. I. Sober, D. Sokhan, S. Stepanyan, S. S. Stepanyan, S. Strauch, W. Tang, M. Ungaro, A. V. Vlassov, H. Voskanyan, E. Voutier, N. K. Walford, D. Watts, X. Wei, L. B. Weinstein, M. H. Wood, L. Zana, I. Zonta, Measurement of the structure function of the nearly free neutron using spectator tagging in inelastic ^{2}H(e,$e'p_s$)X scattering with CLAS. *Phys. Rev. C* **89**, 045206 (2014). doi:10.1103/PhysRevC.89.045206

97. G. Bozzi, S. Catani, G. Ferrera, D. de Florian, M. Grazzini, Transverse-momentum resummation: A perturbative study of Z production at the Tevatron. *Nucl. Phys. B* **815**, 174–197 (2009). doi:10.1016/j.nuclphysb.2009.02.014

98. G. Bozzi, S. Catani, G. Ferrera, D. de Florian, M. Grazzini, Production of Drell–Yan lepton pairs in hadron collisions: Transverse-momentum resummation at next-to-next-to-leading logarithmic accuracy. *Phys. Lett. B* **696**, 207–213 (2011). doi:10.1016/j.physletb.2010.12.024

99. Instructions to run the DYQT program are given in http://pcteserver.mi.infn.it/~ferrera/codes/note-dyqt.pdf.

100. M. Chen, P. Zerwas, Equivalent-particle approximations in electron and photon processes of higher-order QED. *Phys. Rev. D* **12**, 187–197 (1975). doi:10.1103/PhysRevD.12.187

101. T. Sjöstrand, High-energy-physics event generation with PYTHIA 5.7 and JETSET 7.4. *Comput. Phys. Commun.* **82**, 74–89 (1994). doi:10.1016/0010-4655(94)90132-5

102. We use PYTHIA version 6.129 for W and Z production, version 6.136 for Υ production, and version 6.157 for J/ψ production.

103. A. Banfi, S. Redford, M. Vesterinen, P. Waller, T. R. Wyatt, Optimisation of variables for studying dilepton transverse momentum distributions at hadron colliders. *Eur. Phys. J. C* **71**, 1600 (2011). doi:10.1140/epjc/s10052-011-1600-y

104. D. Beecher, thesis, University College London (2011); FERMILAB-THESIS-2011-18.

105. E. A. Kuraev, V. S. Fadin, On radiative corrections to $e^+ e^-$ single photon annihilation at high-energy. [in Russian] *Yad. Fiz.* **41**, 733 (1985).

106. V. V. Sudakov, Vertex parts at very high energies in quantum electrodynamics. *Sov. Phys. JETP* **3**, 65 (1956).

107. Y. Zeng, thesis, Duke University (2012); FERMILAB-THESIS-2012-27.

108. J. Alitti, G. Ambrosini, R. Ansari, D. Autiero, P. Bareyre, I. A. Bertram, G. Blaylock, P. Bonamy, K. Borer, M. Bourliaud, D. Buskulic, G. Carboni, D. Cavalli, V. Cavasinni, P. Cenci, J. C. Chollet, C. Conta, G. Costa, F. Costantini, L. Cozzi, A. Cravero, M. Curatolo, A. Dell'Acqua, T. DelPrete, R. S. DeWolf, L. DiLella, Y. Ducros, G. F. Egan, K. F. Einsweiler, B. Esposito, L. Fayard, A. Federspiel, R. Ferrari, M. Fraternali, D. Froidevaux, G. Fumagalli, F. Gianotti, O. Gildermeister, C. Gössling, V. G. Goggi, S. Grünendahl, K. Hara, S. Hellman, J. Hřivnáč, H. Hufnagel, E. Hugentobler, K. Hultqvist, E. Iacopini, J. Incandela, K. Jakobs, P. Jenni, E. E. Kluge, N. Kurz, S. Lami, P. Lariccia, M. Lefebvre, L. Linssen, M. Livan, P. Lubrano, C. Magneville, L. Mandelli, L. Mapelli, M. Mazzanti, K. Meier, B. Merkel, J. P. Meyer, M. Moniez, R. Moning, M. Morganti, L. Müller, D. J. Munday, M. Nessi, F. Nessi-Tedaldi, C. Onions, T. Pal, M. A. Parker, G. Parrour, F. Pastore, E. Pennacchio, J. M. Pentney, M. Pepe, L. Perini, C. Petridou, P. Petroff, H. Plothow-Besch, G. Polesello, A. Poppleton, K. Pretzl, M. Primavera, M. Punturo, J. P. Repellin, A. Rimoldi, M. Sacchi, P. Scampoli, J. Schacher, B. Schmidt, V. Šimák, S. L. Singh, V. Sondermann, R. Spiwoks, S. Stapnes, C. Talamonti, F. Tondini, S. N. Tovey, E. Tsesmelis, G. Unal, M. Valdata-Nappi, V. Vercesi, V. Vercesi, A. R. Weidberg, P. S. Wells, T. O. White, D. R. Wood, S. A. Wotton, H. Zaccone, A. Zylberstejn; UA2 Collaboration, An improved determination of the ratio of W and Z masses at the CERN pp collider. *Phys. Lett. B* **276**, 354–364 (1992). doi:10.1016/0370-2693(92)90332-X

109. S. Malik, thesis, University College London (2009); FERMILAB-THESIS-2009-59.

110. C. Peterson, T. Rögnvaldsson, L. Lönnblad, JETNET 3.0—A versatile artificial neural network package. *Comput. Phys. Commun.* **81**, 185–220 (1994). doi:10.1016/0010-4655(94)90120-1